Comprehensive computational analysis of the impact of regular head waves on ship bare hull performance

Ocean Engineering 288 (2023) 116049

Contents lists available at ScienceDirect

Ocean Engineering

journal homepage: www.elsevier.com/locate/oceaneng

Comprehensive computational analysis of the impact of regular head waves on ship bare hull performance

Mohsen Irannezhad [a,*], Rickard E. Bensow [a], Martin Kjellberg [b], Arash Eslamdoost [a]

[a] Department of Mechanics and Maritime Sciences, Chalmers University of Technology, 412 96, Gothenburg, Sweden
[b] RISE - SSPA Maritime Center, 412 58, Gothenburg, Sweden

ARTICLE INFO

Keywords:
Ship motions
Resistance
Nominal wake
Regular head waves
CFD
Grid convergence study

ABSTRACT

This paper focuses on investigating the impact of waves on ship hydrodynamic performance, enhancing our understanding of seakeeping characteristics and contributing to advanced ship and propeller design. It examines the resistance, motions, and nominal wake of the KVLCC2 bare hull, which is free to surge, heave, and pitch, in both calm water and regular head waves using a RANS approach. The research reveals a substantial dependency of the wake on grid resolution, particularly in calm water and shorter waves, while motions and resistance display a weaker dependency. The computed nominal wake is compared against towing tank SPIV measurements. Utilizing Fourier analyses and reconstructed time series, the study examines correlations among various factors influencing the bare hull's performance in waves. The axial velocity component of the wake in waves demonstrates significant time variations, mainly driven by higher harmonic amplitudes. This dynamic wake is influenced by instantaneous propeller disk velocities due to hull motions, orbital wave velocities, boundary layer contraction/expansion, bilge vortex and shaft vortex dynamics. The wake distribution at the propeller plane not only differs significantly from the calm water wake in longer waves but also exhibits notably larger time-averaged values (up to 21%).

1. Introduction

Traditionally, ship performance in calm water has been the main research topic in ship hydrodynamics. However, calm water is rather an exception during an actual voyage. Ships may experience involuntary/voluntary speed loss when they operate in a more realistic environmental condition than calm water. Various factors responsible for the loss of speed in a seaway are mentioned by Bhattacharyya (1978) as added resistance due to waves, wind and ship motions, loss of propulsive efficiency (related to propeller underload/overload, altered conditions affecting the characteristics of the propulsive machinery and variation of wake into the propeller due to motions, speed loss as well as propeller ventilation/emergence) and voluntary reduction of engine speed for preventing green water, slamming, excessive accelerations, propeller racing or course keeping. Therefore, ship designers consider an additional experience-based reserved power of 15%–25%, called "sea margin" (ITTC, 2017a), to ensure reliable performance of ships in other environmental conditions than calm water. Although this approach has been proven to be suitable for power predictions over the years for a very large number of vessels, it introduces a drawback that the ships may rarely encounter such conditions which may lead to underpower/overpower situations. Currently, there is a growing inclination towards ship design optimization in operational conditions closer to near-service conditions than calm water.

Waves are playing a significant role in affecting most of the aforementioned factors responsible for ship speed loss. Operating in waves may have several effects on ship behavior. The interactions between waves, hull and the propulsion system of a ship may significantly affect the ship motions, resistance, wake and propeller/engine load in comparison to calm water operational conditions. Added resistance due to waves and the variation of propulsive factors for a ship operating in real sea conditions affect its required engine power in comparison to the idealistic calm water conditions, which may lead to a noticeable ship performance degradation. Moreover, large amplitude ship motions in a rough sea may adversely affect the ship structural integrity and harm the crew and cargo. Therefore, ship performance prediction in waves is crucial, especially in the early stages of the ship design process.

A seaway may contain waves with various heights and lengths propagating in different directions, hence for a full analysis of ship performance in waves, a broad range of environmental and operational conditions have to be considered. Moreover, the ship hydrodynamic responses may be subject to various correlated factors originating from the interaction effects between different ship components (e.g., hull,

* Corresponding author.
E-mail address: mohsen.irannezhad@chalmers.se (M. Irannezhad).

https://doi.org/10.1016/j.oceaneng.2023.116049
Received 31 July 2023; Received in revised form 20 September 2023; Accepted 10 October 2023
Available online 31 October 2023

Nomenclature

α	Multiplication constant in uncertainty analysis tool
$\bar{\psi}$	Mean (time-averaged) of quantity under study in Fourier analysis
$\ddot{\Delta}z_{shaft}$	Vertical acceleration of the shaft center (m/s^2)
$\ddot{x}$	Surge acceleration (m/s^2)
Δt	Time step (s)
Δz_{shaft}	Vertical displacement of shaft from its initial position (m)
Δ	Mass displacement (kg)
δ_n	First layer cell thickness of prism layers in grid n (m)
$\dot{\Delta}z_{shaft}$	Vertical velocity of the shaft center (m/s)
$\dot{\theta}$	Pitch velocity (deg/s)
$\dot{x}$	Surge velocity (m/s)
$\dot{z}$	Heave velocity (m/s)
γ_n	Growth ratio between layers of prism layers in grid n (–)
λ	Wave length (m)
μ	Heading angle (deg)
∇	Volume displacement (m^3)
ν	Kinematic viscosity of water (m^2/s)
ω	Fast Fourier Transform frequency (rad/s)
ω_E	Encounter wave frequency (rad/s)
ω_w	Wave frequency (rad/s)
Φ_0	Estimated exact solution in uncertainty analysis tool
Φ_i	Solution of the ith grid in uncertainty analysis tool
$\psi(t)$	Time series of the quantity under study in Fourier analysis
ψ_i	The ith harmonic amplitude of quantity under study in Fourier analysis
$\psi_{\epsilon i}$	The ith harmonic phase of quantity under study in Fourier analysis
ρ	Water density (kg/m^3)
θ	Pitch motion (deg)
θ_i	The ith harmonic amplitude of pitch motion at wave encounter frequency (deg)
ζ	Free surface elevation (m)
A	Wave amplitude $H/2$ (m)
B	Breadth at mid-ship (m)
C_B	Block coefficient (–)
C_T	Non-dimensional total resistance (–)
D_{hub}	Hub diameter (m)
D_{prop}	Propeller diameter (m)
F_0	External constant force (N)
Fr	Froude number (–)
g	Gravitational acceleration (m/s^2)
H	Wave height (m)
h_i	Typical cell size of the ith grid in uncertainty analysis tool
K	Spring stiffness (N/m)
k	Wave number $360/\lambda$ (deg/m)
K_{yy}	Mass radius of gyration around Y-axis (m)
L	Length between perpendiculars (m)
L_{CG}	Longitudinal position of center of gravity from aft perpendicular (m)
m_1	Mass of hull and pitch-free gimbal (kg)
m_2	Mass of dynamometer (kg)
m_3	Mass of light weight carriage (kg)
n	Grid refinement level (–)
N_n	Total number of layers of prism layers in grid n (–)
p	Observed order of grid convergence in uncertainty analysis tool
R	Propeller radius (m)
r	Radial position on propeller disk (m)
R_P	Pressure resistance component (N)
R_S	Shear resistance component (N)
R_T	Total resistance (N)
R_{hub}	Hub radius (m)
r_i	Assumed center of the ith circumferential surface area on propeller disk (m)
Re	Reynolds number (–)
S	Bare hull wetted surface area at rest (m^2)
t	Time (s)
T_A	Draft at aft perpendicular (m)
T_E	Wave encounter period (s)
T_F	Draft at fore perpendicular (m)
T_{spring}	Spring natural period (s)
U	Ship velocity (m/s)
u	Axial velocity component of ship wake (m/s)
V_{CG}	Vertical position of center of gravity from keel (m)
x	Surge motion (m)
x_i	The ith harmonic amplitude of surge motion at wave encounter frequency (m)
x_{1_s}	The 1st harmonic amplitude of surge motion at spring natural frequency (m)
X_{prop}	Longitudinal position of propeller center forward aft perpendicular (m)
y^+	Non-dimensional wall distance for a wall-bounded flow (–)
z	Heave motion (m)
z_i	The ith harmonic amplitude of heave motion at wave encounter frequency (m)
Z_{prop}	Vertical position of propeller center under water line (m)
$N_{cell\,i}$	Total number of cells of the ith grid in uncertainty analysis tool
$R_{T\,i}$	The ith harmonic amplitude of total resistance at wave encounter frequency (N)
v	Transversal velocity component of ship wake (tangential to the plane of study in Y, in which axial velocity component is defined on) (m/s)
w	Vertical velocity component of ship wake (tangential to the plane of study in Z, in which axial velocity component is defined on) (m/s)

propeller, rudder and engine) in such environmental and operational conditions. These turn the full analysis of ship performance in waves into an extremely cumbersome, if not impossible, task. However, from a hydrodynamics engineering perspective, the focus lies on understanding the physical phenomena associated with fluid flow and their impacts on ship performance in waves. Therefore, as with any engineering approach, it is essential to simplify the problem in the initial step and comprehend the underlying physical phenomena in simplified scenarios before extending the analysis to more complex circumstances.

A proper candidate for the initial stages of investigations in waves is to study ships' bare hull operating in regular head waves. This choice is

based on the comparatively simpler impacts of regular head waves on the bare hull hydrodynamic performance and the involved flow physics, e.g., initiating primarily surge, heave and pitch, as the key entailed motions. Through comparison of the bare hull behavior in regular head waves to that of calm water, the effects of such waves on the bare hull hydrodynamic responses can be examined and a general overview of the physical aspects for different contributing factors can be obtained. This can be counted as a crucial step towards understanding the propeller-hull interaction effects in regular head waves later on, as a more complex scenario.

Ships' bare hull performance in regular head waves has been widely investigated experimentally and numerically. The common experimental approaches, which are known as Experimental Fluid Dynamics (EFD), are the model tests with different Degrees of Freedom (DOF) in towing tanks or seakeeping basins as noted in ITTC (2017b). Although these model tests are expensive and time-consuming, the ship's added resistance and motions are expected to be predicted with a high level of accuracy from the measured motions and towing force. Many examples of such model tests can be found in literature such as Irvine et al. (2008), Guo and Steen (2011), Simonsen et al. (2013), Kim (2014), Park et al. (2015), Kim et al. (2017), Lee et al. (2017), Yu et al. (2017), Hossain et al. (2018), Shivachev et al. (2020) and Seo et al. (2020). Additionally, further experimental measurements can be found in the assessments of the workshops on numerical ship hydrodynamics by Larsson et al. (2014) and Hino et al. (2021), as well as in the SHOPERA project investigations presented by Papanikolaou et al. (2016) and Sprenger et al. (2017). The main focus of such model tests was to investigate the added resistance and motions in regular head waves, with few conducting local flow measurements. The scarcity of local flow measurements for the model tests in regular head waves can be attributed to the intricacy involved in such measurements. This complexity stems from the necessity of specialized equipment, test setups and analysis techniques, as well as the interference of the ship wake with the measurement devices.

Since the 1950s, various computational seakeeping methods have emerged. Bertram (2012) has presented a structured overview of the most well-known methods. Generally, one major advantage of numerical methods over model tests is the possibility of acquiring in-depth information about the fluid flow, which is challenging, costly and extremely cumbersome to achieve through model tests. Each numerical method has a different level of fidelity with respect to its computational costs and accuracy. Generally, the approach in these methods is based on either Potential Flow methods (Strip Theory or Three-Dimensional Panel Methods) or Computational Fluid Dynamics (CFD) techniques.

Usually, potential flow solvers are computationally much faster than CFD solvers. In potential flow methods, the flow is assumed to be inviscid, incompressible and irrotational. In the cases where the viscous effects are insignificant, the application of potential flow methods may provide a great advantage in terms of computational efficiency. Contrary to potential flow methods, the state-of-the-art CFD methods have the advantage of predicting ship hydrodynamic performance more accurately by performing high-fidelity nonlinear computations with fewer simplifications related to flow physics. However, these methods are computationally expensive and time-consuming. The most common CFD methods in the context of ship hydrodynamics are based on the so-called Reynolds-Averaged Navier–Stokes (RANS) approach.

Today, with the development of advanced computational tools and the availability of large computational resources, the application of CFD methods for the investigations of ship performance in waves is gradually gaining more popularity. Given that the investigation in this paper focuses not only on the ship resistance and motions but also its nominal wake, the usage of a CFD method is motivated since it is capable of predicting the complex interactions between the boundary layer and incoming waves and providing comprehensive flow field information, which is not feasible in potential flow methods.

From the application of CFD for practical calculations of complex flows, a quality assessment commonly denoted as Verification and Validation (V&V) is required to establish the credibility of the results, (Eça and Hoekstra, 2014). Verification is a purely mathematical exercise that intends to show that we are solving the equations right, whereas validation is an engineering practice that intends to show that we are solving the right equations, (Roache, 1998). Therefore, validation exercises deal with modeling errors which indicate the discrepancy between the simulated results and the analytical/experimental results. The modeling errors have a sign which can be either positive or negative. However, verification exercises address the numerical uncertainties which are represented by intervals (a plus-minus sign) containing the exact solution with a certain degree of confidence, (Eça and Hoekstra, 2014).

Numerous examples of using CFD methods for analyzing the ship's bare hull performance in regular head waves can be found in literature, for instance, in the investigations by Carrica et al. (2007), Castiglione et al. (2011), Ye et al. (2012), Simonsen et al. (2013), Shen and Wan (2013), Wu et al. (2014), Moctar et al. (2016), Seo et al. (2017), Ozdemir and Barlas (2017), Kim et al. (2017), Chen et al. (2018), Lee et al. (2019), Shivachev et al. (2020), Saettone (2020), Wu et al. (2020), Lee et al. (2021a,b), Gao et al. (2021), Islam and Guedes Soares (2022), Lee et al. (2022), Lungu (2022) and Mikkelsen et al. (2022). However, there are various shortcomings in these investigations as listed below.

- The majority of studies primarily concentrate on resistance and motions, while giving limited attention to the analysis of propulsion performance in relation to the nominal wake in waves. The choice of turbulence model also can be debated. Pereira et al. (2017) mentioned that the turbulence models that lead to the smallest modeling errors in the resistance are not the same as those that lead to the smallest modeling errors in the prediction of the flow field at the propeller plane.
- Although the effects of surge motion on added resistance are assessed to be relatively low, as noted by Sadat-Hosseini et al. (2013), surge motion can play a crucial role in the coupling between motions as well as the variation of nominal wake at propeller plane. Most of the aforementioned studies have been conducted for ships free to heave and pitch (2DOF), overlooking the necessity of considering surge motion when investigating the wake characteristics.
- The numerical uncertainties of the simulations in regular head waves are not often assessed which results in a lack of reliability assessment. This is mainly due to the high computational costs involved in simulations with finer grids or smaller time steps. Even when numerical uncertainty investigations are conducted, certain studies have neglected to provide in-depth explanations regarding the fulfillment of the employed uncertainty method requirements, such as grid similarity requirements for unstructured grids. This lack of clarity raises doubts about the credibility of the obtained numerical uncertainty results.
- Finally, most of these investigations suffer from a proper validation of wake characteristics, mainly due to the unavailability of experimental wake measurements.

In addition to the aforementioned investigations, there are four studies in literature by Guo et al. (2012), Sadat-Hosseini et al. (2013), Sigmund (2019) and Shin et al. (2020), which are very relevant to the current paper, hence reviewed in the following.

Guo et al. (2012) used a RANS approach to study resistance, motions and nominal wake of KVLCC2 tanker in regular head waves, including a grid convergence study on the ship resistance and motions in waves. However, the surge motion was fixed in this investigation and there were no validations carried out for the computed wake. Nonetheless, interesting observations such as strong effects on the ship wake due to the ship performance in regular head waves are reported. Large variations of the axial and non-axial velocity components of the wake

Table 1
Model-scale KVLCC2 vessel bare hull and propeller main particulars (scale factor = 100).

Symbol	Value	Unit	Denotation
Bare Hull			
L	3.2	(m)	Length between perpendiculars
B	0.58	(m)	Breadth at mid-ship
T_F	0.208	(m)	Draft at fore perpendicular
T_A	0.208	(m)	Draft at aft perpendicular
∇	0.312622	(m^3)	Volume displacement
Δ	312.028	(kg)	Mass displacement
S	2.7194	(m^2)	Bare hull wetted surface area at rest
C_B	0.8098	(–)	Block coefficient
L_{CG}	1.71136	(m)	Longitudinal position of COG from aft perpendicular
V_{CG}	0.186	(m)	Vertical position of COG from keel
K_{yy}	0.8	(m)	Mass radius of gyration around Y-axis (pitch)
Propeller - KP458 (based on Osaka University Towing Tank model setup)			
D_{prop}	0.0986	(m)	Propeller diameter
D_{hub}	$0.155D_{prop}$	(m)	Hub diameter
X_{prop}	$0.02L$	(m)	Longitudinal position of propeller center forward aft perpendicular
Z_{prop}	$0.046875L$	(m)	Vertical position of propeller center under water line

are reported during one encounter period of waves, however, the correlations between different factors and the possible effects on the propulsion performance are not discussed.

The investigations carried out by Sadat-Hosseini et al. (2013), which are further analyzed in Wu (2013) Ph.D. thesis and Wu et al. (2016), encompass a wide range of crucial aspects of a bare hull performance in regular head waves. The studies are conducted for KVLCC2 both in fixed and free surge conditions, including numerical uncertainty analyses in regular head waves. The wake validation is performed using 2-Dimensional Stereo Particle Image Velocimetry (SPIV) measurements. Although the variation of the nominal wake is discussed briefly, the correlation of different contributing factors to the transient wake and the effects on the propeller loading and propulsive performance are not examined in detail.

In the Ph.D. thesis by Sigmund (2019), a systematic RANS investigation of the ship performance in waves is carried out in order to study ship motions, resistance and propulsion performance in waves for four different ship types. The discretization errors were evaluated by performing grid studies. The computations and measurements correlated favorably for resistance and motions, however, no wake validation was carried out. It is concluded that the change of the time-averaged wake fraction in waves depends on the hull form and the position of the propeller, whereas the oscillation amplitudes of the wake fraction in waves depend on the wave parameters. Nominal wake fraction is found to oscillate significantly in waves and averaged values are decreased. However, there is no detailed investigation carried out to study the correlation of different contributing factors to the transient wake.

The most relevant study on the change of nominal wake in regular head waves is carried out by Shin et al. (2020) for the KVLCC2 tanker in which a good agreement is observed against the experimental SPIV measurements. The effect of the ship motions on the characteristics of the wake field and the axial velocity at the propeller plane are investigated in different wave conditions. However, the investigations are carried out in the fixed surge condition (2DOF) and the uncertainty analysis is only carried out for the calm water simulations and not in regular head waves. In all of the studied wave conditions, the mean axial velocity component of the nominal wake is increased in comparison to the calm water condition. The interruption of the inflow to the propeller plane is explained by the behavior of the vortices at the stern due to large motions which may result in fluctuation and hence degradation of the propulsion performance.

The lack of a single study incorporating all the aforementioned factors in order to understand the performance of a bare hull in regular head waves is the main motivation for the current investigations. The main objective of the current paper is to perform numerical (RANS) investigations of a bare hull, free to surge, heave and pitch, operating in calm water and regular head waves in order to:

- evaluate one of the state-of-the-art computational tools used for simulating ship performance in head waves;
- analyze the ship resistance, motions and nominal wake as well as the correlations between them;
- identify the discrepancies between the behavior of a bare hull in waves relative to calm water;
- provide guidance to naval architects concerning ship seakeeping performance in regular head waves and deliver flow field analyses to aid ship and propeller designers in optimizing their designs under conditions beyond calm water.

To this end, suitable convergence criteria and post-processing techniques are utilized and then a formal verification and validation (V&V) procedure is applied to understand and control the numerical and modeling uncertainties/errors in the CFD computations. In this paper, the main focus of such verification (uncertainty analysis) is on systematic grid convergence study. The verification and validations are performed for the dominant harmonic amplitudes of the ship resistance, motions and nominal wake in both calm water and regular head waves and the differences between these operational conditions are highlighted in this paper. The findings can also be used for evaluating simplifications commonly adopted in lower fidelity methods like potential flow methods. The KVLCC2 tanker is chosen as the case study in this paper and the available local flow measurements (SPIV) are used to validate the computed nominal wake. The correlations between the wake variations and the ship motions as well as the possible consequential effects on the propeller loading considering both the wake and resistance during the ship performance in regular head waves are investigated.

2. Vessel geometry and operational conditions

The KVLCC2 bare hull in model-scale (scale factor = 100) appended with a shaft (dummy hub) is employed in this study. The ship main particulars in the fully-loaded operational condition are given in Table 1. Since the nominal wake analysis is carried out mainly at the propeller plane/disk, the particulars of the propeller are also provided in Table 1.

The hydrodynamic performance of the vessel operating in fresh water with the density of $\rho = 998.1$ kg/m^3 and the kinematic viscosity of $\nu = 1.002 \times 10^{-6}$ m^2/s is investigated at the ship design speed (Froude number of $Fr = U/\sqrt{gL} = 0.142$), hence Reynolds number of $Re = UL/\nu = 2.546 \times 10^6$. The investigations are carried out in calm water and in three regular head waves with the same wave height $H = 0.06$ m and three different wave lengths $\lambda/L = 0.6$, 1.1 and 1.6. The wave encounter frequency ω_E and encounter period T_E can then be computed for each wave length based on its respective wave frequency ω_w and the heading angle $\mu = 180°$ as,

$$\omega_E = \omega_w - \frac{{\omega_w}^2 U}{g}\cos(\mu), \qquad T_E = 2\pi/\omega_E. \tag{1}$$

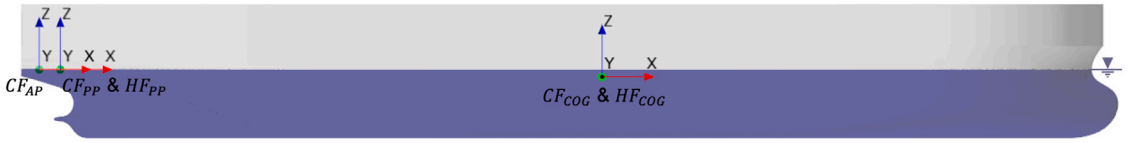

Fig. 1. Initial locations/orientations of the considered coordinate systems.

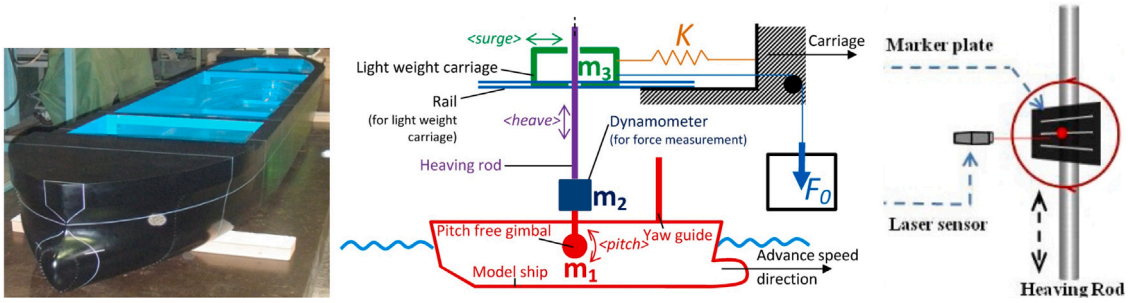

(a) KVLCC2 model. (b) Test setup. (c) Heave synchronizer.

Fig. 2. KVLCC2 model, experimental setup for free surge conditions and heave synchronizer system for SPIV trigger in EFD_1.
Source: Adapted from Kim (2014).

Two reference frames are considered: a carriage-fixed reference frame (CF) and a hull-fixed reference frame (HF). The carriage-fixed reference frame is considered to move in longitudinal direction with the ship design speed, while, the hull-fixed reference frame follows the ship motions and its instantaneous speed. Several Cartesian coordinate systems are defined in each of these reference frames. These coordinate systems at the initial position of the ship are shown in Fig. 1. The coordinate systems are defined at the initial positions of ship Center of Gravity (COG), Propeller Plane (PP) or Aft Perpendicular (AP). For instance, one coordinate system in each reference frame is defined at the ship initial position of COG, which are named as CF_{COG} and HF_{COG}. Both coordinate systems initially have X-axis pointing towards the ship advancing direction, Y-axis towards portside and Z-axis pointing upwards. While the axes directions always remain the same for the coordinate system in the carriage-fixed reference frame (CF_{COG}), they change based on the instantaneous ship motions for the coordinate system in the hull-fixed reference frame (HF_{COG}).

The ship motions are defined at COG with respect to the coordinate systems in the defined reference frames. Consequently, positive surge motion occurs when the COG moves in the direction of the ship's forward speed, i.e., when HF_{COG} moves forward of CF_{COG} in the longitudinal direction. Heave will be positive when the COG moves upwards and pitch will be positive when the ship's bow moves downwards (or stern moves upwards).

The transient wake of the ship is investigated in two different planes: one at the aft perpendicular and one at the propeller plane. Therefore, three extra coordinate systems (CF_{AP} and CF_{PP} in the carriage-fixed reference frame and HF_{PP} in the hull-fixed reference frame) are defined similar to the aforementioned coordinate systems at COG but with the origins at the initial ship design waterline and longitudinal position of the plane, see Fig. 1. All the carriage-fixed coordinate systems move with the constant ship design speed in the longitudinal direction irrespective of the ship instantaneous speed or its motions.

3. Experimental method

The presented test results are from an extensive test campaign led by Osaka University Towing Tank (OU). In this paper, the data is divided into two main data sets (called EFD_1 and EFD_2 henceforth). Detailed information for EFD_1 can be found in Hayashi (2012), Wu (2013), Sadat-Hosseini et al. (2013) and Kim (2014). The more recent data set EFD_2 is reported by Mwangi (2021). The experimental setups were relatively similar in these data sets. A wooden KVLCC2 model (scale factor = 100) was used, see Fig. 2(a). Moreover, 2-Dimensional Stereo Particle Image Velocimetry (SPIV) system was used to measure the flow velocity distribution at different planes.

The model tests were carried out in 3 Degrees of Freedom (3DOF) in which the model was free to surge, heave and pitch. In such tests, the model was free to surge while it was towed with a light-weight carriage connected to the main carriage through a weak spring system, as sketched in Fig. 2(b). The spring stiffness $K = 98$ N/m was chosen to avoid resonance and interference of the spring natural frequency with surge motion frequency in waves. Because of the spring system, an external constant force F_0 (obtained through a set of preliminary tests) is needed to keep the calm water surge and the mean surge in waves close to zero. F_0 and K were emulated by a servo motor. Unfortunately, the applied F_0 is not available in any of the reports from the experiments.

A pitch free gimbal was installed in the hull COG and connected to the carriage by a heaving rod. A load cell dynamometer was installed above the gimbal for force measurements. The hull motions were measured using three potentiometers and the incident wave height was measured by a servo type wave gauge installed on the carriage at some distance in front of the initial position of model (4.425 m in front of the heaving rod in EFD_1 and 3.52 m or 3.314 m in front of fore perpendicular depending on the test type in EFD_2). In both data sets, it is mentioned that the actual measured incident wave height at some tests was different from the target ones, possibly due to the performance of the wave generator and wave dampener systems in the tank. This will be addressed later. The sampling rate of the equipment was 100 Hz.

The experimental setup involved the masses of the hull and pitch-free gimbal ($m_1 = 306.2$ kg) as well as the dynamometer mass ($m_2 = 6.4$ kg), that all contributed to the hull motions ($m_1 + m_2 \approx \Delta$). However, the mass of the light-weight carriage ($m_3 = 2.5$ kg) only affected the surge motion.

The SPIV system was fixed on the carriage, so the model moved around the original position with the wave encounter frequency and the spring natural frequency. The details of the experimental SPIV setup and equipment can be found in the aforementioned references for each data set. This system can take particle images not only at specific intervals but also at specific moments regulated by an external

trigger. The operational conditions, measurement planes and triggers were different in different data sets. These discrepancies are further elaborated in the subsequent sections.

3.1. SPIV in EFD_1

In EFD_1, no information is found about the water temperature, hence the Reynolds number in this data set is assumed to be equal to the design value. The plane of measurements in this data set was fixed on the carriage at the initial position of the propeller plane (CF_{PP} in Fig. 1).

Unfortunately, the raw SPIV data is not accessible for calm water in free surge (3DOF) condition in EFD_1. Instead, another measurement from the OU test campaign for KVLCC2 in calm water is used in this paper, in which the model was fixed but with predefined sinkage and trim setup, provided in Win et al. (2016).

In waves, the trigger of the SPIV system was set in accordance with the phase of the heave motion. The SPIV measurements were carried out in all three wave lengths. The goal was to capture the wake at heave phases of 0°, 45°, 90°, 135°, 180°, 225°, 270° and 315° in $\lambda/L = 0.6$, as well as phases of 0°, 30°, 60°, 90°, 120°, 150°, 180°, 210°, 240°, 270°, 300° and 330° in $\lambda/L = 1.1$ and phases of 0°, 60°, 120°, 180°, 240° and 300° in $\lambda/L = 1.6$. A heave synchronizer system was introduced in order to find such heave phases during the test runs. Heave was chosen because of its relatively stable behavior during different runs. The system included a laser sensor fixed on the towing carriage and a marker plate installed on the heaving rod following the heave motion of the hull, see Fig. 2(c).

A series of parallel horizontal lines were marked on the marker plate (representing different heave phases) in order to be detected by the laser sensor and hence sending a signal to trigger the SPIV measurements. In EFD_1, approximately 200 frames were averaged to obtain each phase of the SPIV data in waves.

In order to find the location of the phase lines on the marker plate, preliminary experiments were carried out to determine the heave mean and first harmonic amplitude in each wave length. Then, the center line was set to capture the heave mean value and the location of other phase lines was derived by calculating the expected instantaneous heave motion $z_{plate} = \bar{z}_{plate} + z_{1_{plate}} \sin(\phi_{desired})$ using the results of the preliminary experiments. $\bar{z}_{plate}$ was found to be −0.0030 m, −0.0030 m and −0.0028 m and $z_{1_{plate}}$ was found to be 0.0025 m, 0.0193 m and 0.0256 m for $\lambda/L = 0.6$, 1.1 and 1.6, respectively. It is very important to notice that the heave motions might change during each run (e.g., depending on the actual incident wave propagating in the tank) and the actual measured heave might differ from the expected one. This could potentially introduce uncertainty to the actual instances of SPIV measurements.

3.2. SPIV in EFD_2

In EFD_2, it is very important to note that the tests in which the motions and resistance were measured are different from those of SPIV measurements. This may introduce a source of uncertainty into the measurements in this data set, as the response of the hull might be different in different conditions. Moreover, the water temperature for the motion and resistance measurements and hence the respective Reynolds number ($Re = 1.9141 \times 10^6$) were different from those for SPIV measurements ($Re = 2.2519 \times 10^6$). The plane of measurements in this data set was fixed on the carriage at the initial position of the aft perpendicular (CF_{AP} in Fig. 1). The plane was re-positioned from the propeller plane to the aft perpendicular to eliminate any disruptive reflections from the dummy hub.

The calm water SPIV measurements were carried out in fixed surge conditions (2DOF) and approximately 230 velocity distribution images were collected and averaged. The calm water measurements were at $Re = 2.6159 \times 10^6$.

In waves (3DOF), the trigger in the SPIV system was based on the measured wave height at the wave gauge installed at a certain distance in front of the initial position of the model. The SPIV measurements in waves were only performed for $\lambda/L = 1.1$ and 1.6 in EFD_2. The trigger was based on the incident wave elevation at the wave gauge at 4 phases of 0° (zero up crossing of wave at wave meter), 90°, 180° (zero down crossing of wave at wave meter) and 270° for each λ/L. The wave gauge location was different in the tests for measuring motions and resistance (3.52 m in front of the fore perpendicular) compared to the SPIV measurements (3.314 m in front of the fore perpendicular). For each phase, the measurements were carried out in two runs in which the measurement plane was moved vertically to cover a larger area due to the large ship motions relative to the carriage. Approximately 180 images were collected and averaged for each phase. One source of uncertainty in this data set raise from the fact that the occurring wave elevation may differ from the expected value in some tests, which might affect the timing for triggering the SPIV.

4. Numerical method

The governing equations of a fluid flow are the so-called continuity and Navier–Stokes equations, which are referred to as the Navier–Stokes equations henceforth. These equations are a set of non-linear partial differential equations derived from the basic laws of mass and momentum conservation. The Reynolds-Averaged Navier–Stokes (RANS) equations of incompressible viscous flow for Newtonian fluids in three dimensions can be expressed as,

$$\frac{\partial \overline{U_i}}{\partial x_i} = 0,$$

$$\frac{\partial \overline{U_i}}{\partial t} + \overline{U_j}\frac{\partial \overline{U_i}}{\partial x_j} = -\frac{1}{\rho}\frac{\partial \overline{P}}{\partial x_i} + \nu\frac{\partial^2 \overline{U_i}}{\partial x_j \partial x_j} + g_i - \frac{\partial \overline{u_i u_j}}{\partial x_j}, \tag{2}$$

which are derived from inserting the Reynolds decomposition of velocity and pressure by time-averaged ($\overline{U_i}$ and $\overline{P}$) and fluctuating (u_i and p) quantities as,

$$U_i = \overline{U_i} + u_i, \qquad P = \overline{P} + p, \tag{3}$$

into the Navier–Stokes equations. i and j represent the coordinates, U_i is the ith component of the velocity vector U, t is time, ρ is the density, P is the pressure, ν is the kinematic viscosity of the fluid and g_i is the gravitational acceleration which is assumed to be the only existing body force in this equation. In the current study, the Reynolds Stress Tensor $\overline{u_i u_j}$ is modeled by an Eddy Viscosity model, i.e., Boussinesq approximation, to provide the closure equation for the partial differential equations. Therefore, $\overline{u_i u_j}$ is assumed to be proportional to the mean strain rate tensor. The original Boussinesq approximation implies a linear constitutive relation as,

$$-\overline{u_i u_j} = \nu_t\left(\frac{\partial \overline{U_i}}{\partial x_j} + \frac{\partial \overline{U_j}}{\partial x_i}\right) - \frac{2}{3}k\delta_{ij}, \tag{4}$$

in which ν_t is the turbulent viscosity, δ_{ij} is the Kronecker delta and k is the turbulent kinetic energy. The turbulent viscosity as the factor of proportionality can be derived by solving additional transport equations for extra scalar quantities.

In this study, the numerical simulations are performed by a commercial CFD solver, Simcenter STAR-CCM+ (version 2020.3), using a RANS approach. The continuous equations are discretized using a Finite Volume method. A segregated approach for coupling velocity and pressure fields is used for solving the conservation equations for mass, momentum as well as turbulence quantities. A second-order spatial discretization scheme is used.

The turbulent viscosity is modeled using the $k-\omega$ SST turbulence model (using all y^+ wall treatment) via solving additional transport equations for turbulent kinetic energy k and specific dissipation rate ω.

The implementation of this turbulence model in STAR-CCM+ is based on Menter (1994). In order to take into account the anisotropy of the turbulence, the linear Bossenisque approximation, given in Eq. (4), is extended by adding nonlinear functions of the strain and vorticity tensors to derive a quadratic constitutive relation. For more details see *Simcenter STAR-CCM+ User Guide* (2020).

The Volume of Fluid (VOF) multiphase model is used as the free surface capturing technique. The High-Resolution Interface Capturing scheme (HRIC) by Muzaferija and Peric' (1998) is used in VOF simulations to maintain a sharp interface between the incompressible fluid phases. For the regular head wave simulations, the 5th order Stokes waves are considered, as they were found to be a better resemblance of the real-world waves, (Fenton, 1985).

Obtaining high-quality regular waves is a well-known challenge in both experimental tests as well as numerical simulations, ITTC (2021a,b) and Tavakoli et al. (2023). In order to investigate the modeling errors involved in the simulation of wave propagation and achieve a robust simulation setup for wave propagation in STAR-CCM+, a comprehensive study has been performed by Irannezhad (2022). The aim was to minimize the modeling errors of wave propagation (e.g., amplitude reduction and period change during propagation, disturbances (wiggles) on the free surface and reflection at boundaries) and compare the discrepancies from the analytical wave. The main excitation forces on the ship are exerted by the waves, so a better understanding of errors in wave propagation modeling can explain the behavior of the ship in waves. For instance, it is shown by Sigmund (2019) and Irannezhad et al. (2022) that when the effects of actual measured wave height in model tests are taken into account, the validation errors for the non-dimensional resistance and motions considerably decrease in comparison to the dimensional ones.

To ensure consistency with the hull performance simulations conducted in the current paper, the wave propagation simulation setups in Irannezhad (2022) were designed to closely resemble those used for the hull performance simulations. It was presumed that the steepest wave is the most critical wave for numerical wave propagation modeling, hence only the wave with a length of $\lambda/L = 0.6$ was considered in the wave propagation simulations in an empty domain.

As it is mentioned by Perić and Abdel-Maksoud (2018, 2020), Berndt et al. (2021) and Perić et al. (2022) case-dependent parameters should be tuned for minimizing the reflections from the boundaries of the computational domain and improving the numerical simulations of flows with free surface waves. Therefore, different user-defined parameters (e.g., the angle factor of 0.15 under the HRIC scheme which affects the discretization of the volume fraction) were tuned in the aforementioned preliminary wave propagation simulations in Irannezhad (2022). In these simulations, the effects of different local refinement zones as well as the quality of the cell size and overset interpolations in the overlapping zones were evaluated. The numerical configuration proposed in Irannezhad (2022) yielded numerical waves that closely resembled the theoretical counterpart, with discrepancies in the 1st harmonic amplitude (i.e., the dominant component) remaining mainly below 3%.

4.1. Motion modeling

In order to simulate the vessel motions, the Dynamic Fluid Body Interaction (DFBI) module in STAR-CCM+ is used. The DFBI Rotation and Translation model is used in order to enable the RANS solver to compute the vessel motions from the fluid excitation forces and moments as well as the body forces. In 3DOF simulations, for numerical replication of the spring and light-weight carriage effects which were present in the experiments, two external forces one for constant force F_0 and one varying spring force $-Kx-m_3\ddot{x}$ are applied at the COG in the ship advancing direction. K is the spring stiffness, x is the instantaneous surge motion and $\ddot{x}$ is the instantaneous surge acceleration.

Since F_0 is not available from the experiments, an estimated F_0 is considered in each operational point (i.e., approximately close to the total resistance of the ship) in order to prevent a large mean surge value. This can be counted as a significant source of discrepancy and will be discussed further in the paper.

In the simulations, a symmetry boundary condition is considered at the ship centerline plane $Y = 0$, hence the experimental values of the spring stiffness K and light-weight carriage mass m_3 are divided by two in the simulations and F_0 is approximated for a half ship. It should be noticed that when the surge has a positive value based on the considered coordinate systems shown in Fig. 1, the spring force $-Kx$ gets a negative value (in the opposite direction of the ship forward speed) as the spring is compressed, see Fig. 2(b). In the simulations, the spring force in each time step is calculated based on the surge motion obtained from the previous time step and applied as an external force at COG.

To ensure a smooth and stable start to the simulations, it is crucial to avoid any abrupt acceleration or large amplitudes of surge motion (i.e., large spring force), as it takes a very long time to dampen the resultant oscillations and thus increased computational costs. Therefore, relatively long Release and Ramp times are considered under DFBI model. Release time in the DFBI model is defined as the duration before the calculation of body motion begins. This allows the flow to stabilize, thereby stabilizing the force and moments acting on the body. Ramp time is the duration after Release time in which the forces and moments acting on the body gradually come into play in the calculation of the hull dynamics.

Finally, the hull is assumed to be rigid, hence its flexibility and hydroelasticity are deemed negligible.

4.2. Grid generation

Unstructured grids including the trimmed hexahedral meshes with local refinements near the free surface and near the hull as well as prism layer meshes along the hull surface are generated using STAR-CCM+ automatic mesh generator. The computational domain is discretized employing an Overset Topology which consists of an overset region and a background region with specific treatment of cell sizes near the overlapping zone (where the information is exchanged between the background and overset regions). Often, it is more computationally efficient to have a narrower local refinement zone close to the free surface for calm water simulations and a wider one for regular head wave simulations. However, in this study, we opted to use the same grid for both calm water and regular head wave simulations to diminish inconsistencies between these simulations. The same is considered in the Ph.D. thesis by Sigmund (2019).

The uncertainty analysis is carried out with the main focus on systematic grid convergence study. In order to perform a valid grid convergence study, several progressively refined grids should be generated where all grids should be exactly "geometrically similar", noted by Eça et al. (2016). However, generating geometrically similar unstructured grids for complex geometries is extremely cumbersome, if not impossible, as explained by Eça and Hoekstra (2014). Therefore, in the current investigations, different cautions are taken into account to eliminate/diminish undesired grid refinement diffusion depths (transition zone between two local refinement zones) and also to generate a "as geometrically similar as possible" set of unstructured grids.

Five systematically refined grids are generated which are determined by the refinement levels $n = 0.75$ (coarsest), 1.00, 1.25, 1.50 and 2.00 (finest). It is worth mentioning that the investigations are also carried out for an additional coarser grid with $n = 0.50$, however, it was found that such grid is incapable of capturing the main flow features and hence its results significantly deviated from the other girds and thus far from the asymptotic range. Therefore, the results of that grid are excluded in the current paper.

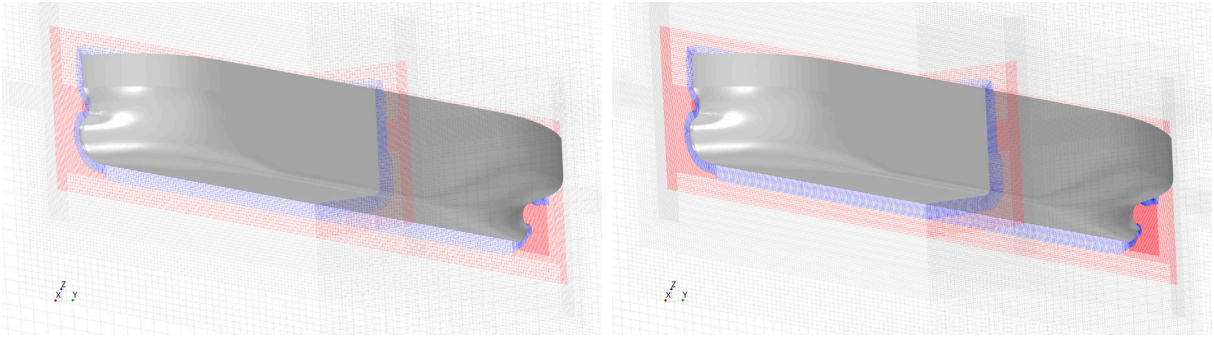

(a) n = 1.00. (b) n = 1.50.

Fig. 3. Overview of the grids near the hull. Gray lines represent the mesh in the background region. Red and blue colors represent the isotropic and prism layer meshes in the overset region, respectively.

Trimmed hexahedral meshes (isotropic volume meshes) are generated in both background and overset regions. For isotropic volume meshes, every two neighboring cells with the same size in the grid $n = 1.00$ are converted into $2n$ cells in each direction (X, Y and Z), hence substituted by $2n^3$ cells. Strict cautions were taken into account for defining the dimensions of different local refinement zones and the number of neighboring similar cells in each direction in each local refinement zone in order to fit an integer number of cells in each direction as a result of multiplication $2n$ and force the local refinements to occur exactly in the defined local refinement zones. Besides such precautions, the refinement ratios between the local refinement zones are defined in order to prevent any missing/extra refinements from the grid generator, hence generating geometrically similar isotropic volume meshes. However, some undesired transition zones occur for $n = 0.75$ and 1.25, therefore, these grids are not exactly geometrically similar (but marginally different) to the other ones in terms of the isotropic volume meshes.

In order to achieve geometrically similar anisotropic sub-layer (prism layer) meshes, the methodology presented by Crepier (2017) is complied. In this method, the total thickness of prism layers remains the same between the grids but both the first layer cell thickness δ and the growth ratio between the layers γ are adjusted accordingly as,

$$\delta_n = \delta_1 \frac{1-\gamma_1{}^{\frac{1}{n}}}{1-\gamma_1}, \qquad \gamma_n = \gamma_1{}^{\frac{1}{n}}, \tag{5}$$

in which δ_1 and γ_1 are the first layer cell thickness and the growth ratio for the grid $n = 1.00$. As a result, the total number of layers in each grid will be $N_n = nN_1$, in which N_1 is the total number of layers for grid $n = 1.00$. It was thus very important to choose a proper N_1 to have an integer number of layers for all grids deriving from nN_1 multiplication. An overview of the grids near the hull for two refinement levels is shown in Fig. 3.

The prism layers are generated such that the non-dimensional wall distance y^+ remains above 30 and under 300 over the major part of the hull wetted surface area during the simulations for all grids, hence a wall function is utilized for the treatment of the near-wall region.

Although an effort has been made to generate a geometrically similar isotropic and anisotropic set of grids, the undesired transition zone between the prism layers and their neighboring isotropic cells is inevitable. Moreover, the geometry is captured with a higher quality in the finer grids, which results in geometrical differences between prism layers for different grids. Therefore, the grids are "as geometrically similar as possible". Consequently, the total number of cells are 3 591 204, 7 868 343, 16 101 857, 26 542 361 and 62 866 494 for $n = 0.75$, 1.00, 1.25, 1.50 and 2.00, respectively. The total number of cells for each refinement level is roughly $7\,868\,343n^3$. The calm water simulations as well as the simulations in regular head waves of $\lambda/L = 0.6$ and 1.1 are carried out in all five refinement levels (including a grid convergence study), while the simulations for the longest wave $\lambda/L = 1.6$ is only carried out in grid $n = 1.00$.

From the free surface local refinement zone, based on the refinements in the vertical Z direction, $10n$ cells per wave height H are considered for each grid. The cell aspect ratio in longitudinal X and transversal Y directions relative to the vertical Z direction is set to be 4. Therefore, the cell size in Z and X directions are $H/(10n)$ and $4H/(10n)$, respectively. Consequently, there are $10n\lambda/(4H)$ cells per wave length for each wave in each grid.

4.3. Computational domain

An overview of the computational domain size and the imposed boundary conditions are shown in Fig. 4. A wave forcing function is used in the vicinity (distance equal to L) of all vertical boundaries with velocity inlet boundary conditions. The aim is to force the solution of the discretized Navier–Stokes equations, for simulations in regular head waves, towards the theoretical 5th order Stokes wave solution, and for calm water simulations, towards the still water solution, hence minimizing the wave reflection from the boundaries.

In order to analyze the numerical free surface elevation, a wave probe is positioned in front of the ship's fore perpendicular, right at the end of the forcing zone. Although the actual incident wave may vary in comparison with the wave at the wave probe, this is the only feasible approach for monitoring the waves near the hull, as the hull and its motions can significantly affect the free surface elevation in the hull vicinity. On the other hand, based on the investigations carried out in Irannezhad (2022), insignificant deviations are expected with the current simulation setup.

In the preliminary investigations, a Distance Weighted overset interpolation scheme was employed. However, later it was found that the quality of the interpolations was rather poor, resulting in nonphysical vortices at the overlapping regions which significantly affected the predicted forces acting on the hull. It was then found that higher order schemes are required to improve the quality of interpolations, (Lemaire et al., 2021). Therefore, the Least Square interpolation scheme is employed within the overset topology which marginally increases the required computational costs but introduces higher accuracy interpolations compared to the Distance Weighted scheme. More details about the aforementioned interpolation schemes can be found in *Simcenter STAR-CCM+ User Guide* (2020).

4.4. Time step

An implicit unsteady solver is used with a second-order temporal discretizational scheme (time step $\Delta t = 0.003$ s/n, hence similar Courant number between the grids). The chosen time step results in Courant numbers smaller than 0.3–0.4 on the free surface which is in line with

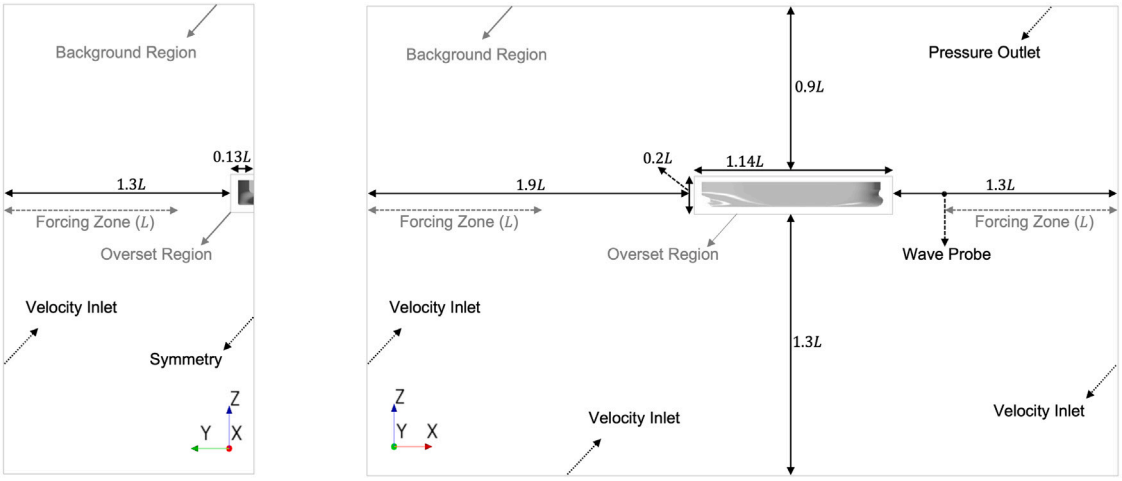

Fig. 4. Computational domain size, applied boundary conditions and wave probe location.

the best practices for numerical wave propagation and also fulfills the ITTC (2014) recommendations. The maximum number of inner iterations per time step is set to 20.

The uncertainty analysis in this paper concerns the grid convergence study, while a complete uncertainty analysis would include the combination of iterative and grid convergence studies. Therefore, conservative values are chosen for the time step size and the maximum number of inner iterations to minimize the dependency of the results on the time step. The choice of time step was also evaluated by running a selective set of operational conditions and grids with a substantially smaller time step. However, no significant alteration was observed in the solutions. Additionally, as stated above, the time step is modified for each grid refinement to ensure the same Courant number between the grids.

4.5. Uncertainty analysis method

In this paper, the numerical uncertainty analysis tool developed by Eça and Hoekstra (2014) and Eça et al. (2019) is employed to carry out the grid convergence study in calm water and regular head waves. In this tool, first, the discretization error is estimated with power series expansions as a function of the typical cell size h_i defined as,

$$h_i/h_1 = \sqrt[3]{N_{cell\,1}/N_{cell\,i}}, \tag{6}$$

in which $N_{cell\,i}$ is the number of cells for the grid i and $N_{cell\,1}$ is the number of cells for the finest grid, relying on the availability of at least four data points (grids). Assuming that the CFD method is theoretically second-order accurate, four types of expansions are considered as,

$$\begin{aligned} \Phi_i - \Phi_0 &= \alpha {h_i}^p, \\ \Phi_i - \Phi_0 &= \alpha h_i, \\ \Phi_i - \Phi_0 &= \alpha {h_i}^2, \\ \Phi_i - \Phi_0 &= \alpha_1 h_i + \alpha_2 {h_i}^2, \end{aligned} \tag{7}$$

in which Φ is the quantity of interest, Φ_i is the solution of grid i, Φ_0 is the estimate of the exact solution, p is the observed order of grid convergence and α is a constant coefficient. Then, the best fit to the data for each of these expansions is obtained in the least-squares sense. Several alternative formulations are involved, including weighted and non-weighted fits of expressions. The selection of the best error estimate is based on the standard deviation of the fits. Thereafter, the error estimate is converted into an uncertainty with a safety factor that depends on the observed order of grid convergence and on the standard deviation of the fit. More information about the tool and the implemented methodology can be found in Eça and Hoekstra (2014).

4.6. Convergence criteria and post-processing techniques

It is necessary to attain proper convergence before post-processing the results of the computations. Convergence must be achieved not only within each time step but also statistically for a certain duration of time. The level of convergence can be assessed by monitoring the history of residual variations for the mass and momentum equations, (ITTC, 2014). Residuals indicate how far the present approximate solution deviates from the perfect conservation of mass and momentum, hence quantifying the imbalance between the left and the right-hand side of the discretized equations across all the computational cells.

For the simulations carried out in this paper, a proper level of convergence was achieved within each time step considering the conservative choice of the maximum number of inner iterations for each time step. The recommended criterion for assessing the convergence in the whole simulation time is the drop of normalized residuals by several orders of magnitude off their initial values, (ITTC, 2014). However, in the investigations of ship hydrodynamic performance in calm water and regular head waves, the residuals exhibit an oscillatory behavior during the solution time due to the complexity of the problem, hence such criterion may not be satisfied. Moreover, residuals do not necessarily relate to quantities of engineering interest in the simulation such as hydrodynamic forces and ship motions. Therefore, in this work, besides monitoring the residuals, the convergence is mainly assessed through the computed ship resistance. The criterion is defined differently for each operational point of the ship and is explained in the subsequent sections.

4.6.1. Convergence criterion for calm water simulations

In calm water simulations, the oscillatory behavior of the resistance and motions signals should ideally vanish and the solution should converge to a constant value for each quantity. However, due to the unsteady nature of the problem, this may never be achieved. Moreover, the convergence to a constant value not only requires an extremely long simulation time (high computational costs), but also beyond a certain point, it may not result in any significant changes in the magnitude of the final value. Therefore, a convergence criterion on the resistance signal is defined in order to obtain a reliable estimate of resistance and other quantities with reduced computational costs.

A calm water simulation is deemed converged when the Standard Deviation (STD) of the total resistance time history is below 2% of its Root Mean Square (RMS) for a defined time window of the signal tail. The choice of the time window is dependent on the signal oscillations. In Fig. 5, a representative plot is shown for a resistance signal sample in calm water simulations.

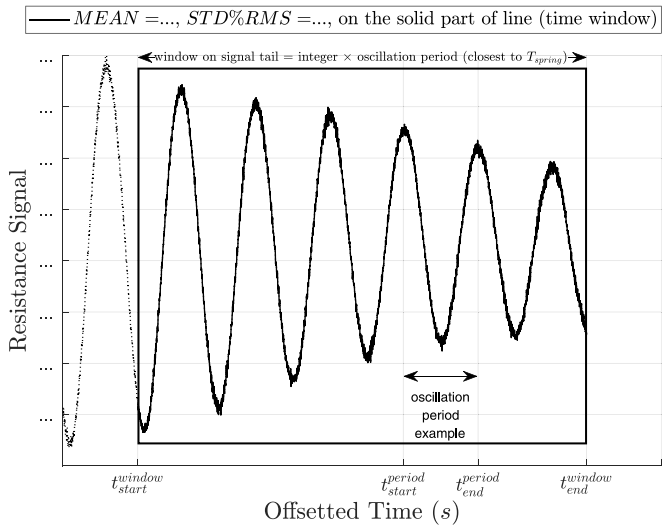

Fig. 5. A representative resistance signal plot for explaining the convergence criteria and post-processing techniques in calm water.

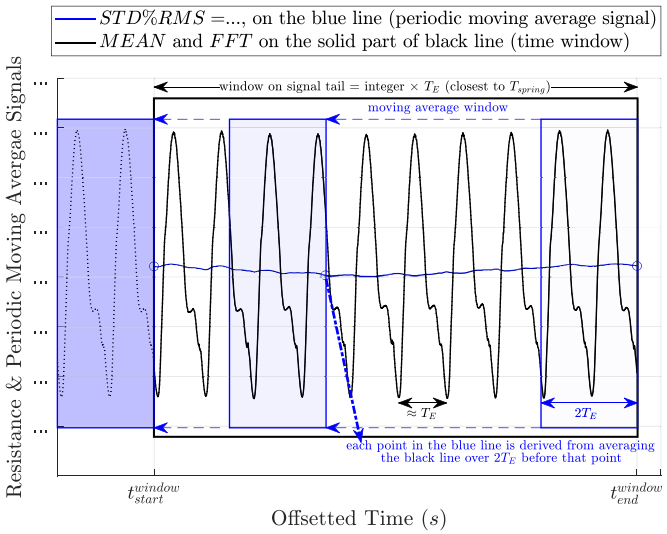

Fig. 6. A representative resistance signal together with its periodic moving average signal plot for explaining the convergence criteria and post-processing techniques in regular head waves.

The horizontal axis shows the offsetted time to visualize only the tail of the computed signal, i.e., the more important part, and eliminate the initial part. A time window is selected on the signal tail and shown with a black rectangle. The signal consists of a part highlighted by a dashed line starting at an arbitrary time instance and a solid line part beginning from the start time of the selected time window and extending to the end of the signal which is also the end of the selected time window. The mean value of the signal within the selected window (MEAN) as well as its Standard Deviation normalized by the percentage of Root Mean Square (STD%RMS) are shown in the plot legend. The simulation is deemed converged when the STD%RMS becomes smaller than 2. Then the MEAN value represents the calm water resistance.

As can be seen, the resistance signal exhibits an oscillatory behavior in time while the amplitude of oscillations decay. However, the oscillations are rather periodic in time. An example of such oscillation period is shown in Fig. 5. Therefore, a proper time window can be a multiplication of an integer number to the oscillation period. Then there is a lower uncertainty involved in the calculation of the MEAN value.

For calm water simulations in this paper, the oscillation period is approximately 2 s. On the other hand, the resistance signal in the free surge condition is affected by the spring. The natural period of the spring is $T_{spring} \approx 11.25$ s. Therefore, in order to partly include the effects of spring, a time window of $6 \times 2 = 12$ s is chosen which is rather close to one spring natural period.

4.6.2. Convergence criterion for regular wave simulations

In regular head waves simulations, the oscillatory behavior of the resistance and motions signals should ideally become periodic (harmonic) with respect to the wave encounter frequency with consistent harmonic amplitudes. However, due to the unsteady nature of the problem, as well as other contributing factors such as the change of actual incident wave and the presence of the spring, this may never be achieved. Therefore, a convergence criterion on the resistance signal is defined in order to estimate trustworthy outcomes from the computations in regular head waves.

The convergence criterion in regular head waves is defined on the "periodic moving average" of the resistance time series. However, the hydrodynamic analysis of the time series is carried out for the original signal. The periodic moving average is a signal derived from the original resistance signal, in which its value at each instance of time is the average of the resistance signal values over a moving average window before that instance of time. In Fig. 6 a representative plot is shown for a resistance signal sample and its periodic moving average signal in regular head waves simulations.

The horizontal axis shows the offsetted time to see only the tail of the computed signal and eliminate the initial part. The black line is the original resistance signal. A moving average window (blue rectangle) is selected in order to derive the periodic moving average signal (blue line). A proper choice of the moving average window can be a multiplication of an integer number to the wave encounter period T_E in each wave length. Based on the preliminary investigations and in order to keep the computational costs low, here, it is decided to define the moving average window as $2T_E$ for each respective wave length.

Thereafter, a time window is selected on the signal tail and shown with a black rectangle. The original signal consists of a dashed line part starting arbitrarily at some instances of time and a solid line part starting from the kick-off time of the selected time window and ending at the end of the signal which is also the end of the selected time window.

A regular head wave simulation is deemed converged when the Standard Deviation (STD) of the periodic moving average signal (blue line) for the defined moving average window (blue rectangle) is below 2% of its Root Mean Square (RMS) over a selected time window (black rectangle). In the plot legend, the Standard Deviation in terms of the percentage of Root Mean Square (STD%RMS) calculated on the periodic moving average signal (blue line) on the selected time window is shown. Based on the defined criterion, if the STD%RMS is smaller than 2, then the simulation is deemed converged. However, the post-processing of the results is then carried out for the selected time window on the original signal. In order to post-process the time series $\psi(t)$, Fourier analysis is performed as,

$$\psi(t) = \psi_0 + \psi_1 cos(\omega_E t + \psi_{\varepsilon 1}) + \psi_2 cos(2\omega_E t + \psi_{\varepsilon 2}) + \psi_3 cos(3\omega_E t + \psi_{\varepsilon 3}) + \cdots, \tag{8}$$

where ψ_i is the ith harmonic amplitude of the quantity under study ψ, and $\psi_{\varepsilon i}$ is the phase component related to the ith harmonic amplitude.

Although a good choice of the time window for the Fourier analysis shall include several spring natural periods, this is not feasible due to the extremely large required computational costs. Therefore, for each wave length, the time window is selected in a way to have an integer number of T_E which is closest to one spring natural period T_{spring} in

order to partially incorporate the spring effects. In the representative resistance plot shown in Fig. 6, the spring effect can be observed in the periodic moving average signal (blue line). The reason behind choosing an integer number of T_E is to minimize the spectral leakage in the Fast Fourier Transform (FFT) results. Those integer numbers are given in Section 6 for the waves under study in this paper.

4.6.3. Reconstruction of time series

The time series are reconstructed in order to generate reconstructed time series for 1 encountered wave period T_E in each wave length. The reconstruction is based on the Fourier series, Eq. (8), in which only the dominant harmonic components (HC), i.e., harmonic amplitudes (HA) and harmonic phases, derived from the FFT results over the chosen time window in each wave length, are taken into account. In order to make all the reconstructed time series compatible for EFD and CFD, the origin of time $t/T_E = 0$ in the reconstructed time series is defined as when the wave crest is located at the initial position of the ship fore perpendicular.

It should be noted that the CFD wake contour plots in regular head waves are only recorded for the last encountered wave in each simulation. Therefore, the reconstructed time series should be compared with the original time series during the last encountered wave in each simulation. However, the last encountered wave in each simulation does not necessarily start from the time when the incident wave crest is at the initial position of the ship fore perpendicular. Therefore, the origin of time ($t/T_E = 0$) for the last encountered wave time series in each simulation should be "synced" with the defined time origin for the reconstructed time series.

To achieve the synced time series for the last T_E, first, such last T_E time series are divided into two parts: part one from the beginning of the time series to the time in which the wave crest is at the initial position of the fore perpendicular, and part two from the time in which the wave crest is at the initial position of the fore perpendicular to the end of the signal. Then these parts are swapped, hence part two starts from a synced $t/T_E = 0$ and part one is simply attached to the end of part two. The attachment point mainly overlaps for most of the time series because the behavior of the ship is rather harmonized with the encountered wave period. However, this is not true for the surge motion time series in which, due to the presence of spring, the ship experiences an extra harmonic behavior at the spring's natural frequency. Therefore, the attachment point often does not overlap in the plots depicting the synced last T_E time series of surge motion.

4.6.4. Wake analysis methods

As discussed in Section 3, the SPIV measurements were carried out for carriage-fixed planes, however, it is more beneficial to study the ship nominal wake on the hull-fixed propeller disk. Therefore, although the wake validation is performed for the carriage-fixed planes similar to the SPIV measurements, the analysis of wake is carried out on the hull-fixed propeller disk.

The analysis of wake includes the investigations of three velocity components of the flow, i.e., axial u, transversal v and vertical w components on the propeller disk located at the propeller center and moving with the hull during the motions. Transversal and vertical components are the tangential velocity components to the propeller disk surface in Y and Z directions, respectively. The axial velocity is considered positive from the fore ship into the propeller disk, i.e., opposite of X direction, while the transversal and vertical components follow the hull fixed coordinate systems in Fig. 1. As shown in Fig. 7, the propeller disk radius is equal to the propeller radius. The velocity components are time-averaged ($\bar{u}$, $\bar{v}$, $\bar{w}$) and/or surface-averaged ($\tilde{u}$, $\tilde{v}$, $\tilde{w}$) in distinct ways in order to extract and present the main features of the flow.

Surface averaging of the wake is carried out in two ways: one over the whole propeller disk surface area and the other for a number of equally distanced (in the radial direction) circumferential surface areas. Such circumferential surface areas are derived from the division of the propeller disk (excluding the hub) into 10 circumferential stripes with the first strip starting at the hub edge to a radius of $R_{hub}+(R-R_{hub})/10$ with an assumed strip center at $r_1 = R_{hub}+(R-R_{hub})/20$, see Fig. 7. The same radial stepping is used to define the remaining 9 circumferential stripes where the outer edge of the tenth surface is the propeller tip radius R. The surface-averaged wake on these surface areas is called "circumferential-averaged wake", henceforth.

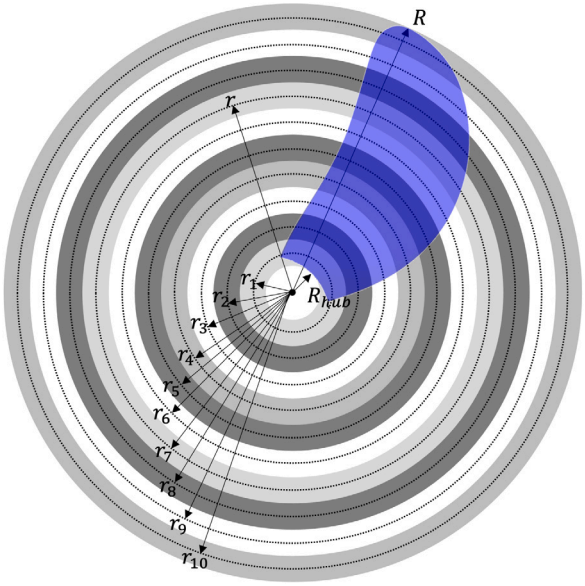

Fig. 7. Circumferential stripes defined on propeller disk for wake analysis.

On the other hand, time averaging of wake over a specific time period can be carried out in three ways: for each point on the propeller disk surface area (to be able to present it as a contour plot), for the circumferential-averaged wake at different radii (to be presented as a line plot), or for the surface-averaged wake ($\tilde{u}$, $\tilde{v}$ and $\tilde{w}$) over the whole propeller disk (to be able to derive one value as $\bar{\tilde{u}}$, $\bar{\tilde{v}}$ and $\bar{\tilde{w}}$). The time period for time-averaging wake in the regular wave simulations is mainly considered as an integer number times T_E in each wave length.

Finally, Fourier analysis of velocity components can be carried out for each extracted data point (computational cell) on the propeller plane to extract the harmonic amplitudes and phases at that specific point. The outcome can be plotted as contours of harmonic amplitudes and phases of velocity components at the propeller plane.

Although the wake of the ship in calm water simulations can be unsteady, only the last time step of each simulation is used for wake comparison. This was because the unsteady effects were deemed insignificant in comparison to that of highly dynamic regular head waves.

5. Calm water — V&V

In this section, the calm water results are provided including a verification and validation analysis of the ship resistance, motions and its wake. The calm water simulations are carried out in free surge conditions (3DOF) across all of the considered grids, i.e., $n = 0.75$, 1.00, 1.25, 1.50 and 2.00. First, the convergence of simulations is discussed and then, the verification and validation of results are carried out. The investigations are divided into two parts: one for resistance and motions studied in Section 5.1, and the other for wake studied in Section 5.2. Further analysis of the calm water simulation results with respect to the hydrodynamic performance of the ship is provided in Section 7.

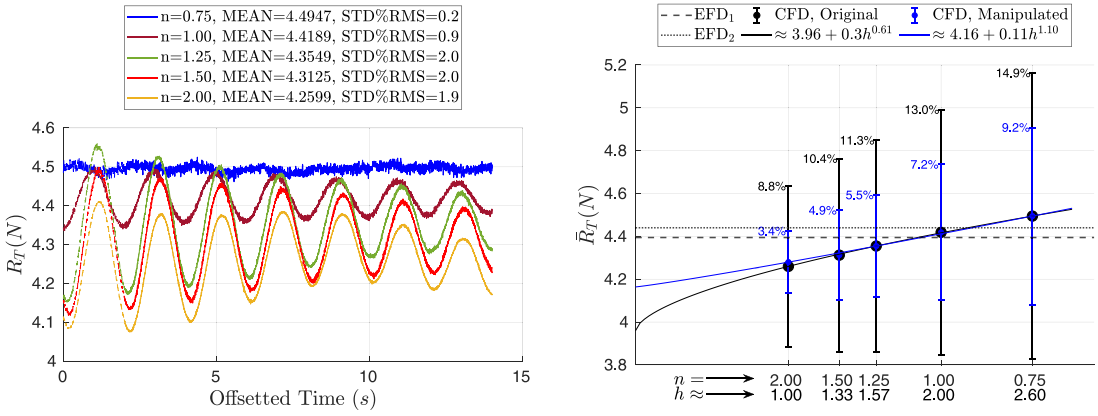

(a) Resistance time series. (b) V&V of resistance.

Fig. 8. Calm water resistance results.

Table 2
Comparison of EFD and CFD (only for $n = 1.00$) results in calm water.

Data	EFD_1	EFD_2	$n = 1.00$			
			$E = CFD - EFD$		$E\%D = E/EFD \times 100$	
			E_1	E_2	$E\%D_1$	$E\%D_2$
$\bar{R}_T$ (N)	4.394	4.440	0.024	−0.021	0.5	−0.5
$\bar{x}$ (m)	0.0124	0.0058	−0.0125	−0.0058	–	–
$\bar{z}$ (m)	−0.0032	−0.0027	0.0002	−0.0002	−6.8	9.4
$\bar{\theta}$ (deg)	0.129	0.088[a]	−0.014	0.027	−11.0	30.0

– No meaningful comparison can be performed as $\bar{x}$ depends on F_0.

[a] The authors of the current paper believe that the sign of pitch in EFD$_2$ was not consistent with the prescribed coordinate system in Mwangi (2021), therefore, the pitch sign is modified here. The same modification is also applied to the EFD$_2$ results in waves.

5.1. Resistance and motions in calm water

The calm water resistance results are shown in Fig. 8. There is a factor of 2 multiplied to the resistance results from the simulations with symmetry boundary conditions in order to represent the full hull results. Some marginal effects from the spring on the resistance time series can be observed in Fig. 8(a). The convergence criterion for calm water simulations is explained in Section 4.6. The selected time window for calm water simulations is 12 s. The convergence is confirmed in all grids and the presented MEAN values in the plot legend in Fig. 8(a) are the computed total resistance from each grid. Such values are used in Fig. 8(b) in order to perform the verification and validation study. Moreover, a quantified comparison between different results in calm water from EFD and CFD (only for grid $n = 1.00$) is shown in Table 2.

The computed resistance values in all grids are relatively similar which are also close to the EFD data, e.g., with a discrepancy of ±0.5% for grid $n = 1.00$, when compared with EFD$_1$ and EFD$_2$. On the other hand, the fitted line using the employed uncertainty analysis tool is very sensitive to small changes of magnitude. In order to illustrate such sensitivities, the resistance value for the finest grid $n = 2.00$ is manipulated (increased by 0.02 N) and a new line is fitted by the tool, shown in Fig. 8(b). The asymptotic resistance obtained from the grid convergence study on the original CFD data is predicted to be almost 4 N and the uncertainty of the finest grid is about 8.8%. However, the uncertainty of the finest grid for the manipulated CFD data is reduced to 3.4% with the final asymptotic value around 4.2 N and a relatively linear fitted line. This may encourage a linear line fitting for the situations in which the data points are relatively close in terms of magnitude with regard to the accuracy of the employed computational tool.

The computed surge in all grids (not shown) for the calm water simulations is very close to zero (−0.0008 to 0.0016 m). The fixed and free surge should not change the steady-state values in calm water, but the transient values. Therefore, the surge value depends mainly on the external force F_0 and the spring stiffness, hence it cannot be compared between CFD and EFD as it is shifted by an arbitrary external force F_0 in different conditions. Considering zero surge acceleration $\ddot{x} \approx 0$ in calm water, then the resistance can be estimated as $R_T \approx F_0 - Kx$. The external force from EFD data is not available, but since the surge motion is given in Table 2, then the experimental F_0 in EFD$_1$ and EFD$_2$ can be approximated as 5.6 and 5.0 N, respectively. In the simulations, the external force $F_0/2 = 2.206$ N is considered (division by 2 is for symmetry boundary condition).

The computed heave and pitch in calm water (sinkage and trim but at COG) are shown in Fig. 9. The same time window is considered as of resistance time window to calculate the MEAN values of heave and pitch motions in the plots legends. These values are rather similar considering the very small differences in terms of magnitude (up to ≈ 0.0003 m and 0.001 deg). Therefore, the grid convergence study is not carried out for heave and pitch motions. The largest discrepancies between EFD and CFD ($n = 1.00$) for the heave and pitch motions in calm water are 9.4% and 30.0%, respectively. However, the errors in terms of magnitude are almost 0.0002 m and 0.027 deg which are negligible considering the accuracy of computations and measurements. Moreover, $\bar{z}$ and $\bar{\theta}$ values from CFD lie between the two EFD data sets, which may reveal the possible uncertainties in the experimental measurements.

The wall y^+ in each grid at the last time step in calm water simulations are shown in Fig. 10. The surface-averaged $\bar{y}^+$ values on the wetted surface area of the hull are approximately 134, 99, 78, 65 and 48 for the coarsest grid to the finest one. The hull wetted surface area is about 2.78 m^2 in all grids.

The bilge vortex found by the same Q-criterion in different grids is shown in Fig. 11. A smaller vortex is also generated under the hub cap region that swirls opposite to the bilge vortices, as shown by the normalized helicity. The vortical structures are obviously captured with a higher resolution in finer grids. The position where the vortices hit the propeller disk is found to be more or less stationary during the ship performance in calm water.

5.2. Wake in calm water

The time series of the axial velocity component of the surface-averaged nominal wake computed on the hull-fixed propeller disk $\tilde{u}$ for different grids as well as the grid convergence study performed on the MEAN values $\bar{\tilde{u}}$ (time-averaged over the selected 12 s time window)

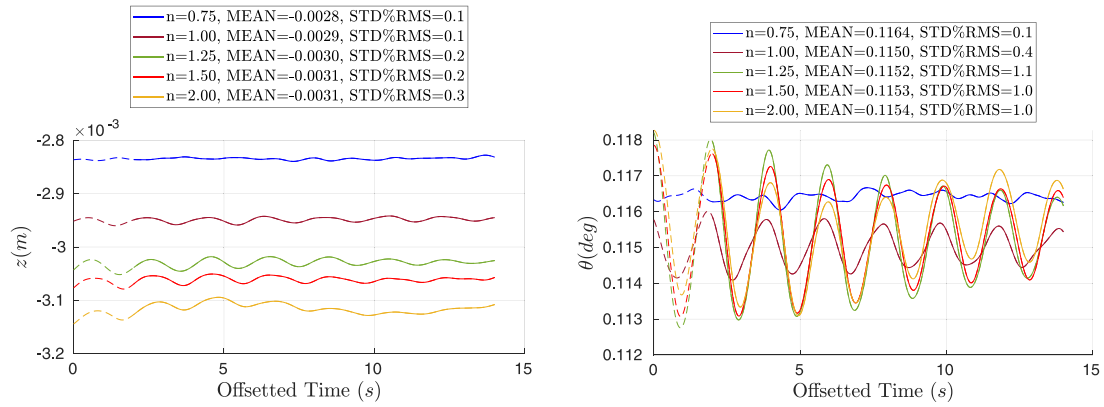

(a) Heave time series. (b) Pitch time series.

Fig. 9. Computed heave and pitch in calm water simulations.

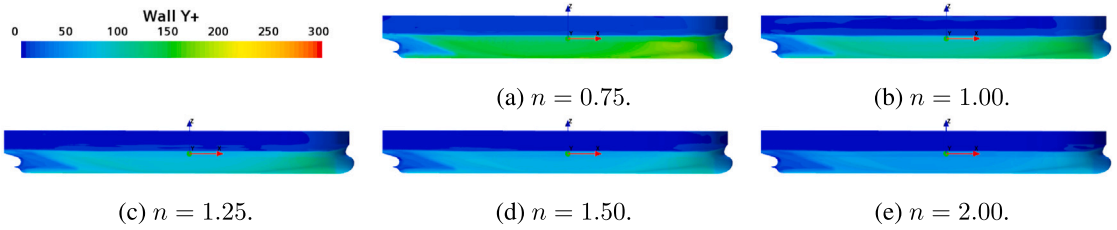

(a) $n = 0.75$. (b) $n = 1.00$.

(c) $n = 1.25$. (d) $n = 1.50$. (e) $n = 2.00$.

Fig. 10. Wall y^+ in each grid at the last time step in calm water simulations.

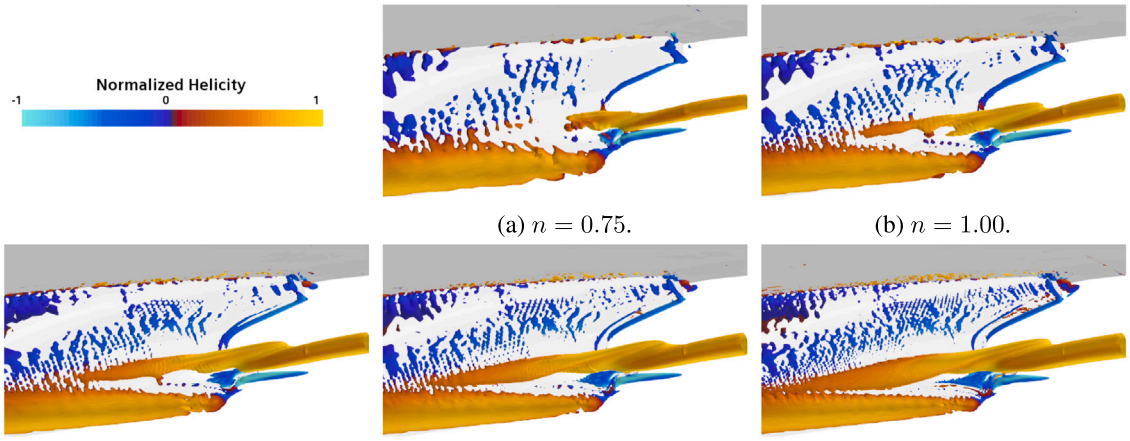

(a) $n = 0.75$. (b) $n = 1.00$.

(c) $n = 1.25$. (d) $n = 1.50$. (e) $n = 2.00$.

Fig. 11. The vortical structures (colored by normalized helicity) found by Q-criterion = 10 /s^2 in each grid at the last time step in calm water simulations.

are shown in Fig. 12 for calm water simulations. The time series of the transversal and vertical velocity components for different grids are also given in Fig. A.1 in Appendix, but not studied further in this paper.

The MEAN values of the axial velocity component in Fig. 12(a) are used to perform a verification study in Fig. 12(b), in which a monotonic convergence is seen. The numerical uncertainty of the axial wake varies between 31% and 18% from the coarsest to the finest grid, and $\tilde{\bar{u}}$ reduces approximately 12%. This indicates the significance of grid refinement level on the predicted wake in calm water simulations. The MEAN value of the axial velocity of the wake decreases as the refinement level increases. This is likely attributed to the improved prediction of the bilge vortex and its interaction with the boundary layer as the grids become finer. It is widely recognized that a bilge vortex causes the boundary layer to open up, forming a distinctive "hook shape" in the wake. With finer grids, the bilge vortex is captured more accurately, allowing for a more precise representation of its effect in opening up the wake. Consequently, this leads to a reduced wake at the propeller plane as seen in Fig. 11.

The SPIV measurements and hence the wake validations are carried out in the carriage-fixed planes. In Figs. 13 and 14, the wake at propeller plane and aft perpendicular can be compared between EFD and CFD. The plot axes Y/L and Z/L are defined in the corresponding carriage-fixed coordinate systems (CF_{PP} and CF_{AP}). The non-dimensional axial velocity u/U is represented by contour plots and the non-dimensional transversal and vertical velocity components (tangential to the plane of study) are represented by vectors. Due to the existence of different potential sources of discrepancy, the comparison of EFD and CFD wake can only be carried out qualitatively.

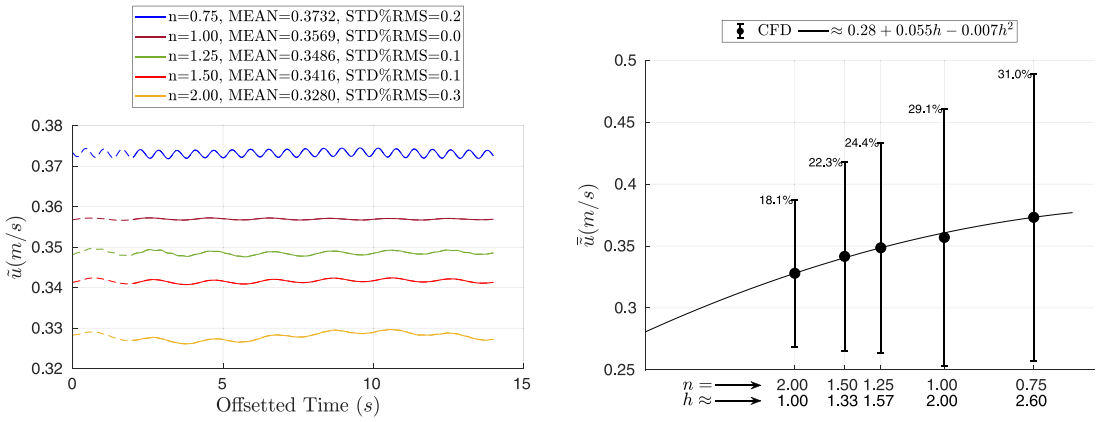

(a) Axial component time series. (b) Verification of axial component.

Fig. 12. Time series and verification of the surface-averaged wake axial velocity component over the hull-fixed propeller disk in calm water simulations.

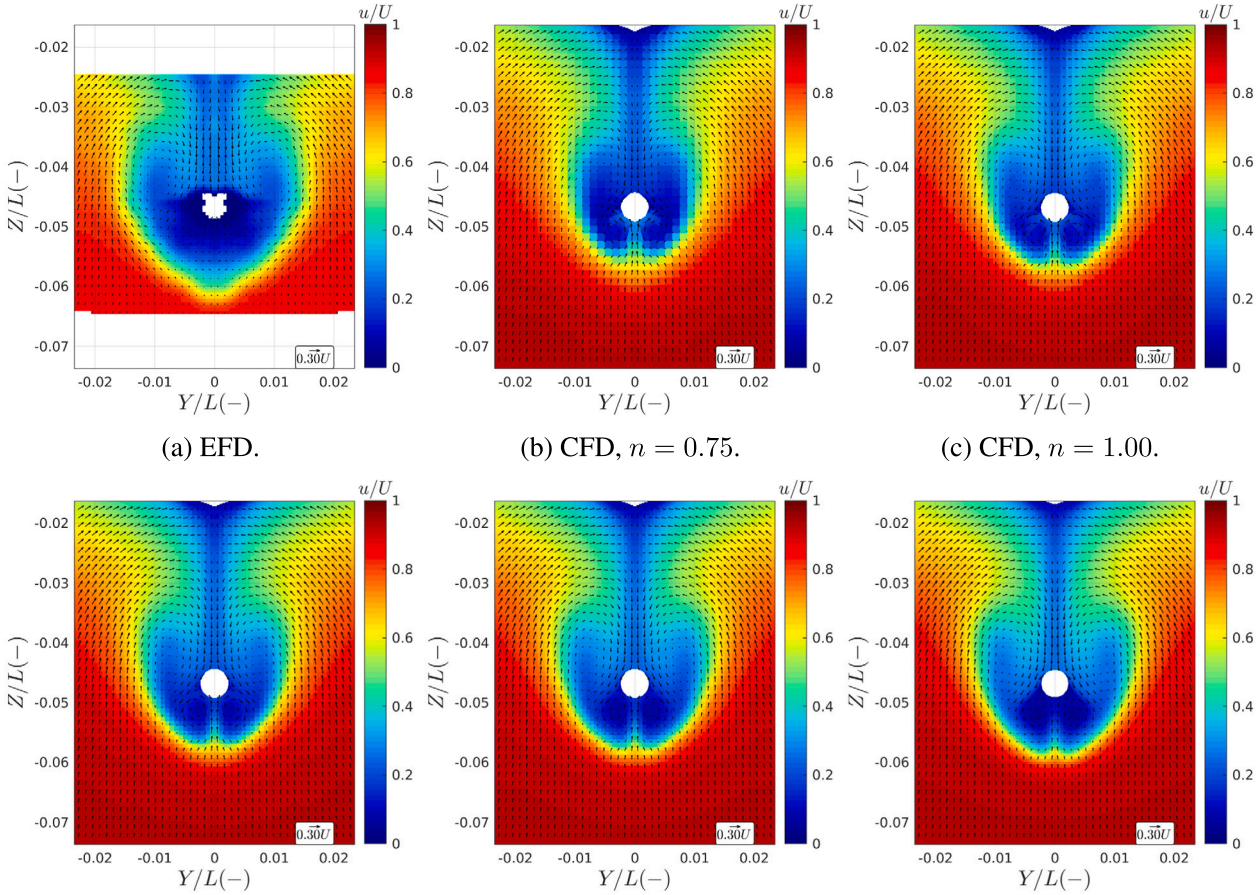

(a) EFD. (b) CFD, $n = 0.75$. (c) CFD, $n = 1.00$.

(d) CFD, $n = 1.25$. (e) CFD, $n = 1.50$. (f) CFD, $n = 2.00$.

Fig. 13. Calm water EFD wake (SPIV) and CFD wake (at the last time step of simulation) in carriage-fixed plane at the initial position of propeller plane (CF_{PP}).

Unfortunately, the SPIV measurement data is not accessible for calm water in EFD_1 in 3DOF. However, another measurement is available from the OU test campaign for KVLCC2 in calm water in which the model was fixed but with predefined sinkage and trim setup, provided in Win et al. (2016) and shown in Fig. 13(a). Since the heave and pitch motions in calm water are very small, insignificant effects are expected.

The SPIV measurements of EFD_2 in calm water were carried out at aft perpendicular in fixed surge condition (2DOF) and it is shown in Fig. 14(a). It is worth mentioning that the calm water simulations with fixed surge are also carried out but the differences in the computed wakes were negligible between free and fixed surge simulations. Therefore, the results of fixed surge simulations are excluded from this paper.

The main flow features are comparable between EFD and CFD wake in Figs. 13 and 14. The coarser grids are less capable of capturing the main wake features, hence the flow details and the hook shape

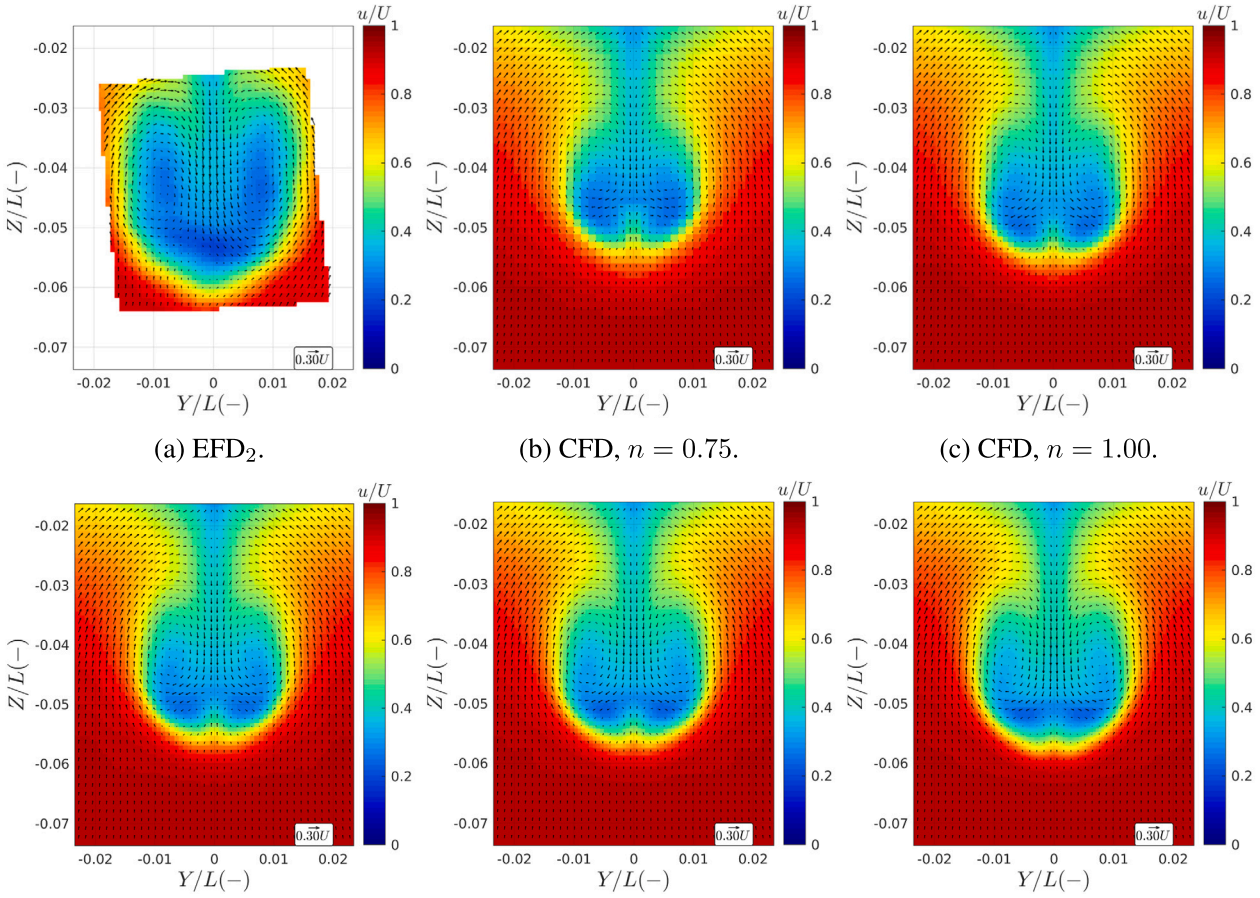

(a) EFD_2. (b) CFD, $n = 0.75$. (c) CFD, $n = 1.00$.

(d) CFD, $n = 1.25$. (e) CFD, $n = 1.50$. (f) CFD, $n = 2.00$.

Fig. 14. Calm water EFD_2 wake (SPIV) and CFD wake (at the last time step of simulation) in carriage-fixed plane at the initial position of aft perpendicular (CF_{AP}).

bilge vortex are captured much better in the finer grids. Nevertheless, the details of the hook shape bilge vortex seen in EFD_2 wake are mostly missing in CFD computations in all grids. Such details are only represented to some extent in the finer grids.

One obvious difference between the EFD and CFD wake is the computed velocity components under the hub in all grids. It is clear that the symmetry boundary condition defined in the CFD simulations forced the normal flow velocities across the symmetry plane to zero. However, this is not the case in model tests as the flow can commute to different sides due to the asymmetric nature of the problem. It is worth mentioning that a simulation in a full domain (without the symmetry boundary condition) is also carried out for the grid $n = 1.00$, however, no significant changes are seen in the CFD wake. The authors' speculation is that the difference may be originated from any asymmetry conditions in the model tests, e.g., the manufactured model or within the experimental setup which are inevitable in model tests. However, in a general qualitative sense, the EFD and CFD wake are comparable.

The nominal wake on the propeller disk obtained from different grids at the last time step of the simulations is shown in Fig. 15. Since the surge, heave and pitch motions in free surge calm water simulations are very small, the wake on the hull-fixed propeller disk is very similar to that of the carriage-fixed wake at the initial position of the propeller plane in Fig. 13. The captured bilge vortex is stronger in the finer grids and the extent of the vortical structures under the hub and particularly the size of the low axial velocity region are larger for the finer grids.

Propeller designers often use a circumferential-averaged wake for designing the particulars of a wake-adapted propeller. Such wake represents an averaged flow encountered by the propeller blade at each radius in one revolution. Fig. 15(f) shows the computed circumferential-averaged axial component of the CFD wake obtained from different grids. A rather significant difference in the magnitude and profile of the wake components is observed between various grids, e.g., in $r/R \approx 0.6$–0.8, where the large part of the propeller thrust is often generated. A reduction of approximately 29% is seen in $r/R \approx 0.7$ from the coarsest grid to the finest one, whereas a relatively smaller difference (≈12%) is seen for the surface-averaged wake over the whole propeller disk $\bar{\bar{u}}$ in Fig. 12. In case a propeller is supposed to be designed based on a CFD wake, the resultant wake-adapted design will be very different depending on the employed wake. The circumferential-averaged wake for the non-axial velocity components is also shown in Fig. A.2 in Appendix, but not further analyzed in this paper.

6. Regular wave — V&V

In this section, the regular head wave results are provided including a convergence assessment as well as an extensive verification and validation analysis of the ship resistance, motions and its wake. The CFD simulations in regular head waves are carried out across all of the considered grids, i.e., $n = 0.75$, 1.00, 1.25, 1.50 and 2.00, in wave lengths $\lambda/L = 0.6$ and 1.1, however, only the grid $n = 1.00$ is considered for the hull performance simulations in the longest wave $\lambda/L = 1.6$. Therefore, the grid convergence study is only carried out for $\lambda/L = 0.6$ and 1.1. The verification and validation of results are carried out in two

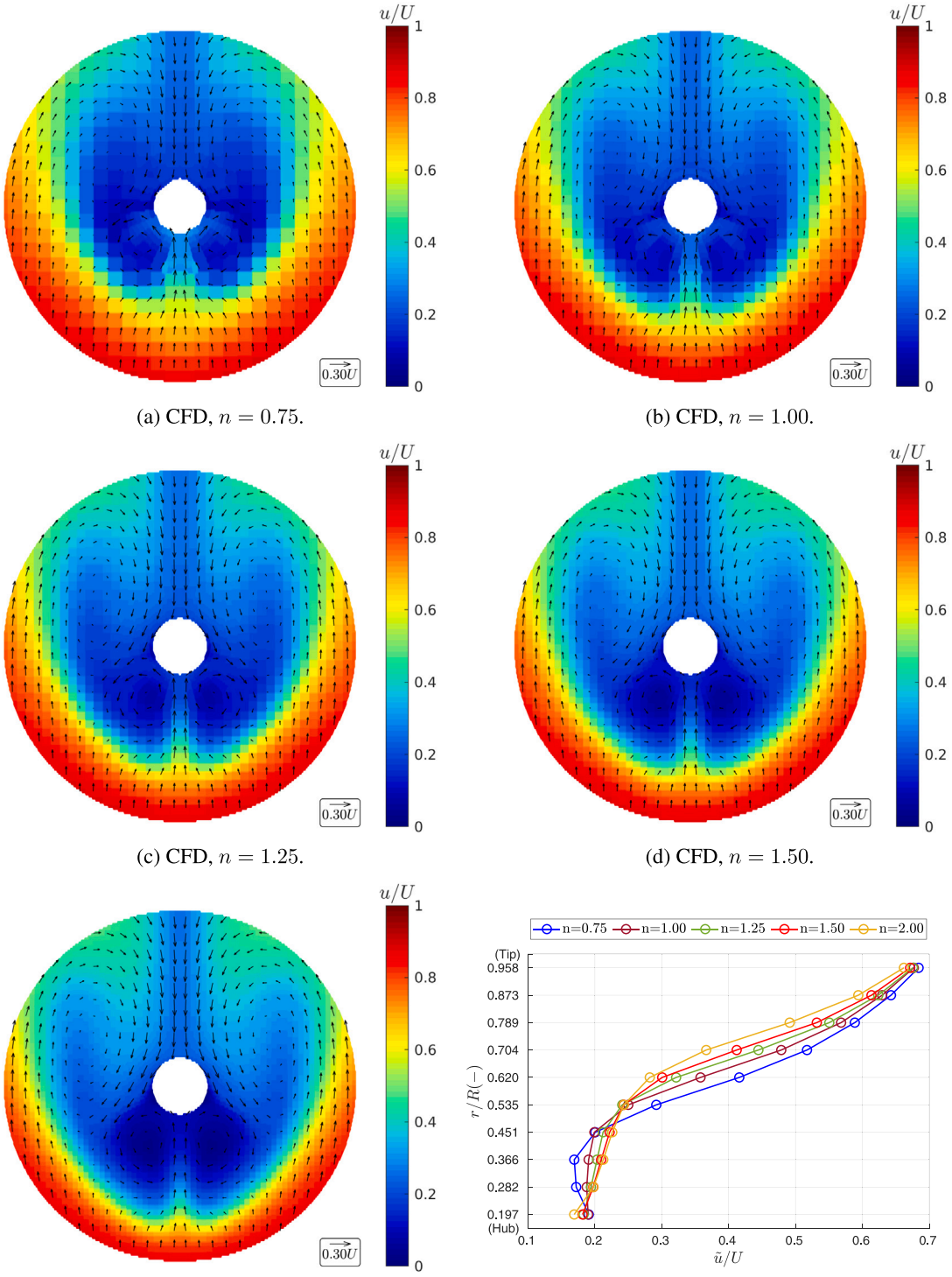

(a) CFD, $n = 0.75$. (b) CFD, $n = 1.00$.

(c) CFD, $n = 1.25$. (d) CFD, $n = 1.50$.

(e) CFD, $n = 2.00$. (f) Circumferential-averaged axial component.

Fig. 15. CFD wake and circumferential-averaged axial velocity component on hull-fixed propeller disk at the last time step in free surge calm water simulations.

parts: one related to the resistance and motions in Section 6.1 and the other related to the wake in Section 6.2. Further analysis of the regular head wave results with respect to the hydrodynamic performance of the ship is provided in Section 7.

As it is discussed in Section 4, the quality of actual incident waves plays a critical role in the hydrodynamic performance of the ship operating in regular waves. Based on the preliminary investigations in Irannezhad (2022), insignificant deviations are expected for the numerical waves compared to the analytical one in the current paper. However, the deviations may become notable between the actual incident waves in the current model tests and the intended waves, mainly due to the performance of the wave generator and wave dampener systems in the towing tank. Such deviations may be counted as an important source of discrepancy in the validation of the results.

6.1. Resistance and motions in regular waves

The convergence of the simulations in regular head waves, explained in Section 4.6, is investigated in Fig. 16. The selected time windows for $\lambda/L = 0.6$, 1.1 and 1.6 are $15T_E = 11.39$ s, $10T_E = 11.20$ s and $8T_E = 11.30$ s, respectively. The wave encounter period T_E is different in each wave length λ/L and the time window in each wave length is chosen in order to be close to one spring natural period $T_{spring} \approx 11.25$ s.

The moving average is calculated on a $2T_E$ moving window in each λ/L. The derived STD%RMS values on the periodic moving average time series of resistance for all grids in $\lambda/L = 0.6$ and 1.1 confirms the convergence based on the defined criterion. However, the convergence criterion is not satisfied in $\lambda/L = 1.6$ as STD%RMS > 2, even after running the simulation for a long physical time. This may reflect that the defined convergence criterion is too conservative for this wave length as there are noticeable effects from spring on the moving average of resistance in Fig. 16(f). The MEAN values and the Fourier analysis of different time series are all calculated on the selected time windows in each wave length.

The FFT results of resistance in regular head waves are shown in Fig. 17. It is hard to compare the results for different grids in $\lambda/L = 0.6$ and 1.1, due to the major overlaps between different bars in the graphs. The main reason for providing the bar plots is to demonstrate the performance of the applied Fourier analysis with regard to the chosen time windows. The dominating bars are mostly seen at the integer values of the harmonic components ω/ω_E (the ratio of FFT frequencies to the wave encounter frequency). Therefore, the resistance time series are, to a high extent, a harmonic function of the wave encounter frequency, hence a rather minimized spectral leakage is obtained.

The calculated 0th, 1st, 2nd and 3rd harmonic amplitudes (HAs) of resistance, i.e., the FFT amplitudes in the respective harmonic components (ω/ω_E), are shown in the plots legends in Fig. 17. The 0th harmonic amplitudes of resistance are identical to the absolute of MEAN values ($\bar{R}_T$) given in the legends of Figs. 16(a), 16(c) and 16(e). The 0th, 1st and 2nd harmonic amplitudes are the dominant components in all wave lengths and higher harmonic amplitudes are very small, except for $\lambda/L = 1.1$ in which the higher harmonics (up to and including the 5th harmonic amplitude) are not negligible, but still relatively small.

In Irannezhad et al. (2022), the variation of dominant harmonic amplitudes of resistance in different wave lengths is studied for a general cargo vessel. It was shown that the higher harmonic amplitudes of resistance become noticeable in comparison to the 1st harmonic amplitude mainly in the vicinity of $\lambda/L = 1.0$, hence significantly affecting the mean total resistance near such wave length. Similar behavior is also observed in the current investigations for KVLCC2 in $\lambda/L = 1.1$. For instance, R_{T2}/R_{T1} ratio is rather large in $\lambda/L = 1.1$ compared to that of other two wave lengths. This will be discussed further in Section 7.

The verification of the dominant harmonic amplitudes of resistance, i.e., $\bar{R}_T$, R_{T1} and R_{T2}, is shown in Fig. 18. The vertical axis in some plots, e.g., in Fig. 18(b), is broken down and modified (scaled) in order to fit the results of all wave lengths in a single plot without losing important features and characteristics due to the large differences in magnitudes. Moreover, the quantified comparison between the EFD and CFD (only for grid $n = 1.00$) for the mean total resistance in dimensional $\bar{R}_T$ and non-dimensional $C_T = \bar{R}_T/(\rho g B^2 A^2/L)$ forms is shown in Table 3. The analytical wave amplitude of $A = 0.03$ m in CFD and the measured actual wave amplitude in each particular model test in EFD are used to non-dimensionalize the results.

The predicted asymptotic value for $\bar{R}_T$, shown in Fig. 18(a), is smaller than the computed values in both $\lambda/L = 0.6$ and 1.1, while the CFD results for different grids are similar in each wave length. Consequently, the calculated numerical uncertainties are rather large (6.6%−−11.1%). The numerical uncertainties for the 1st and 2nd harmonic amplitudes of resistance are lower than the ones seen for $\bar{R}_T$, except for R_{T2} in $\lambda/L = 1.1$ where such 2nd harmonic amplitudes are considerable.

On the one hand, the multiplication constant for the first-order term in both fitted lines in $\bar{R}_T$ is relatively larger than the second-order term, and since the CFD results are very similar in different grids, a linear line may be a better candidate for curve fitting. This is similar to what is seen in the calm water resistance grid convergence study. On the other hand, the predicted asymptotic value is very close to both EFD data in $\lambda/L = 1.1$, but very different in $\lambda/L = 0.6$. Therefore, a linear curve fitting would adversely alter this scenario for $\lambda/L = 1.1$, while improving it for $\lambda/L = 0.6$.

For the grid $n = 1.00$ in Table 3, the largest discrepancies for $\bar{R}_T$ are seen for $\lambda/L = 1.1$, i.e., over prediction by 7.7% and 9.9% in EFD_1 and EFD_2, respectively. However, the uncertainty of the experimental measurements should not be forgotten. The scatter of the experimental data in the repeated model tests for the data set EFD_1 is provided in Table 5. A different number of tests were carried out in each wave length. The scatter is illustrated as the Standard Deviation in terms of the percentage of the Root Mean Square ($STD\%RMS$) in different tests. The largest variations of $\bar{R}_T$ in the scatter of EFD_1 data (i.e., 19.3%) is seen in $\lambda/L = 1.1$, which may justify the largest validation errors seen in this wave length in Table 3.

The approximate linear relation of the added wave resistance to the wave amplitude squared has been discussed thoroughly in literature, for instance by Gerritsma and Beukelman (1972) and Block (1993). In the current study, in order to take into account the effects of actual measured wave height in the model tests, the total resistance coefficient $C_T = \bar{R}_T/(\rho g B^2 A^2/L)$ is calculated and shown in Table 3, in which the wave amplitude squared A^2 is utilized for the non-dimensionalization. It can be seen that the absolute of $E\%D$ for C_T is mainly reduced in comparison to $\bar{R}_T$ in $\lambda/L = 1.1$ and 1.6 (although it is slightly increased in $E\%D_2$ for $\lambda/L = 1.6$), however, it is substantially increased in $\lambda/L = 0.6$.

In the investigations in Irannezhad et al. (2022) for a general cargo vessel, it was shown that although the global trend of the added wave resistance was linearly proportional to the wave amplitude squared, nonlinear trends were seen in short waves and the wave lengths close to the heave and pitch natural frequencies. Such nonlinear behavior is also reported for KVLCC2 by different authors, e.g., Yu et al. (2017), Lee et al. (2017, 2019) and Seo et al. (2020). Consequently, the non-dimensionalization of total resistance by the wave amplitude squared may not be a legitimate choice for $\lambda/L = 0.6$, given that in this wave length the resistance errors are already insignificant in dimensional form, i.e., $E \approx 0.07$ N and $E\%D \approx 1.0$.

Since the 1st harmonic amplitude is the dominating component in the Fourier analysis of motion time series, there is no significant gain in providing the motions time series or their FFT bar graphs. On the other hand, the surge motion of the ship in regular head waves consists an amplitude at the frequency equal to the spring natural frequency (x_{1_s}) in conjunction with the amplitude at the wave encounter frequency (x_1). Therefore, the surge motion time series are provided in Fig. 19 which will be helpful to understand the instantaneous location of the carriage-fixed planes at the time of wake computations.

The MEAN values of surge motion shown in the plots legends are calculated on the same time window that used for the resistance time series. The same is also carried out for the heave and pitch time series and the CFD results (only for grid $n = 1.00$) of the MEAN values together with x_{1_s} are compared to those of EFD data in Table 4.

It should be noticed that $\bar{x}$ cannot be compared between EFD and CFD as it is influenced by the arbitrary choice of F_0 in different conditions. The applied F_0 in CFD simulations are 7.11 N, 10.40 N and 6.00 N in $\lambda/L = 0.6$, 1.1 and 1.6, respectively. Although the considered F_0 resulted in a very small $\bar{x}$ in CFD, the MEAN value of surge in the EFD data, especially in EFD_1, indicates a notable difference in

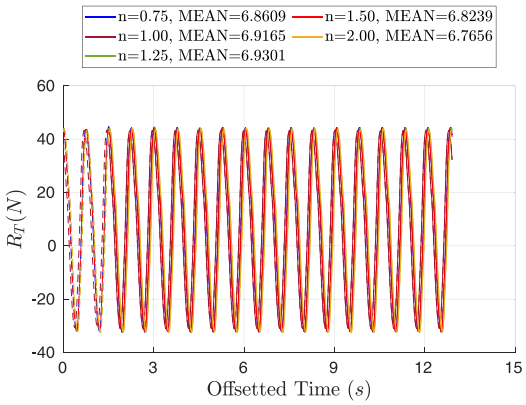

(a) Resistance time series in $\lambda/L = 0.6$.

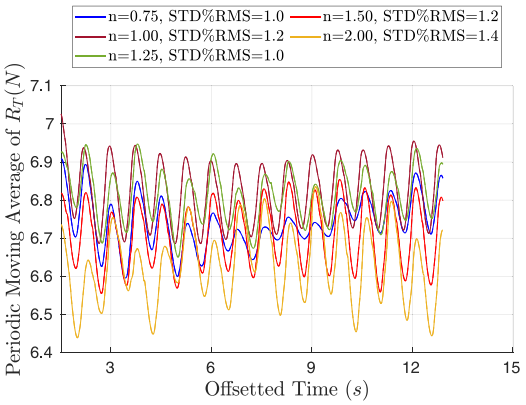

(b) Resistance periodic moving average in $\lambda/L = 0.6$.

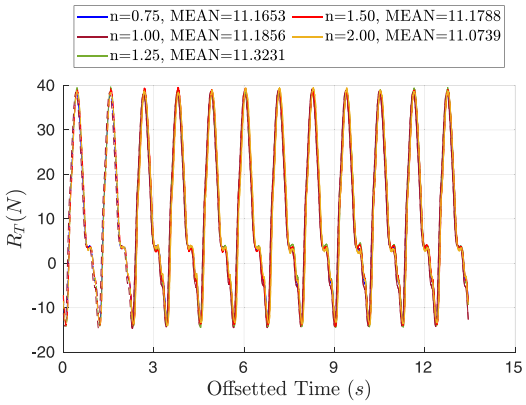

(c) Resistance time series in $\lambda/L = 1.1$.

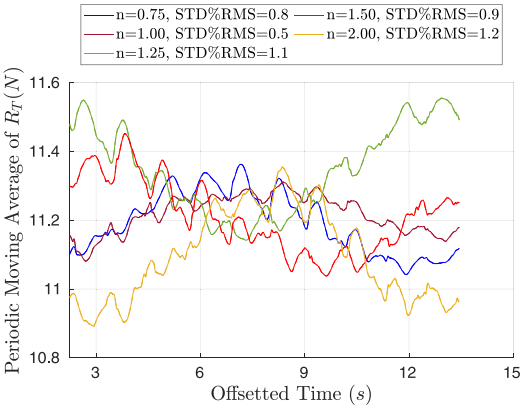

(d) Resistance periodic moving average in $\lambda/L = 1.1$.

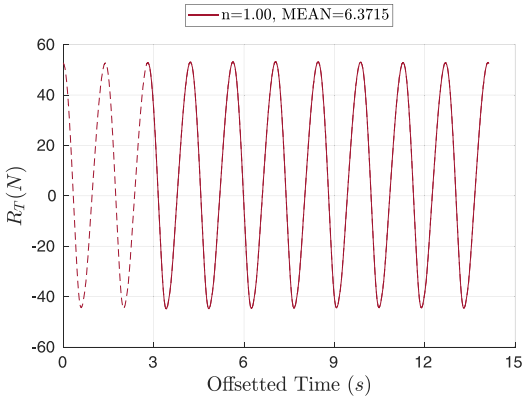

(e) Resistance time series in $\lambda/L = 1.6$.

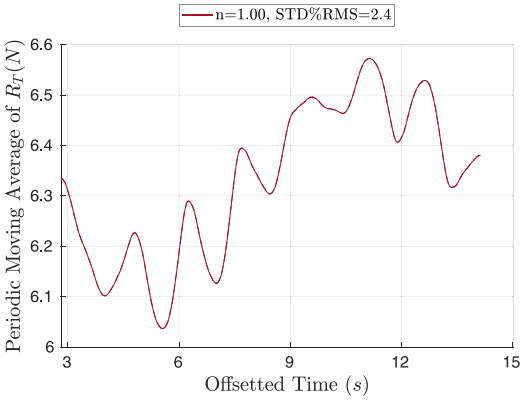

(f) Resistance periodic moving average in $\lambda/L = 1.6$.

Fig. 16. Resistance time series and its periodic moving average (on the respective $2T_E$ moving window in each λ/L) in regular head waves.

the considered F_0 in the corresponding model tests. Consequently, the mean stretch/compression of the spring is different between CFD and EFD data. Therefore, the carriage-fixed plane positions with respect to the hull are different which may be counted as a potential source of discrepancy for wake comparison in the carriage-fixed planes.

Although large values are seen for $E\%D_1$ of x_{1_s}, the difference between EFD_1 and CFD (E_1) is insignificant in terms of magnitude in all wave lengths. This statement is also valid for the mean values of heave and pitch ($\bar{z}$ and $\bar{\theta}$) when the results of grid $n = 1.00$ in CFD are compared to both EFD data in Table 4. The largest discrepancy in $\bar{z}$ is 0.0010 m which corresponds to 44.6% error. The mean value of pitch $\bar{\theta}$ from CFD corresponds well to the EFD_1 data with the largest discrepancies of 0.072 deg. But much larger disagreements are seen when it is compared to EFD_2 data. Such large differences between the two EFD data sets can also reveal the possible uncertainties in experimental data. In Table 5, large scatters are also observed for $\bar{z}$ and $\bar{\theta}$ for the repeated tests in EFD_1.

The verification and validation of the 1st harmonic amplitudes of motions are shown in Fig. 20. Moreover, the quantified comparison between EFD and CFD (only for grid $n = 1.00$) in dimensional (x_1, z_1 and θ_1) and non-dimensional (x_1/A, z_1/A and θ_1/kA) forms is shown in Table 3.

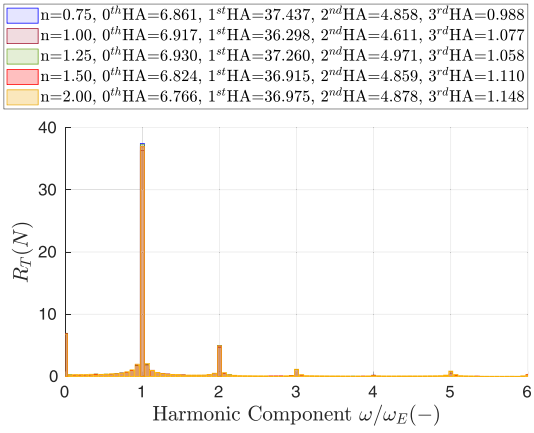

(a) FFT results in $\lambda/L = 0.6$.

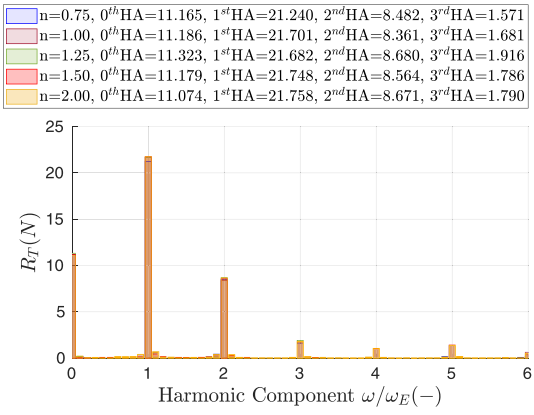

(b) FFT results in $\lambda/L = 1.1$.

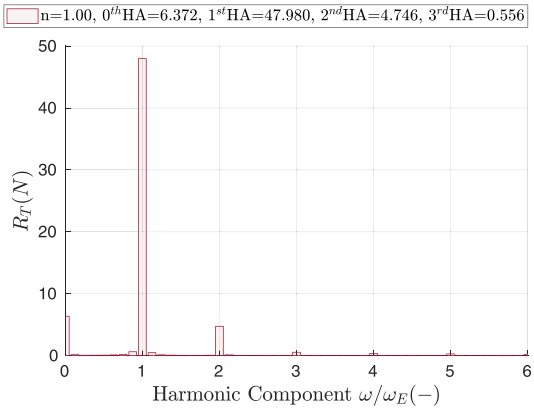

(c) FFT results in $\lambda/L = 1.6$.

Fig. 17. Fourier analysis results of the resistance time series in regular head waves simulations.

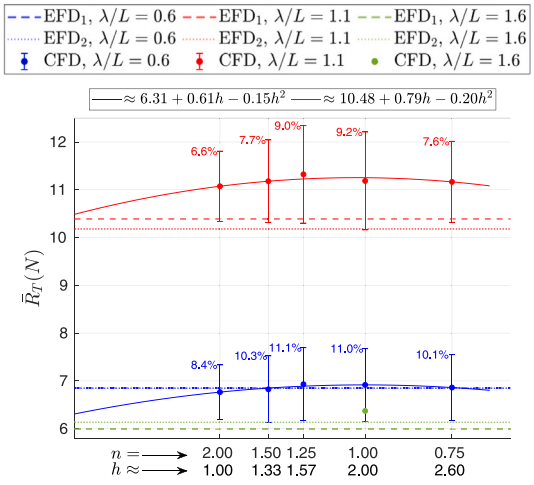

(a) 0th harmonic amplitude.

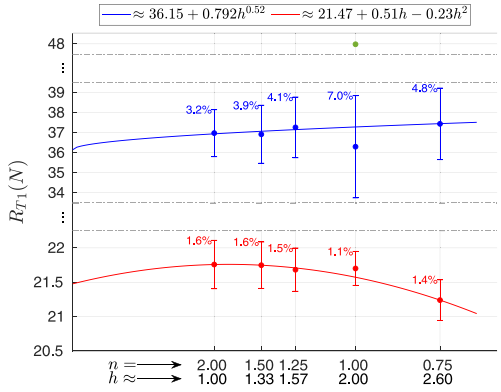

(b) 1st harmonic amplitude.

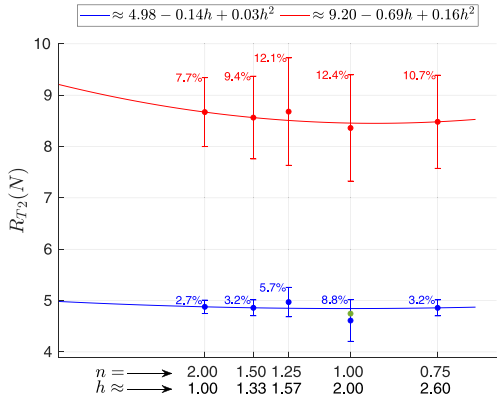

(c) 2nd harmonic amplitude.

Fig. 18. Verification and validation of the dominant harmonic amplitudes of resistance in regular head waves.

Despite the marginal magnitude of the 1st harmonic amplitude of motions in some conditions, the majority of the numerical uncertainties are relatively lower than the ones calculated for the mean value of total resistance in Fig. 18(a). Given that the 1st harmonic amplitudes of motions are very similar between different grids in each wave length, and the multiplication constants for the second-order terms are rather small in the fitted lines, a linear line might be a better candidate for curve fitting.

Although large errors are seen for all three motions in terms of percentage in Table 3, the discrepancies in terms of magnitude (E) are quite insignificant. Moreover, the computed $E\%D$ in the majority of results in $\lambda/L = 1.1$ and 1.6 is reduced for the non-dimensional quantities in comparison to the dimensional ones, indicating the importance of the actual measured wave height in the model tests. However, for the shortest wave $\lambda/L = 0.6$ these errors are mainly increased. In this wave length, the higher harmonic amplitudes are not completely negligible and non-dimensionalization using the wave amplitude may

Table 3
Comparison of EFD and CFD ($n = 1.00$) results in regular head waves for the dimensional and non-dimensional mean value of total resistance and the first harmonic amplitudes of motions. While the target wave amplitude of $A = 0.03\ m$ is used to non-dimensionalize the CFD results, the measured wave amplitude in each particular test is used for EFD data.

λ/L	Data	EFD_1	EFD_2	$n = 1.00$			
				$E = CFD - EFD$		$E\%D = E/EFD \times 100$	
				E_1	E_2	$E\%D_1$	$E\%D_2$
0.6	$\bar{R}_T$ (N)	6.852	6.847	0.065	0.069	0.9	1.0
	x_1 (m)	0.0017	0.0017	0.0000	−0.0001	0.6	−5.2
	z_1 (m)	0.0018	0.0019	−0.0000	−0.0001	−0.4	−7.0
	θ_1 (deg)	0.099	0.103	0.028	0.024	28.5	22.9
	$\overline{\lvert E\%D \rvert}$					7.6	9.0
	C_T (–)	8.004	9.281	−0.538	−1.815	−6.7	−19.5
	x_1/A (–)	0.0579	0.0661	−0.0019	−0.0102	−3.3	−15.4
	z_1/A (–)	0.0629	0.0726	−0.0027	−0.0124	−4.2	−17.0
	θ_1/kA (–)	0.018	0.020	0.004	0.002	23.5	9.7
	$\overline{\lvert E\%D \rvert}$					9.4	15.4
1.1	$\bar{R}_T$ (N)	10.390	10.180	0.796	1.006	7.7	9.9
	x_1 (m)	0.0022	0.0026	0.0000	−0.0004	1.0	−14.4
	z_1 (m)	0.0199	0.0198	0.0018	0.0019	9.1	9.4
	θ_1 (deg)	1.523	1.497	0.268	0.294	17.6	19.6
	$\overline{\lvert E\%D \rvert}$					8.9	13.3
	C_T (–)	11.804	11.392	0.270	0.683	2.3	6.0
	x_1/A (–)	0.0744	0.0871	−0.0011	−0.0138	−1.5	−15.9
	z_1/A (–)	0.6791	0.6722	0.0433	0.0502	6.4	7.5
	θ_1/kA (–)	0.509	0.497	0.075	0.087	14.6	17.5
	$\overline{\lvert E\%D \rvert}$					6.2	11.7
1.6	$\bar{R}_T$ (N)	5.989	6.133	0.382	0.239	6.4	3.9
	x_1 (m)	0.0073	0.0073	0.0006	0.0005	7.8	7.0
	z_1 (m)	0.0263	0.0260	0.0015	0.0018	5.7	7.1
	θ_1 (deg)	1.799	1.747	0.329	0.381	18.3	21.8
	$\overline{\lvert E\%D \rvert}$					9.5	9.9
	C_T (–)	6.963	7.292	−0.085	−0.414	−1.2	−5.7
	x_1/A (–)	0.2519	0.2566	0.0097	0.0050	3.8	1.9
	z_1/A (–)	0.9109	0.9094	0.0170	0.0185	1.9	2.0
	θ_1/kA (–)	0.885	0.869	0.124	0.140	14.0	16.0
	$\overline{\lvert E\%D \rvert}$					5.2	6.4

Table 4
Comparison of EFD and CFD ($n = 1.00$) results in regular head waves for the mean values of motions and the first harmonic amplitude of surge motion in the spring natural frequency.

λ/L	Data	EFD_1	EFD_2	$n = 1.00$			
				$E = CFD - EFD$		$E\%D = E/EFD \times 100$	
				E_1	E_2	$E\%D_1$	$E\%D_2$
0.6	$\bar{x}$ (m)	0.0284	−0.0011	−0.0253	0.0041	–	–
	x_{1_s} (m)	0.0054	*	−0.0034	*	−63.0	*
	$\bar{z}$ (m)	−0.0031	−0.0032	−0.0006	−0.0005	18.9	15.9
	$\bar{\theta}$ (deg)	0.085	0.125	0.020	−0.019	24.0	−15.5
1.1	$\bar{x}$ (m)	0.0708	−0.0165	−0.0795	0.0077	–	–
	x_{1_s} (m)	0.0096	*	−0.0017	*	−17.7	*
	$\bar{z}$ (m)	−0.0024	−0.0030	−0.0010	−0.0005	44.6	16.0
	$\bar{\theta}$ (deg)	0.089	0.319	0.042	−0.188	47.3	−58.9
1.6	$\bar{x}$ (m)	0.0166	0.0066	−0.0209	−0.0109	–	–
	x_{1_s} (m)	0.0093	*	0.0074	*	79.6	*
	$\bar{z}$ (m)	−0.0035	−0.0023	0.0003	−0.0009	−7.7	40.9
	$\bar{\theta}$ (deg)	0.188	0.177	−0.072	−0.061	−38.4	−34.7

– No meaningful comparison can be performed.
* Not available from EFD_2 data.

not be a valid choice. Moreover, the values are extremely small and close to zero, hence small changes will results in large deviations and the uncertainty of measurements can become essential. In Table 5, large scatters of z_1 and θ_1 are seen for $\lambda/L = 0.6$. Overall, the largest validation errors in Table 3 are mainly seen for the 1st harmonic amplitudes of pitch motion.

Table 5
Scatter of experimental data in the repeated model tests in EFD_1.

λ/L	No. of tests	$STD\%RMS$							
		$\bar{x}$	$\bar{z}$	$\bar{\theta}$	x_1	z_1	θ_1	$\bar{R}_T$	A
0.6	10	23.5	3.3	7.7	8.0	4.3	3.7	1.5	3.9
1.1	9	14.0	9.7	28.3	10.9	1.9	1.8	19.3	2.5
1.6	8	4.5	17.5	17.7	5.4	2.1	1.3	1.2	1.4

In all three wave lengths, the averaged absolute errors $\overline{|E\%D|}$, computed from averaging the absolute errors of the mean resistance and the 1st harmonic amplitudes of motions, are smaller in the validations against EFD_1 in comparison to EFD_2, both in dimensional and non-dimensional quantities. Moreover, $\overline{|E\%D|}$ is mainly reduced in both EFD data sets for the non-dimensional quantities in comparison to the dimensional ones, except in $\lambda/L = 0.6$ where the non-dimensionalization using only the wave amplitude might be questionable.

The MEAN values (time-averaged on the respective time window in each λ/L) of the wetted surface area of the hull as well as wall $\bar{y}^+$ (surface-averaged over the wetted surface area) in all three wave lengths are approximately close to the calm water values in each respective grid given in Section 5.1. A similar finding regarding the time-averaged wetted surface area in waves is reported in an earlier paper by Irannezhad et al. (2022) using a fully nonlinear potential flow solver.

6.2. Wake in regular waves

In this section, first, the grid convergence study is carried out for the surface-averaged nominal wake $\tilde{u}$ computed on the hull-fixed propeller disk in regular head waves simulations. Then, the carriage-fixed wake is compared between the experimental SPIV measurements and CFD computations. In order to have a better understanding of the time instances in which the wake computations and SPIV measurements are considered, the reconstructed time series as well as the synced last T_E time series, explained in Section 4.6.3, are provided.

Although the harmonic amplitudes of resistance and motions are already compared between CFD and EFD in Section 6.1, the harmonic phases are disregarded. In this section, a rather qualitative comparison can be performed on these harmonic phases by detecting the differences in terms of t/T_E, as the time origin for both CFD and EFD data are set to be when the wave crest is at the initial position of fore perpendicular. Moreover, the significance of the validation errors and the differences between grids can be perceived.

The FFT results of the surface-averaged nominal wake computed on the hull-fixed propeller disk for different grids in regular head waves are shown in Fig. 21. The same time window that has been used for the resistance and motions is considered for the Fourier analysis of $\tilde{u}$ in each respective wave length. The dominant bars are mostly seen at the integer values of the harmonic components ω/ω_E and the values of the harmonic amplitudes are shown in the plots legends. The 0th and 1st harmonic amplitudes are the dominant components in $\lambda/L = 0.6$ and the higher harmonic amplitudes are very small. On the other hand, those higher harmonic amplitudes in $\lambda/L = 1.1$ and 1.6 are not negligible, but still relatively small.

The grid convergence study is carried out for the 0th and 1st harmonic amplitudes of $\tilde{u}$ and the results are shown in Fig. 22. The numerical uncertainties of $\bar{\tilde{u}}$ in $\lambda/L = 0.6$ are approximately between 22% and 32%, which are significantly larger than the numerical uncertainties of the resistance and motions in this wave length, however, relatively similar to the numerical uncertainties of the calm water wake in Fig. 12(b). Interestingly, the numerical uncertainties of $\bar{\tilde{u}}$ in $\lambda/L = 1.1$ are lower than the respective values in calm water and the shorter wave $\lambda/L = 0.6$. The importance of grid refinement level on the accurate prediction of the bilge vortex is discussed in Section 5. In calm water

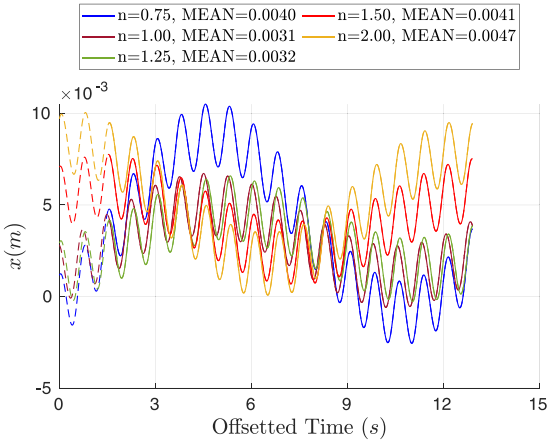

(a) Surge time series in $\lambda/L = 0.6$.

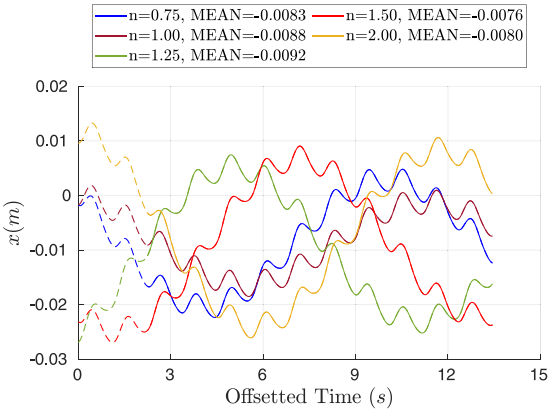

(b) Surge time series in $\lambda/L = 1.1$.

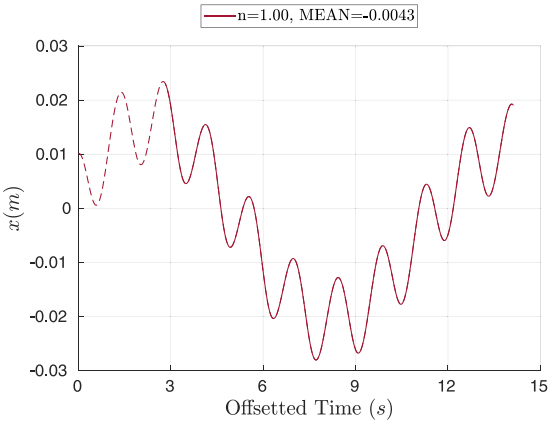

(c) Surge time series in $\lambda/L = 1.6$.

Fig. 19. Surge motion time series in regular head wave simulations.

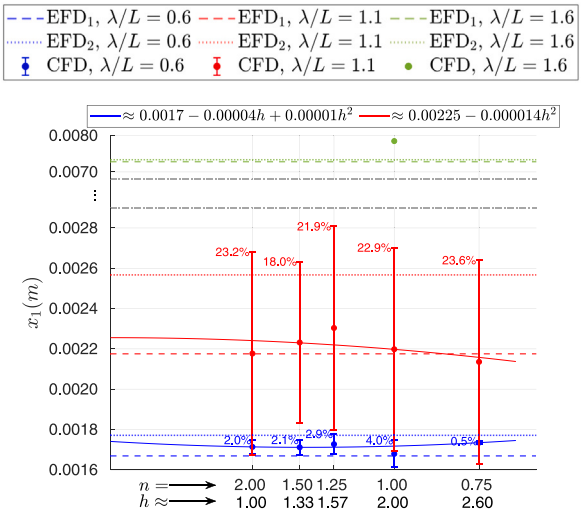

(a) 1st HA of surge motion.

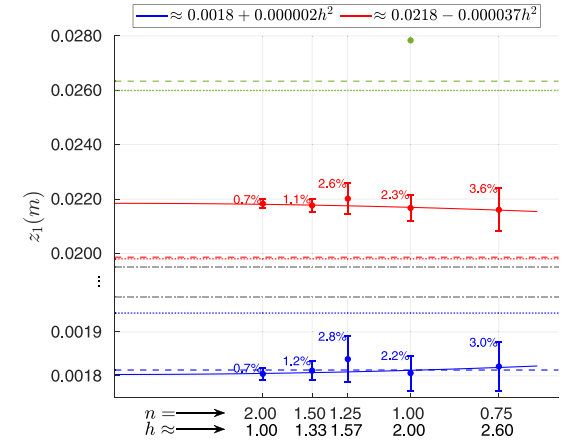

(b) 1st HA of heave motion.

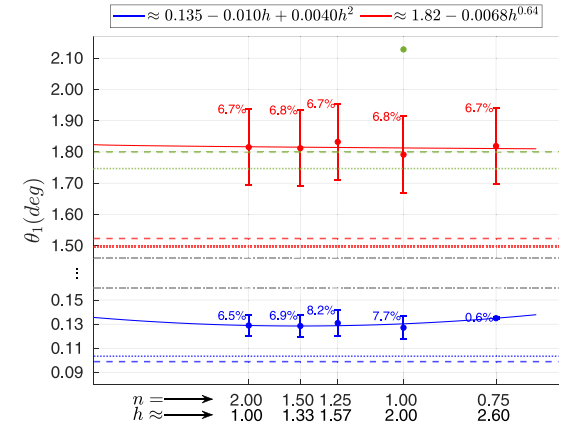

(c) 1st HA of pitch motion.

Fig. 20. V&V on the motions 1st harmonic amplitudes in regular head waves.

and in the shortest wave $\lambda/L = 0.6$, the location where the bilge vortex hits the propeller disk remains more or less stationary during the ship performance. Consequently, the accuracy of the computed wake is affected by the flow-driven accumulated effects from the prediction of bilge vortex, thus a strong dependency on the grid refinement level and hence larger numerical uncertainties are observed. On the other hand, in the longer waves, the bilge vortex meanders and even exits the propeller disk during one encounter wave period. Therefore, the accuracy of the computed wake is mainly governed by the ship dynamics while the flow-driven effects from bilge vortex prediction

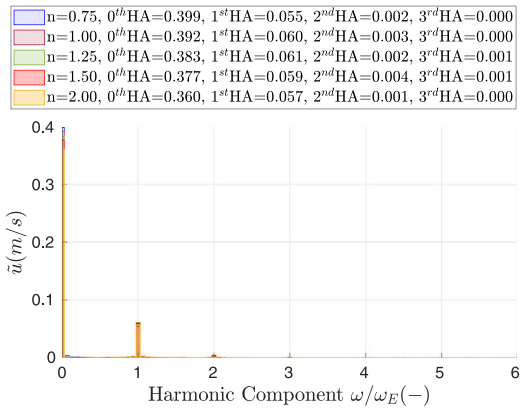

(a) FFT results in $\lambda/L = 0.6$.

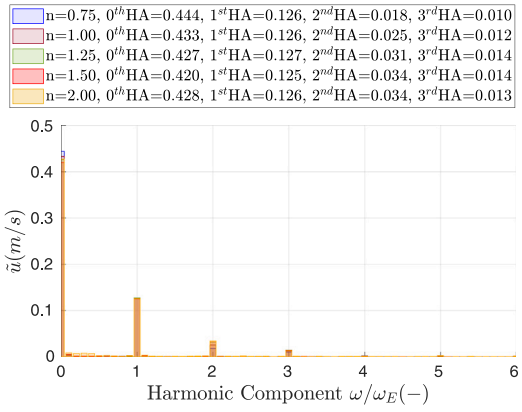

(b) FFT results in $\lambda/L = 1.1$.

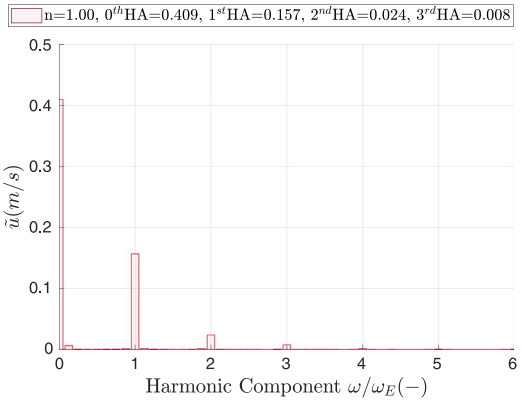

(c) FFT results in $\lambda/L = 1.6$.

Fig. 21. FFT analysis of the surface-averaged axial velocity component of wake on the hull-fixed propeller disk in regular head waves simulations.

become less consequential. The observed numerical uncertainties of the 1st harmonic amplitude of $\tilde{u}$ in $\lambda/L = 0.6$ and $\lambda/L = 1.1$ can likewise be attributed to the same explanation.

The reconstructed and synced last T_E time series for three wave conditions are shown in Figs. 23–25. SPIV time instances in EFD_1 and EFD_2 are represented by vertical lines. Reconstructed time series are generated based on the explanations in Section 4.6.3 where different quantities are reconstructed up to different harmonic components (HCs, i.e., harmonic amplitudes and phases) using the Fourier series.

The time series of the free surface elevation ζ in EFD_1 and EFD_2 are reconstructed up to the 1st and 3rd HCs, respectively, due to the availability of similar information from model tests. On the other hand, since the 5th order Stokes waves are considered in the simulations, ζ is reconstructed up to the 5th HCs in CFD. Surge, heave and pitch motions are reconstructed up to the 1st HCs in both EFD and CFD. Total resistance as well as the surface-averaged wake over the hull-fixed propeller disk are reconstructed up to the 5th HCs in CFD. The main reason is that the higher harmonic components are not negligible in some wave lengths, as evidenced by the Fourier analysis shown in Figs. 17 and 21. The time series for $\tilde{v}$ and $\tilde{w}$ for different grids in the CFD simulations are shown in Figs. A.3–A.5 in Appendix, but not further analyzed in this paper.

The reconstructed and synced last T_E time series of the wave elevation from the CFD simulations in Figs. 23(a), 24(a) and 25(a) are in a good agreement. The differences between different grids are insignificant and the computed wave elevation resembles well to the analytical wave in each condition. The largest discrepancies are seen for the coarsest grid $n = 0.75$.

It should be reminded that the wave elevation close to the hull is affected by the hull. Thereby, in order to show the wave elevation from CFD, the monitored wave elevation at the wave probe in Fig. 4 is analyzed and used in Figs. 23(a), 24(a) and 25(a). The monitored wave at the wave probe is offsetted in time in order to estimate the expected wave elevation at the initial position of the ship fore perpendicular using the 5th order Stokes wave mean velocity and the ship velocity. This may introduce a potential source of discrepancy in the comparisons as there is no practical way to estimate the exact wave elevation at the ship fore perpendicular. However, as discussed earlier, based on the preliminary investigations in Irannezhad (2022), insignificant deviations (less than 3%) are expected with the current simulation setup.

The wave height measurements in the towing tank tests are also carried out at some distance in front of the hull, explained in Section 3, and then offsetted in time in order to represent the wave elevation at the ship fore perpendicular. Generally, the quality of the waves in the current experimental measurements is lower than the quality of the CFD waves. The discrepancy of the measured wave amplitudes from the analytical values in EFD_1 in $\lambda/L = 0.6$, 1.1 and 1.6 are under-prediction by 3.9%, 2.5% and 3.6%, respectively. The measured wave amplitudes in EFD_2 in $\lambda/L = 0.6$, 1.1 and 1.6 are under-predicted by 10.8%, 1.8%, 4.7%, respectively. Based on these deviations as well as the scatter of wave amplitudes in the repeated tests in EFD_1 shown in Table 5, the steepest wave is presumed to be the most critical one in terms of generation and propagation in the towing tank. The potential effects on the hydrodynamic response of the ship are discussed in Section 6.1.

The surge motion reconstructed time series from EFD and CFD as well as the synced last T_E time series from the CFD simulations are shown in Figs. 23(b), 24(b) and 25(b). The reconstructed time series from different grids in CFD are very similar in each wave length in terms of magnitudes of both mean value and 1st harmonic amplitude, as it is also seen in Section 6.1.

The discontinuity of the surge motion synced last T_E time series is explained in Section 4.6.3. The difference in the mean values for the synced last T_E time series is originated from the fact that in each simulation the last T_E can represent a different time period of the spring natural period as it is shown in Fig. 19. Consequently, the reconstructed time series and the synced last T_E time series are not similar in terms of mean values, but they are comparable in terms of the 1st harmonic amplitude.

It is assumed that $\tilde{u}$ exhibit an approximately harmonic behavior with respect to the wave encounter frequency and its amplitude in the spring natural frequency is negligible (less than 1.5%), hence the wake contour plots in the last encountered wave of the simulations can be generalized for the whole time window. On the other hand, due to the presence of the spring, the instantaneous position of the carriage-fixed planes with respect to the hull may vary between different simulations with different grids. The reason is that the hull is subjected to different

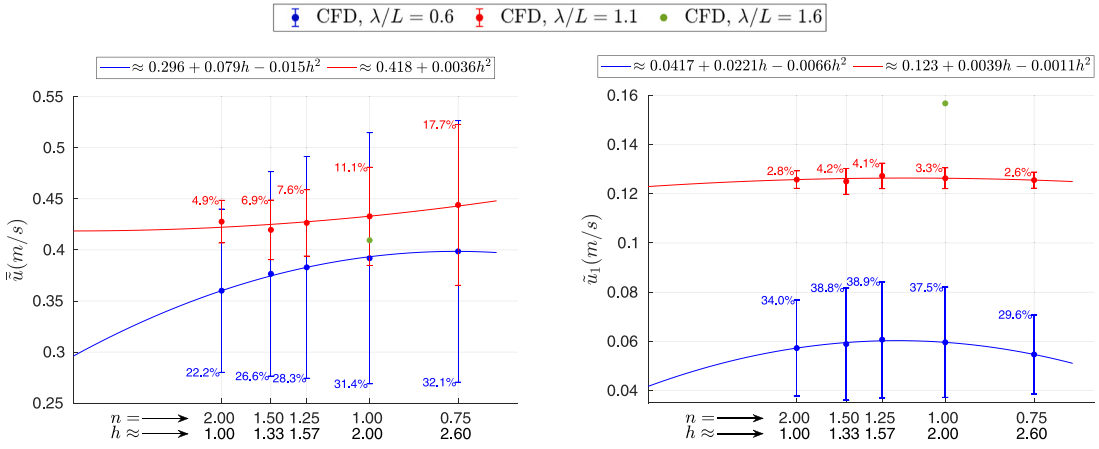

(a) 0th harmonic amplitude. (b) 1st harmonic amplitude.

Fig. 22. Grid convergence study of the MEAN and 1st harmonic amplitude of the surface-averaged axial velocity component of wake on the hull-fixed propeller disk in regular head waves.

instantaneous surge values in the last encountered wave in which the wake is extracted from the simulations. In other words, the hull moves in the longitudinal direction due to its surge motion and since the instantaneous surge values are different between various grids, the instantaneous position of the carriage-fixed planes with respect to the hull may vary between different grids. This should be highlighted as an important source of discrepancy in the wake comparisons in the carriage-fixed planes. Moreover, the CFD wake is only recorded at each computed time step, therefore, there might be a minor time difference between the time instances in different grids.

The reconstructed times series of surge motion from EFD and CFD are comparable in terms of the 1st harmonic amplitudes, as it is studied in Section 6.1. However, the differences in the 0th harmonic amplitudes are considerable, especially in EFD_1. These differences are mainly caused by the arbitrary choice of F_0 in different conditions. There are two major consequences originated from the differences in the mean values of the reconstructed times series of surge motion from EFD and CFD.

Firstly, it introduces a phase difference between the motions time series in EFD and CFD when the reconstructed time series are offsetted to the defined origin $t/T_E = 0$. The reason is that the ship motions are measured/calculated at the instantaneous ship COG while the time series are offsetted based on the time in which the wave crest is located at the initial position of the ship fore perpendicular. The wave is measured at the wave gauge mounted on the carriage, therefore, it is not moving with the hull. When the mean surge is not identical in different conditions, the distance from the instantaneous position of COG to the initial position of the ship fore perpendicular is also not identical.

These phase differences can be clearly detected in the reconstructed time series of surge, heave and pitch motions in Figs. 23–25. More pronounced phase differences ($\approx$ 10–20 deg) are observed in EFD_1, mainly because the mean values of the surge in EFD_1 are substantially different from the ones in EFD_2 and CFD, shown in Table 4 and Figs. 23(b), 24(b) and 25(b). This is one of the complex effects of the spring and there is no straightforward way, due to the limited information from the model tests, to include such effects in the current investigations.

As the second consequence of the differences in the mean values of the reconstructed times series of surge motion from EFD and CFD, the carriage-fixed plane locations with respect to the model in EFD varies substantially from the initial position of plane locations. These variations together with the fact that the CFD wake is just extracted in the last T_E in each simulation, pose an important potential source of discrepancy in the wake comparison between CFD and EFD.

The heave and pitch motions reconstructed time series from EFD and CFD as well as the synced last T_E time series from the CFD simulations are shown in Figs. 23(c), 23(d), 24(c), 24(d), 25(c) and 25(d). Although the reconstruction is carried out for up to the 1st harmonic components, the reconstructed time series are very well matching the synced last T_E time series. The reconstructed time series from different grids in CFD are comparable in each wave length in terms of magnitudes of both mean value and the 1st harmonic amplitude. The largest deviations are mostly seen for the coarsest grid $n = 0.75$, especially in the shortest wave length. The results are also comparable between EFD and CFD, which is discussed in Section 6.1.

The reconstructed and the synced last T_E time series of the total resistance from CFD simulations are shown in Figs. 23(e), 24(e) and 25(e). Insignificant deviations are seen between different grids for the resistance time series and the reconstructed resistance time series correspond well to the synced last T_E time series in each grid.

Although the reconstructions are carried out for up to 5th HCs for the time series of $\tilde{u}$, the reconstructed time series are not properly coincided with the synced last T_E time series in $\lambda/L = 1.1$ in Fig. 24(f). In the shorter and longer waves in Figs. 23(f) and 25(f), the reconstructed and the synced last T_E time series are more similar in each grid. In an overall comparison of $\tilde{u}$, very significant differences are seen between the time series of different grids in the same wave length. This may declare the importance of grid refinement on the computed nominal wake while the resistance and motions computations are not susceptible as much to the level of refinement. The same is seen in the wake investigations in calm water simulations between different grids, which show significant differences based on the refinement levels while the motions are almost identical.

The CFD and EFD wake comparisons in some selective conditions are shown in Figs. 26–28. The comparison of the computed (for $n = 1.00$) and measured wakes in the remaining conditions are provided in Appendix.

Despite the possible sources of discrepancy mentioned throughout the paper, the EFD and CFD wakes are comparable. The difference in Reynolds number for different data sets should not be overlooked as well. The effects of symmetry boundary condition, which are discussed in the wake comparison in calm water, are also present in waves. The finer grids predicted a larger bilge vortex in comparison to the coarser ones and it can be seen that the CFD wake in finer grids is becoming more similar to the SPIV wake. The secondary vortex generated under the hub due to the moving shaft is generally more pronounced in the CFD wake.

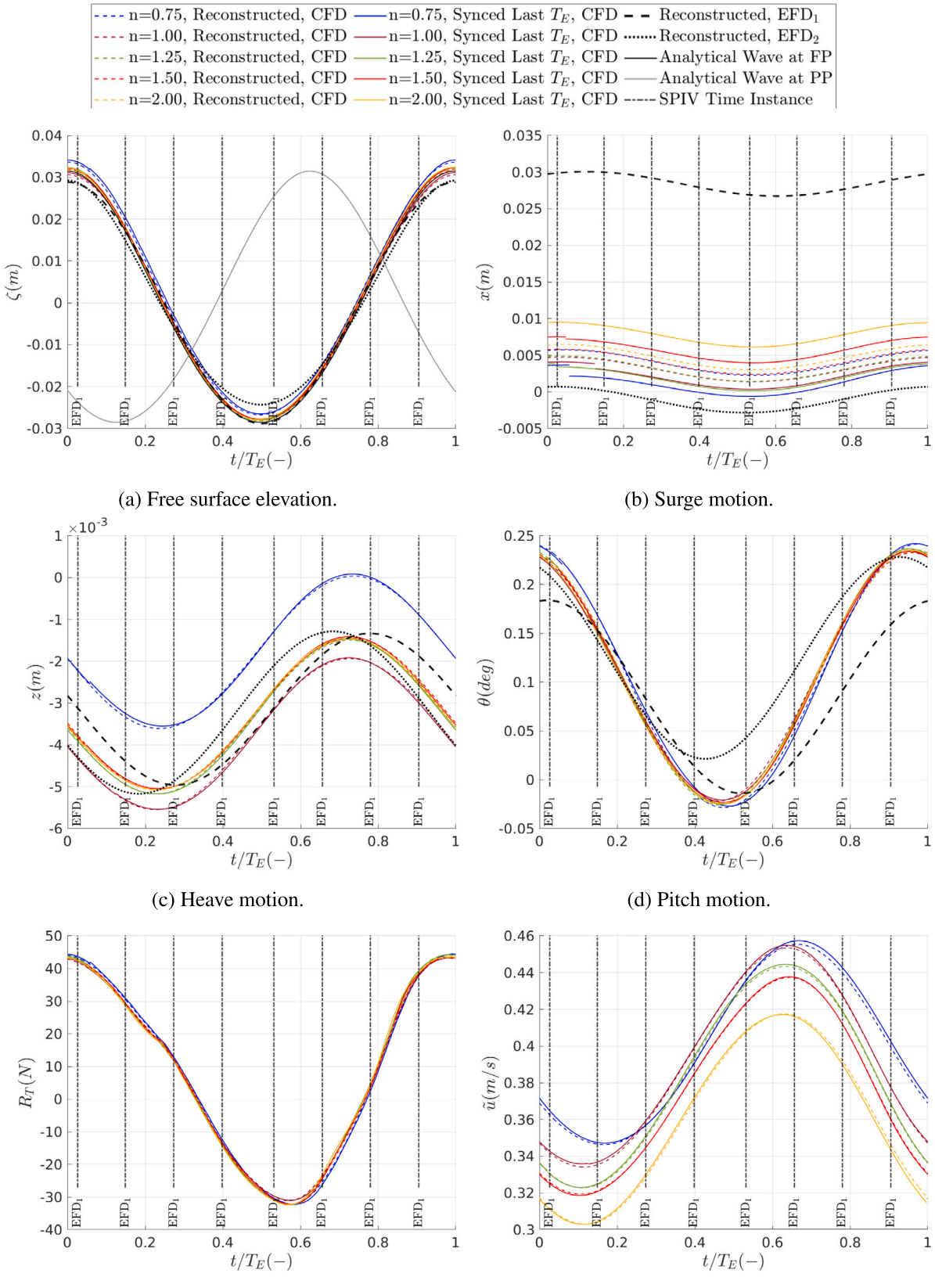

(a) Free surface elevation.

(b) Surge motion.

(c) Heave motion.

(d) Pitch motion.

(e) Total resistance.

(f) Axial velocity component of wake.

Fig. 23. Reconstructed and synced last T_E time series in $\lambda/L = 0.6$.

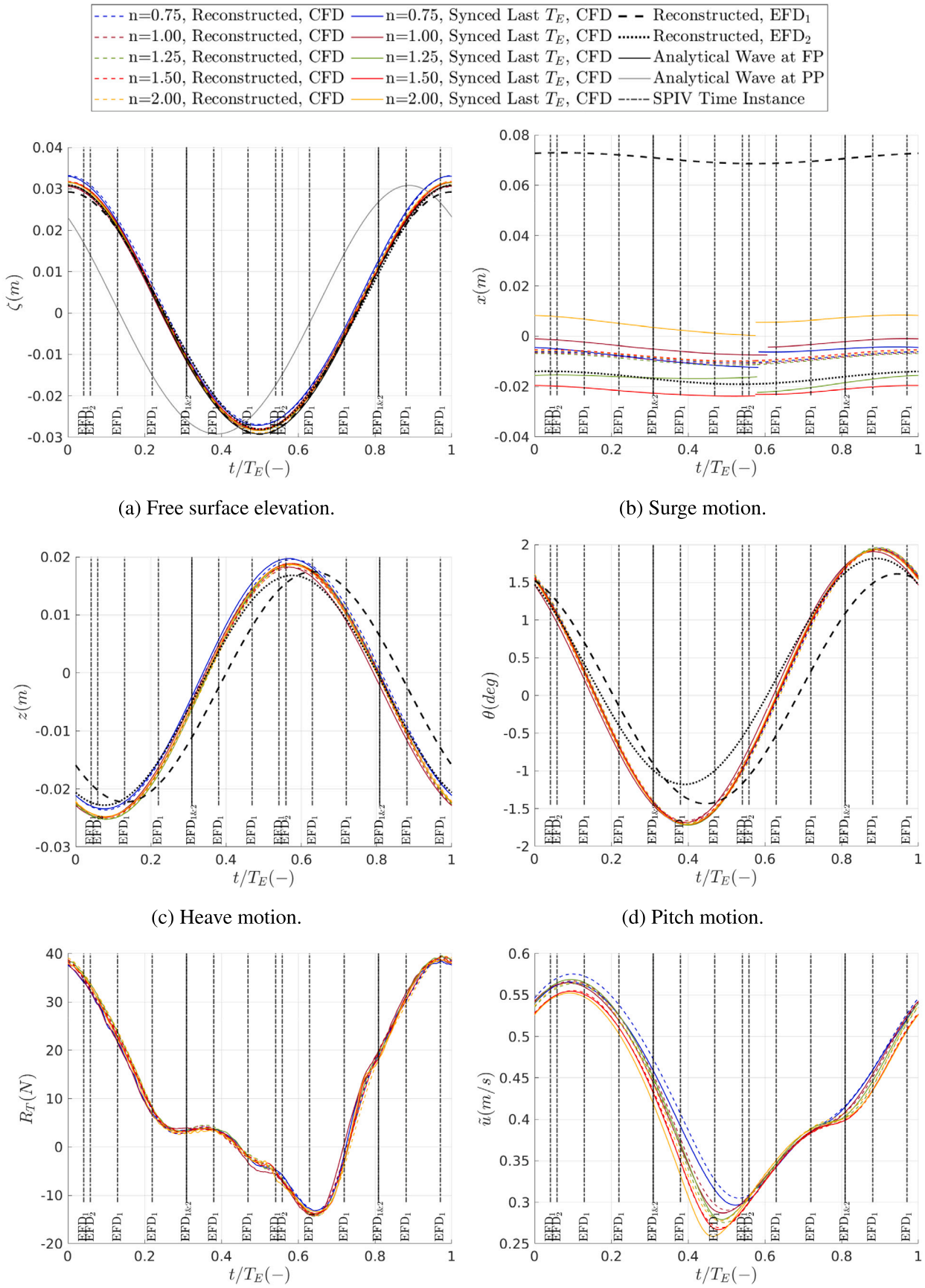

(a) Free surface elevation.

(b) Surge motion.

(c) Heave motion.

(d) Pitch motion.

(e) Total resistance.

(f) Axial velocity component of wake.

Fig. 24. Reconstructed and synced last T_E time series in $\lambda/L = 1.1$.

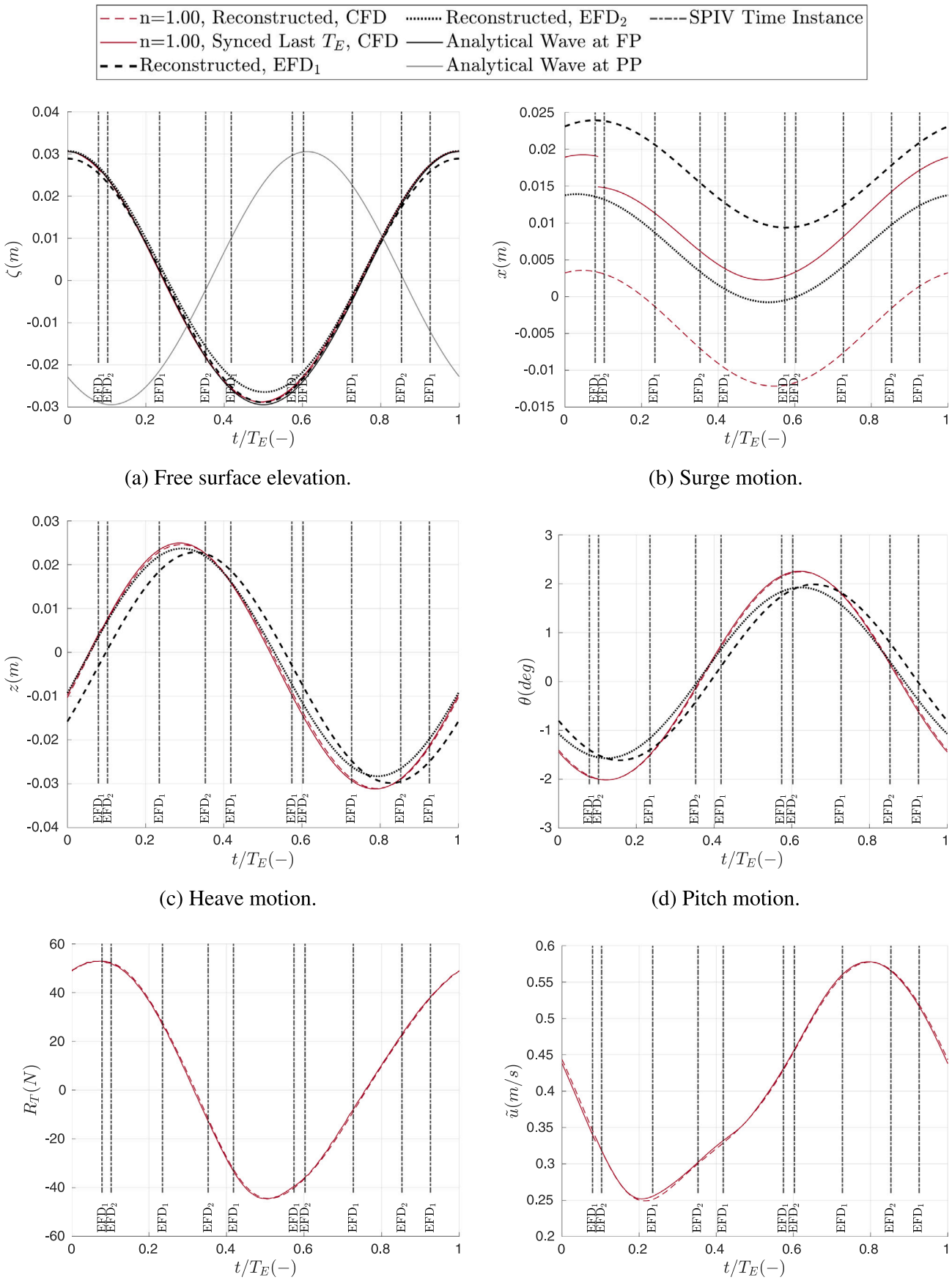

(a) Free surface elevation.

(b) Surge motion.

(c) Heave motion.

(d) Pitch motion.

(e) Total resistance.

(f) Axial velocity component of wake.

Fig. 25. Reconstructed and synced last T_E time series in $\lambda/L = 1.6$.

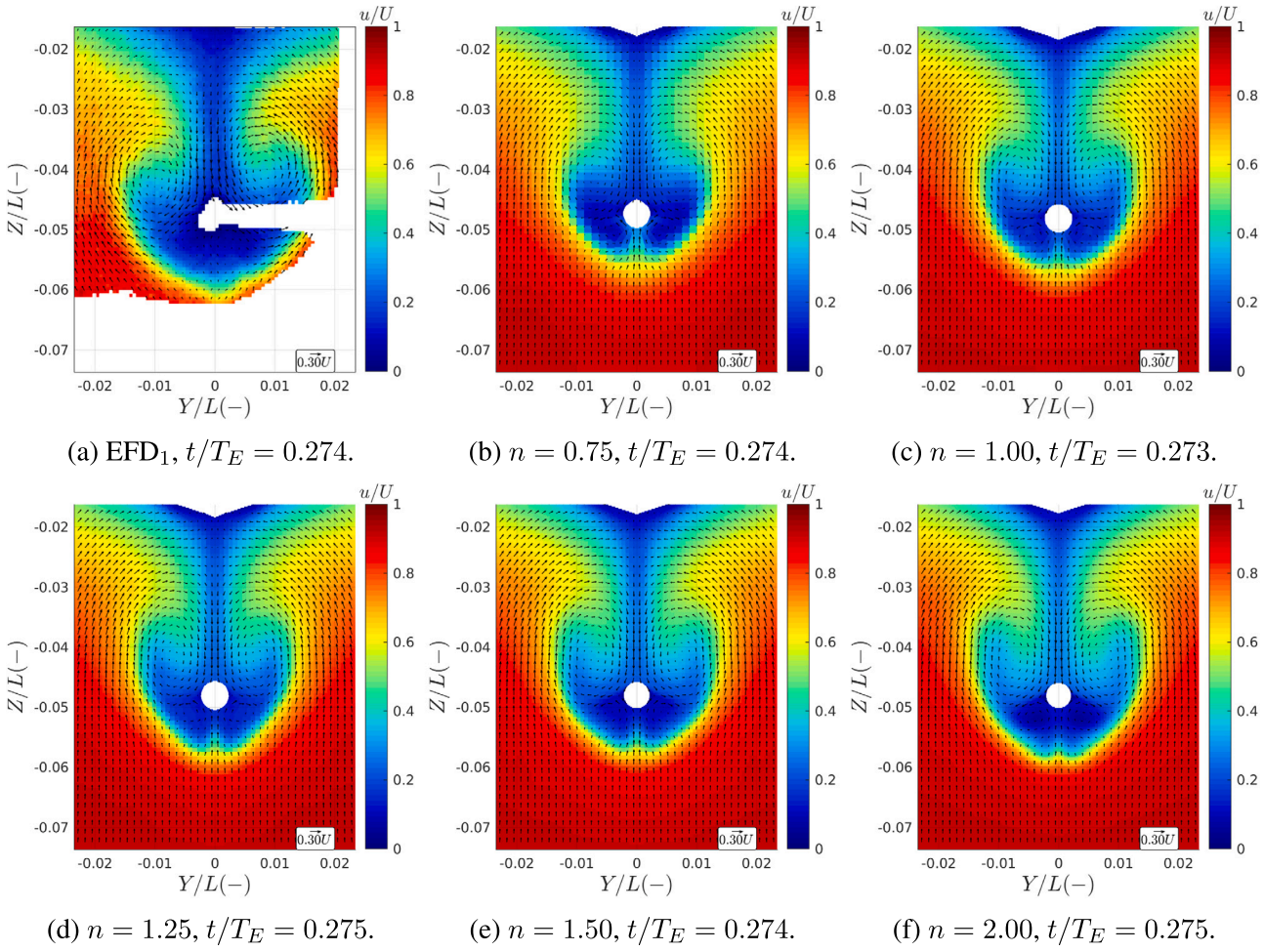

(a) EFD_1, $t/T_E = 0.274$. (b) $n = 0.75$, $t/T_E = 0.274$. (c) $n = 1.00$, $t/T_E = 0.273$.

(d) $n = 1.25$, $t/T_E = 0.275$. (e) $n = 1.50$, $t/T_E = 0.274$. (f) $n = 2.00$, $t/T_E = 0.275$.

Fig. 26. EFD_1 and CFD wake comparison in the carriage-fixed plane at the initial position of propeller plane (CF_{PP}) in $\lambda/L = 0.6$ at $t/T_E \approx 0.274$.

7. Analyses and discussions

In Sections 5 and 6, the verification and validation analysis is performed for the simulations in calm water and regular head waves. In the current section, the ship hydrodynamic performance in these operational conditions is analyzed and compared using solely the CFD results. To this end, the results of free surge simulations (3DOF) in calm water and in three regular head waves only with the grid $n = 1.00$ are considered. The reconstructed time series as well as the synced last T_E time series in the simulations of the three regular head waves are combined with the calm water simulations results and shown in Fig. 29. It should be reminded that, the origin of the time series $t/T_E = 0$ is considered as the time in which the wave peak is located at the initial position of the ship fore perpendicular, as it was explained in Sections 4.6.3 and 6. It should be noted that the encounter wave period T_E is different in each wave length, but t/T_E is used in these plots in order to compare the results of all three wave lengths in one encounter period of each wave condition.

The monitored free surface elevation at the wave probe in the simulations, shown in Fig. 29(a), is similar to the analytical wave and, as discussed before, the potential discrepancies of the incident wave are deemed insignificant. In this figure, the analytical wave at the initial position of the propeller plane (PP) is also provided in order to enhance the understanding of the correlations between the waves and the ship nominal wake.

7.1. Motions and resistance

The surge motion time series are given in Fig. 29(b). The minimum surge in all three waves is occurring near $t/T_E \approx 0.5$, i.e., when the wave trough is close to the ship fore perpendicular. The surge motion is relatively small in terms of magnitude in all three wave lengths.

As it is also seen in Table 3, z_1 and θ_1 are noticeably larger in $\lambda/L = 1.1$ and 1.6 in comparison to the shortest wave, hence rather large variations are seen during one encounter period for the heave and pitch motions in $\lambda/L = 1.1$ and 1.6 in Figs. 29(c) and 29(d). Such motions can result in an increased variation of the ship nominal wake.

Based on Fig. 29(e), higher harmonic amplitudes of resistance play a crucial role in the resistance time series. Although the behavior of z and θ during one encounter period ($t/T_E = 0$ to 1) is completely different in different wave lengths, the behavior of R_T is roughly similar for all three waves, with negative total resistance values occurring approximately in $0.25 < t/T_E < 0.75$. The maximum/minimum resistance values are seen when the wave crest/trough is close to the ship fore perpendicular.

It is seen in Fig. 17 that the mean of the total resistance in $\lambda/L = 1.1$ is larger than the other two waves. On the other hand, the departure of the transient total resistance in $\lambda/L = 1.1$ from its time-averaged (MEAN) value is smaller in comparison to the shorter and longer wave lengths. Basically, this is due to the effects of the higher harmonic amplitudes on the total resistance time series. In the vicinity of $t/T_E \approx 0.5$, a smaller decrease in resistance is seen in $\lambda/L = 1.1$ in comparison to $\lambda/L = 0.6$ and 1.6, resulting in a larger MEAN value in $\lambda/L = 1.1$. Interestingly, this means that although the propeller of a self-propelled

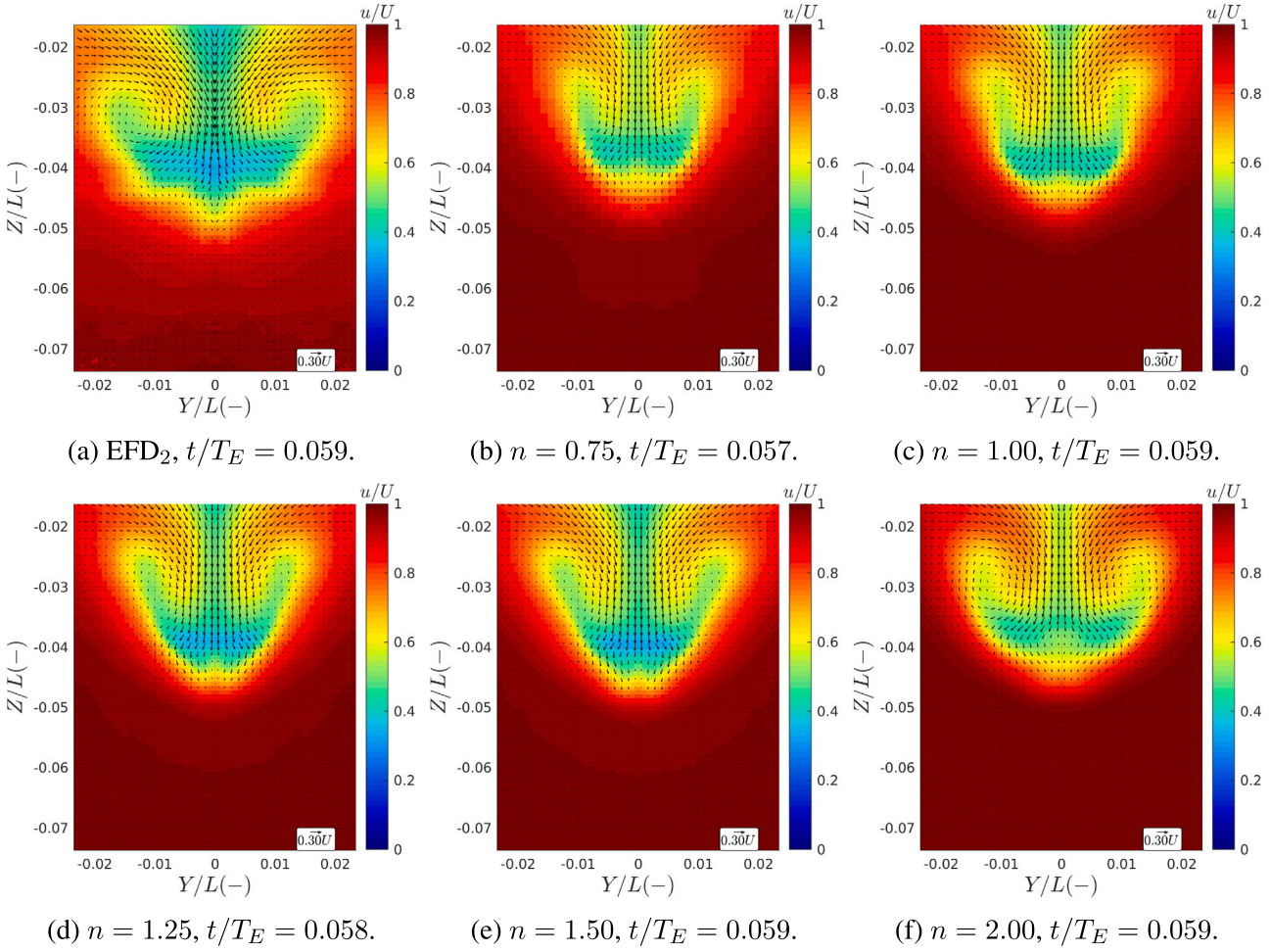

(a) EFD_2, $t/T_E = 0.059$. (b) $n = 0.75$, $t/T_E = 0.057$. (c) $n = 1.00$, $t/T_E = 0.059$.

(d) $n = 1.25$, $t/T_E = 0.058$. (e) $n = 1.50$, $t/T_E = 0.059$. (f) $n = 2.00$, $t/T_E = 0.059$.

Fig. 27. EFD_2 and CFD wake comparison in the carriage-fixed plane at the initial position of aft perpendicular (CF_{AP}) in $\lambda/L = 1.1$ at $t/T_E \approx 0.059$.

hull in $\lambda/L = 1.1$ has to deliver a larger averaged thrust in comparison to the other wave lengths, the load variation and consequently the maximum and minimum loading conditions on the propeller will be more severe in the shorter and longer wave lengths. Such load variations can impose several design constraints both for the propeller and the machinery system. However, it should be noted that the thrust generation mechanism is also dependent on the hull wake. The wake in waves can vary significantly which can result in propeller thrust variations, and consequently, resistance and thrust imbalance.

The resistance components, i.e., pressure resistance and shear resistance, are reconstructed up to the 5th harmonic components and shown in Figs. 29(i), 29(j), respectively. The pressure resistance is the dominant resistance component, hence the trend of total resistance mainly follows the trend of this component.

The MEAN shear resistance in calm water for the grid $n = 1.00$ is 3.49 N. For the simulations with the same grid in $\lambda/L = 0.6$, 1.1 and 1.6 the MEAN shear resistance values are 3.66 N, 3.69 N and 3.58 N, which are representing 4.9%, 5.7% and 2.6% increase from the calm water value. The added resistance values, derived by subtracting the calm water total resistance from the total resistance in waves, for grid $n = 1.00$ in $\lambda/L = 0.6$, 1.1 and 1.6 are 2.50 N, 6.77 N and 1.95 N, respectively. Therefore, the contribution of added shear resistance on the total added resistance of the hull is 6.8%, 2.9% and 4.6% for the shortest wave to the longest one, which is relatively small but not negligible. Similar observations are also reported by Guo et al. (2012) for KVLCC2 in regular head waves. As presented in Section 6.1 the time-averaged wetted surface area in waves remains almost equal to the calm water value. This reveals the fact that the wetted surface area cannot be used directly for the estimation of frictional resistance, e.g., using the ITTC-57 model-ship correlation line. Sigmund (2019) mentioned that the added resistance can have a significant (20% or more) frictional part in short waves in model scale, resulting from the orbital velocities in waves which are causing the molecular and turbulent shear stresses to increase, leading to higher frictional forces acting on the wetted surface area of hulls.

7.2. Nominal wake

7.2.1. Surface-averaged wake

In Fig. 29(f), the time series of the axial velocity component of the nominal wake at the hull-fixed propeller disk is shown. The harmonic amplitudes of $\bar{u}$ in waves are shown in Fig. 21. The MEAN values in all three waves are larger (approximately 9.8%, 21.3% and 14.6% for $\lambda/L = 0.6$, 1.1 and 1.6, respectively) than the calm water value given in Fig. 12(a). This can also be observed in Fig. 29(f). Important effects from the higher harmonic amplitudes of $\bar{u}$ can be seen in the time series of $\lambda/L = 1.1$ and 1.6, however, such effects are less pronounced in $\lambda/L = 0.6$. Although the 1st harmonic amplitude of $\bar{u}$ is larger for the longest wave $\lambda/L = 1.6$, the MEAN value is larger in $\lambda/L = 1.1$. Large MEAN value of $\bar{u}$ in $\lambda/L = 1.1$ could result in lower expected thrust generation while the MEAN resistance is large for this wave, which should be of interest for ship/propeller designers.

It is seen in Fig. 29(e) that the total resistance in all three studied wave lengths is low in the vicinity of $t/T_E \approx 0.5$ and high close to $t/T_E \approx 0$ and 1. However, the high or low values of the axial velocity component of the wake are occurring in different time instances in

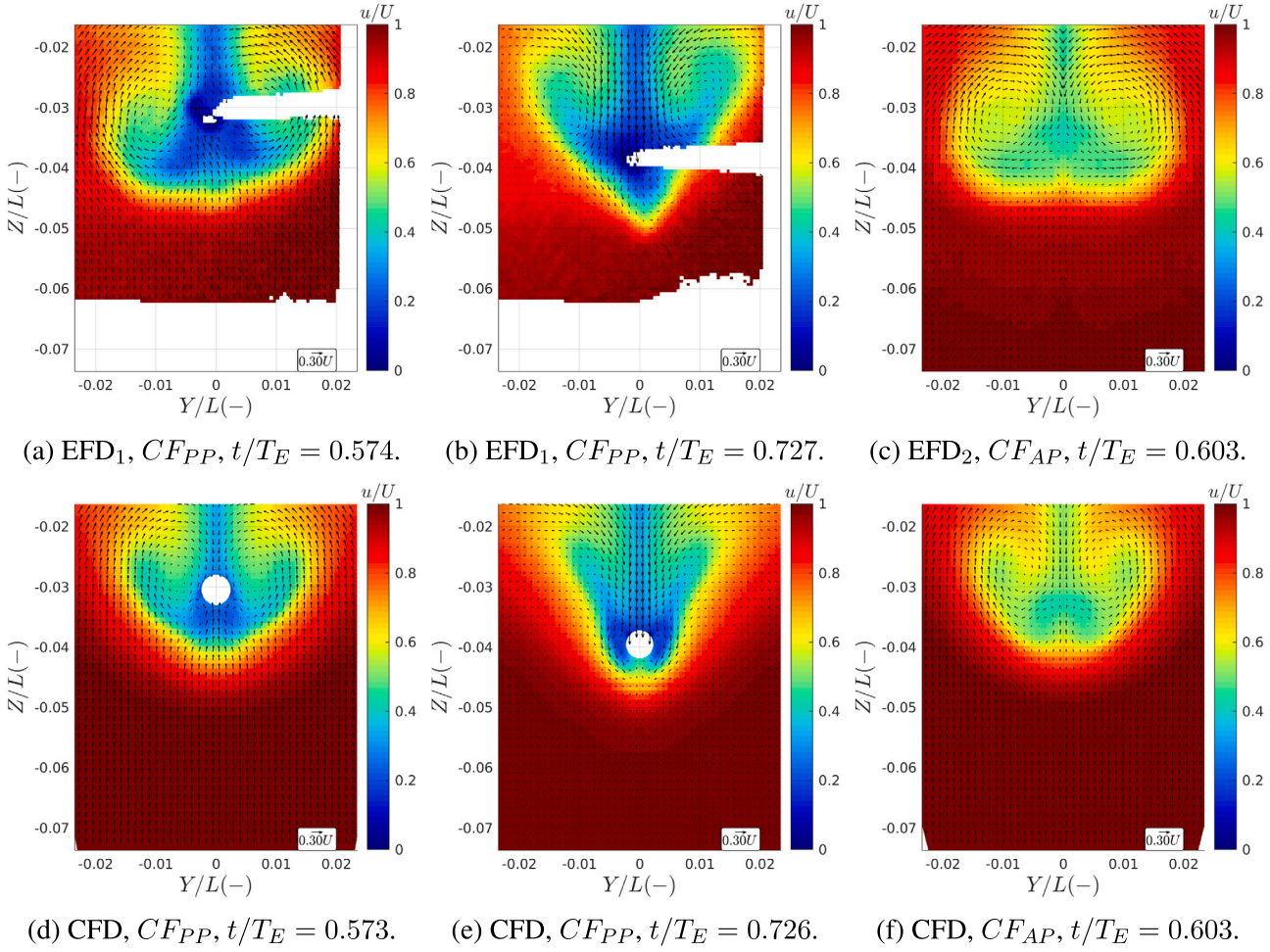

(a) EFD$_1$, CF_{PP}, $t/T_E = 0.574$. (b) EFD$_1$, CF_{PP}, $t/T_E = 0.727$. (c) EFD$_2$, CF_{AP}, $t/T_E = 0.603$.

(d) CFD, CF_{PP}, $t/T_E = 0.573$. (e) CFD, CF_{PP}, $t/T_E = 0.726$. (f) CFD, CF_{AP}, $t/T_E = 0.603$.

Fig. 28. EFD and CFD ($n = 1.00$) wake comparison in the carriage-fixed planes at the initial position of propeller plane (CF_{PP}) and the initial position of aft perpendicular (CF_{AP}) in $\lambda/L = 1.6$ at three time instances t/T_E.

each wave length. For instance, in $\lambda/L = 1.1$, the low values of $\tilde{u}$ approximately coincide with the low resistance conditions. Consequently, the required instantaneous thrust to overcome the instantaneous resistance is lower while, assuming a constant propeller rotation speed, the propeller thrust increase due to the low axial inflow velocity into the propeller disk. On the other hand, the high values of $\tilde{u}$ in $\lambda/L = 1.1$ approximately coincide with the high resistance conditions, resulting in lower expected propeller thrust. At the same time, there is a high thrust demand to overcome the instantaneous resistance. The excess or the deficit of the propeller thrust relative to the total instantaneous resistance together with the surge velocity of the ship will be governing the instantaneous velocity of the ship in self-propulsion. The correlation between the instantaneous resistance (demanded thrust) and the wake into the propeller is rather opposite in $\lambda/L = 0.6$ and the lower/higher required thrust occurs when there is a lower/higher expected thrust generation from the variation of $\tilde{u}$. Nevertheless, significant variation of resistance during one encounter period is seen in $\lambda/L = 0.6$, while the departure of transient $\tilde{u}$ from its time-averaged value is rather small. In $\lambda/L = 1.6$, the high and low resistance time intervals coincide with the moderate propeller loading conditions. The instantaneous resistance and thrust imbalance lead to changes in surge velocity, either increasing or decreasing it. Consequently, these changes affect the instantaneous velocity into the propeller disk, resulting in either decreased or increased instantaneous propeller thrust, respectively. The change of propeller thrust will also alter the propeller suction effect and thus the thrust deduction fraction, resulting in a change in the instantaneous resistance. The maximum and minimum of axial velocity of the wake vary in between 15%–40% of the mean value, as shown in Fig. 29(f). Based on the generic propeller open water curves, at lower advance velocities thrust varies almost within the same range as the wake variations, however, the thrust variation can be larger at higher advance velocities where the propeller thrust is close to thrust breakdown. The maximum and minimum of total resistance vary between 250%–800% of the mean value, shown in Fig. 29(e), which is substantially larger than the thrust changes caused by the wake variations. This highlights the importance of resistance variations relative to wake variations on the propeller thrust. To conclude, the analysis of the instantaneous resistance, wake and consequent thrust can assist in understanding the instantaneous expected speed of a self-propelled ship, however, it should be noted that all the instantaneous propulsive factors will be affected and it can be a cumbersome task to identify all the interaction effects correctly only through estimating the interaction effects based on bare hull performance in waves. After all, it should also be mentioned that the resistance and thrust balance should be achieved over a full wave encounter period since there will be an imbalance between instantaneous resistance and thrust throughout a full period.

The surface-averaged transversal velocity component of the nominal wake at the propeller disk (reconstructed up to the 5th harmonic component) is shown in Fig. 29(g). The transversal velocity component is only taken into account for half of the disk located in the positive Y direction from the symmetry plane because the surface-averaged value over the full disk is always zero. The MEAN value of $\tilde{v}$ in calm water is approximately -0.010 m/s. The MEAN values

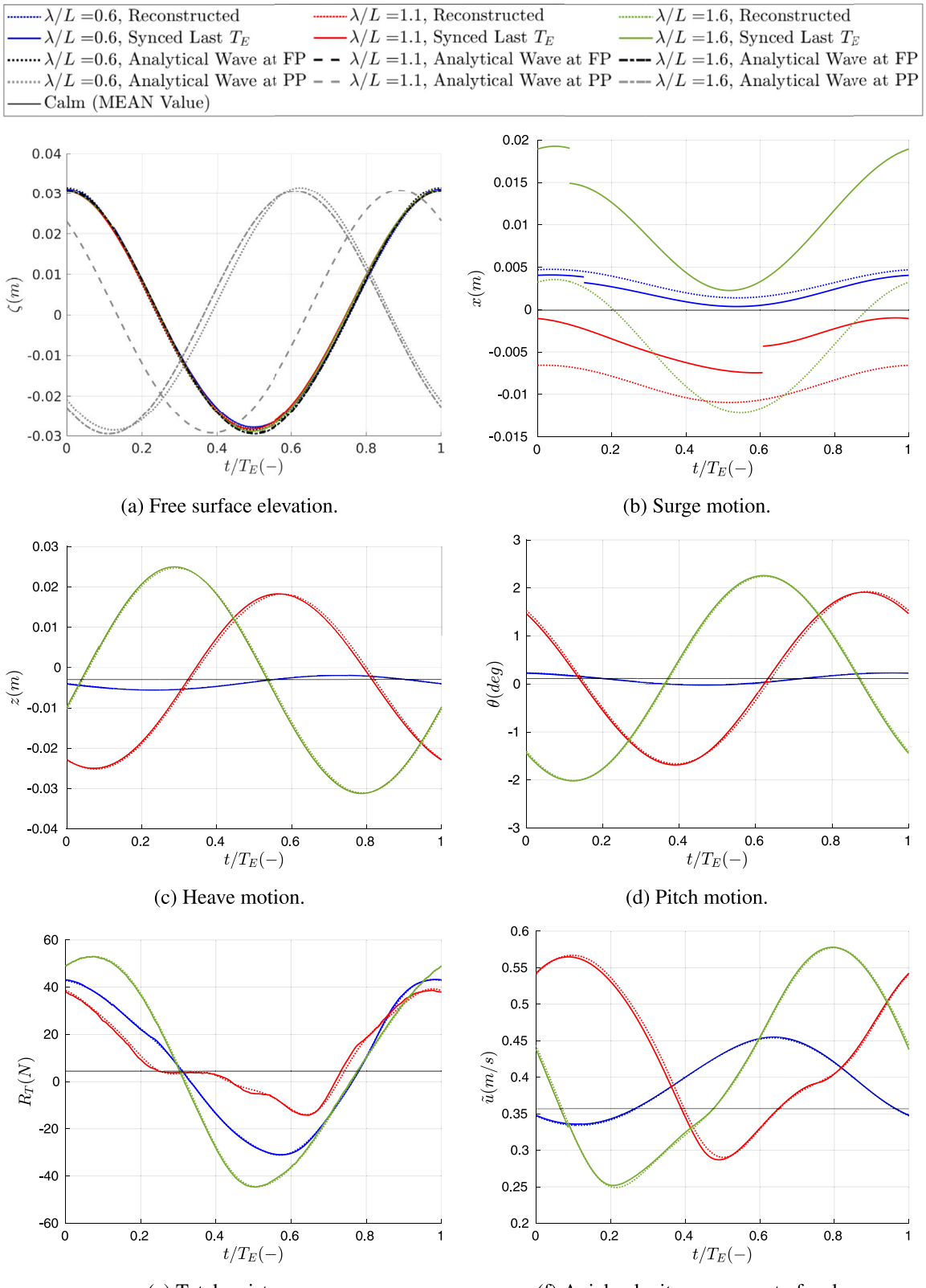

(a) Free surface elevation.

(b) Surge motion.

(c) Heave motion.

(d) Pitch motion.

(e) Total resistance.

(f) Axial velocity component of wake.

Fig. 29. CFD results for the grid n = 1.00 in calm water and in regular head waves. For calm water, a horizontal line is used which is representing the MEAN value over the chosen time window. For regular waves, the synced last T_E as well as the reconstructed time series (derived from the FFT analysis in the chosen time windows) are used.

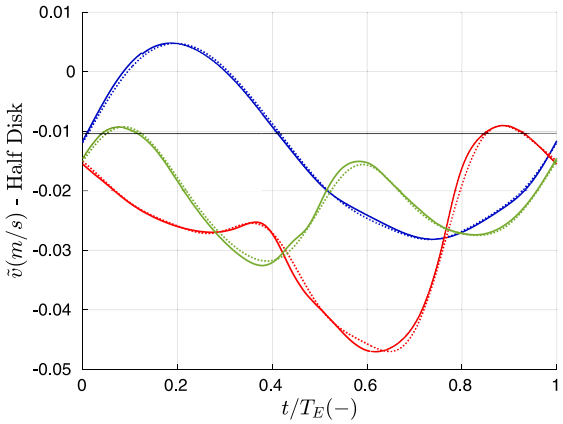

(g) Transversal velocity component of wake.

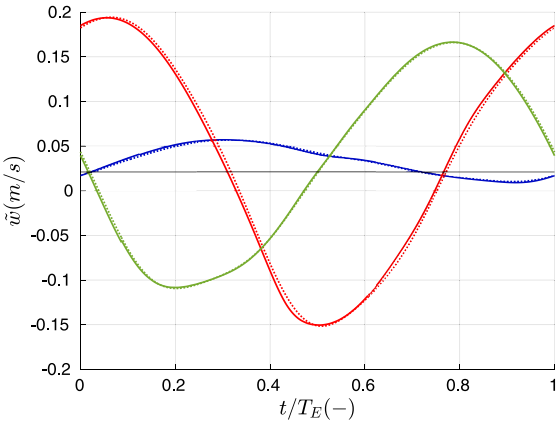

(h) Vertical velocity component of wake.

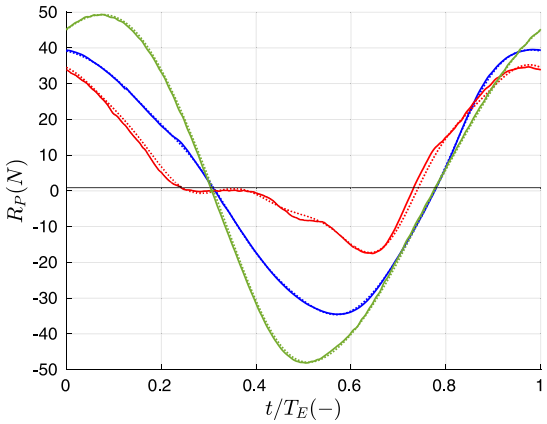

(i) Pressure resistance component.

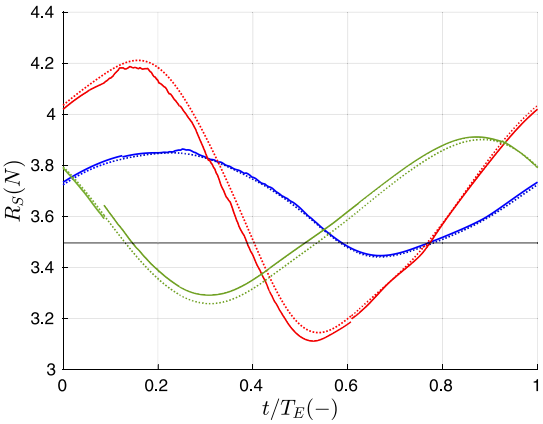

(j) Shear resistance component.

Fig. 29. (*continued*).

in waves are approximately −0.013 m/s, −0.027 m/s and −0.022 m/s for the shortest wave to the longest one, which is rather similar to the calm water value in terms of magnitude. In general, due to the contracting hull form in the aft, there is a velocity component towards the symmetry plane resulting in negative transversal component at the propeller disk. However, there is an induced transversal velocity caused by the bilge and shaft vortices. In waves, the hull motions and the orbital velocities of the waves add dynamics to the transversal velocity component. The contraction/expansion of the boundary layer in waves increases/decreases the transversal velocity at the propeller disk. Moreover, the dynamics of the bilge and shaft vortices in waves can alter the transversal velocity component. Although severe effects are seen from the higher harmonic amplitudes of $\tilde{v}$, especially in $\lambda/L = 1.1$ and 1.6, the variation of $\tilde{v}$ during T_E remains insignificant in terms of magnitude in comparison to the axial velocity component.

The surface-averaged vertical velocity component of the nominal wake at the propeller disk (reconstructed up to the 5th HC) is shown in Fig. 29(h). The MEAN value of $\tilde{w}$ in $\lambda/L = 0.6$, 1.1 and 1.6 are 0.033 m/s, 0.032 m/s and 0.027 m/s, respectively, which are close to the calm water value 0.021 m/s. The 1st harmonic amplitude is the dominant component in all three waves and the effects of higher harmonic amplitudes are less pronounced, but not negligible. The resultant maximum departure of $\tilde{w}$ from its mean value during one encounter period is large, especially in $\lambda/L = 1.1$ and 1.6, similar to the magnitudes of such variations for $\tilde{u}$. Although the trends of $\tilde{u}$ and $\tilde{w}$ during one encounter wave period are quite similar in $\lambda/L = 1.1$ and 1.6, such trend in $\lambda/L = 0.6$ is very different.

7.2.2. Contributing factors to transient wake

So far, the surface-averaged velocity components of the nominal wake at the propeller disk are studied for simulations in calm water and regular head waves in terms of harmonic amplitudes and time series during one encounter wave period, including brief discussions on the possible effects on the propeller performance considering resistance time series. In the following, first, the correlation of different contributing factors to the transient wake is examined, and then, the distribution of the transient wake over the propeller disk as well as the possible effects on the propulsive performance are investigated in detail. The investigations mainly concern the axial velocity component of the wake as the most important component with respect to the propulsion characteristics, while the transversal and vertical velocity components are also discussed briefly.

Overall, the variation of nominal wake in waves is a result of the interaction between the instantaneous propeller disk velocities, boundary layer contraction/expansion due to hull motions, bilge vortex and shaft vortex dynamics and the orbital wave velocities at the propeller disk. The effects of the instantaneous propeller disk velocities (caused by the hull motions) can be perceived by considering only the propeller disk in a uniform flow but superposing the hull motions in waves. The local flow velocity over the disk at each instance of time is identical to the instantaneous propeller disk velocity but in the opposite direction. It should be noticed that such effects are already included in the extracted wake velocities from the simulations in the presented results, however, the significance of such effects can be examined in an isolated condition disregarding its interactions with other contributing factors.

Since there is no motion in Y direction, there should be no effect on the transversal velocity component of the wake from the isolated

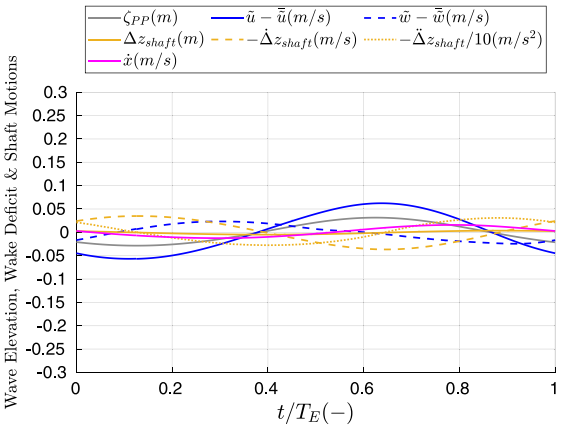

(a) $\lambda/L = 0.6$.

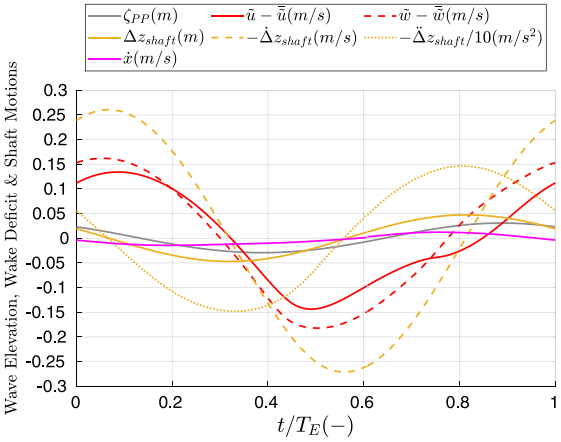

(b) $\lambda/L = 1.1$.

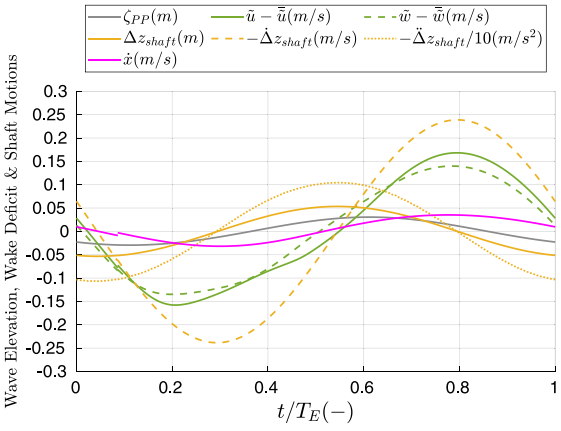

(c) $\lambda/L = 1.6$.

Fig. 30. Analytical wave at the initial position of propeller plane (PP), the variation of the shaft vertical position from its initial location and the variation of shaft vertical velocity and acceleration as well as the variation of the axial and vertical velocity component of the nominal wake from its mean value in the CFD simulations (grid $n = 1.00$) in regular head waves during the synced last encountered wave period of the simulations.

instantaneous propeller disk velocities. However, the axial and vertical velocity components are affected by different motions. The axial velocity component is affected by the surge and pitch, through the surge velocity $\dot{x}$, pitch velocity $\dot{\theta}$ component in the axial direction and the propeller disk rotation angle due to pitch motion. The vertical velocity component is affected by the heave and pitch, through the heave velocity $\dot{z}$, pitch velocity $\dot{\theta}$ component in the vertical direction and the propeller disk rotation angle due to pitch motion.

In order to simplify the problem, the pitch velocity component in the axial direction as well as the propeller disk rotation angle are deemed negligible. Therefore, it is assumed that the axial velocity component of the nominal wake is only affected by the surge velocity $\dot{x}$ while the vertical velocity component is affected by the vertical velocity of the shaft center $\dot{\Delta} z_{shaft}$. These components are shown in Fig. 30 for the synced last T_E time series. In this figure, for a better illustration, the MEAN values of the axial and vertical velocity components of the wake $\bar{\tilde{u}}$ and $\bar{\tilde{w}}$ are subtracted from $\tilde{u}$ and $\tilde{w}$. Moreover, the analytical wave elevation at the initial position of the propeller plane, and the shaft vertical departure from its initial location Δz_{shaft} as well as the vertical acceleration of the shaft $\ddot{\Delta} z_{shaft}$ during the synced last encountered wave period are also shown in Fig. 30.

The surge velocity $\dot{x}$ is the deviation of instantaneous ship forward velocity from the carriage velocity i.e., equal to the defined ship forward speed U. Although $\dot{x}$ varies during one encounter period, its MEAN value remains very close to zero, hence the MEAN instantaneous ship forward velocity remains very close to U. $\dot{x}$ is about 90 deg out of phase compared to the surge motion x. Therefore, the instantaneous ship forward velocity is also marginally affected by the spring, however, the contribution of variations in the spring natural frequency is assumed to be insignificant in the analysis of physical phenomenon related to the wake at the propeller plane, and only the synced last T_E time series are provided. Since the axial velocity of the wake is assumed to be positive from the fore ship towards the aft ship, $\tilde{u} - \bar{\tilde{u}}$ is correlated with $\dot{x}$. It can be seen in Fig. 30 that the effect of surge velocity on the axial velocity of the wake is not negligible. Therefore, the variation of wake during one encounter wave period might be considerably different between the fixed and free surge conditions. This reflects the importance of surge motion in the analysis of ships' nominal wakes.

Since the vertical wake velocity is assumed positive in the upward direction, $\tilde{w} - \bar{\tilde{w}}$ is correlated with $-\dot{\Delta} z_{shaft}$. In Fig. 30, a similar trend between $\tilde{w} - \bar{\tilde{w}}$ and $-\dot{\Delta} z_{shaft}$ is seen during one encounter wave period in $\lambda/L = 1.1$ and 1.6 and since the variation magnitude of $-\dot{\Delta} z_{shaft}$ is larger than that of $\tilde{w} - \bar{\tilde{w}}$, the effects of other contributing factors as well as the interactions between them are expected to be significant. On the other hand, such effects, except the orbital wave velocities, are less pronounced in $\lambda/L = 0.6$ and the nominal wake during one encounter wave period is found to be very close to the calm water wake. In this condition, the effects of wave orbital velocities can play a significant role as $\tilde{w} - \bar{\tilde{w}}$ approximately follows the trend of wave orbital velocities at the propeller disk, i.e., becomes zero close to the wave peak and wave trough and becomes maximum/minimum roughly at the zero down/up crossing of the wave elevation at propeller disk.

In the following section, the effects of different contributing factors on the transient wake are examined for each wave length, taking into account the ship motions as well as the shaft vertical motions during the synced last encountered wave period.

In $\lambda/L = 0.6$, the 1st harmonic amplitude of axial velocity component $\tilde{u}$ is the dominant harmonic component, as seen in Fig. 21, however, it is relatively lower than the other two wave lengths, hence the wake has weak dynamics and is more similar to the calm water wake. The maximum of $\tilde{u}$ in $\lambda/L = 0.6$ occurs at $t/T_E \approx 0.6$ in which the pitch motion value is just departing its minimum and the heave is approaching its maximum. However, since these motions are very small, the variation of the shaft vertical position in Fig. 30(a) remains negligible in this wave length. On the other hand, the maximum of the wake approximately coincides with the wave peak at the propeller plane ζ_{PP} and the trend of ζ_{PP} and $\tilde{u} - \bar{\tilde{u}}$ time series are very similar during one wave encounter period ($t/T_E = 0$ to 1). Therefore, the wake in $\lambda/L = 0.6$ is mainly affected by the wave orbital velocities, which is also confirmed by the variations of $\tilde{w} - \bar{\tilde{w}}$.

In $\lambda/L = 1.1$, the effects of the higher harmonic amplitudes of the surface-averaged velocity components at the propeller disk are more pronounced, especially in $0.5 < t/T_E < 0.9$. The maximum of $\tilde{u}$ occurs at $t/T_E \approx 0.1$ in which the heave is approximately at its minimum and increasing and the pitch is decreasing (i.e., stern moving downwards). The effects of heave and pitch motions on the shaft's vertical position can be seen in Fig. 30(b). The maximum of $\tilde{u}$ occurs when the shaft is almost at its original vertical position but moving downwards and the analytical free surface elevation at the propeller plane is approaching the still water level from the wave crest. The minimum of $\tilde{u}$ in $\lambda/L = 1.1$ occurs at $t/T_E \approx 0.5$ in which pitch increases from its minimum value towards positive values (i.e., the stern is moving upwards) and the heave increases and moves towards its maximum value. When $\tilde{u}$ is at its minimum, the shaft is located lower than its original position while moving upward. At this stage, the wave trough has just been traversed and the free surface elevation is moving towards still water level. Insignificant effects are expected from $\dot{x}$ in this wave length.

In $\lambda/L = 1.6$, the effects of the higher harmonic amplitudes of the surface-averaged velocity components at the propeller disk are mainly seen in $0.2 < t/T_E < 0.6$. The maximum of $\tilde{u}$ occurs at $t/T_E \approx 0.8$ in which heave motion is approximately at its minimum and the pitch motion departs approximately from high values and stern moves downward. In other words, the maximum of $\tilde{u}$ is occurring when the shaft is located at its original position and moving downwards, while the analytical free surface elevation at the propeller plane is approaching the still water level from the wave crest, see Fig. 30(c). The minimum of $\tilde{u}$ in $\lambda/L = 1.6$ occurs at $t/T_E \approx 0.2$ in which pitch just departs its minimum (the stern moves upwards from its deepest submerged state) and the heave motion approaches its maximum. When $\tilde{u}$ is at its minimum, the shaft is located lower than its original position and moves upward, while the wave trough has just traversed and the free surface elevation approaches still water level. Significant effects are expected from instantaneous surge velocity due to the large magnitude of $\dot{x}$ in this wave length which coincided with the variation of $\tilde{u}$.

It is very interesting that the maximum and minimum conditions for $\tilde{u}$ are precisely similar in $\lambda/L = 1.1$ and 1.6. Moreover, in both of these wave lengths, the time t/T_E it takes from the maximum of $\tilde{u}$ to the minimum of $\tilde{u}$ is similar and it is shorter ($\approx 0.4T_E$) than the time it takes from minimum to maximum ($\approx 0.6T_E$). Moreover, the effects of higher harmonic amplitudes are more pronounced during the time from minimum $\tilde{u}$ to approximately MEAN $\tilde{u}$. However, in $\lambda/L = 0.6$ the time between maximum and minimum are almost equal ($\approx 0.5T_E$). In Fig. 31 the vortical structures found by the same Q-criterion, i.e., similar to the calm water case in Fig. 11, as well as the nominal wake at hull-fixed propeller disk approximately at the maximum and minimum $\tilde{u}$ time instances are shown.

In $\lambda/L = 0.6$, due to small ship motions, the contribution from the instantaneous surge velocity, the boundary layer development as well as the shaft and bilge vortices dynamics are found to be negligible and the wake is found to be mainly affected by the wave orbital velocities. This can also be observed in Figs. 31(a) and 31(d). On the other hand, in $\lambda/L = 1.1$ and 1.6, large amplitude ship motions affect the formation of the boundary layer as well as the dynamics of the vortical structures. Therefore, the maximum of $\tilde{u}$ approximately coincides with the contracted boundary layer. The contraction of the boundary layer occurs when the aft ship moves downward, as a result of combined heave and pitch motions, which consequently results in an upward-moving flow around the aft bilge and thus formation of a strong bilge vortex close to the bilge but swipes away the weakened shaft and bilge vortices at the propeller disk, see Figs. 31(b) and 31(c). At this time, the shaft is moving downward from almost its original position and the bilge vortex disperses and moves almost out of the propeller disk while the weakened shaft vortex at the propeller disk is located above the shaft and the area below the shaft is mainly a high velocity area. Since the maximum of $\tilde{u}$ occurs when the wave elevation is close to the still water surface, then there is probably no significant effect from the wave orbital velocities. The contribution of $\dot{x}$ is expected to be more pronounced in $\lambda/L = 1.6$ which may justify the large variation of $\tilde{u}$.

The minimum of $\tilde{u}$ in $\lambda/L = 1.1$ and 1.6 occurs when the shaft is located lower than its original position and moving upward while the propeller disk faces the expanded boundary layer. At this stage, bilge vortices hit the propeller plane and play a significant role in the dynamics of the wake at the propeller disk, as shown in Figs. 31(e) and 31(f). A strong shaft vortex in the minimum wake state is located under the shaft which leads to a large low-speed area in this region. As the minimum wake state occurs at the time in which the wave elevation is between the wave trough and still water surface (approaching the still water level), then there might be a slight effect from the orbital velocities of the wave which might explain the earlier minimum condition in these wave lengths.

The impact of the higher harmonic amplitudes of the axial wake in $\lambda/L = 1.1$ and 1.6 occurs during the time in which the shaft is almost at its original position and moving upward, i.e., shortly after the minimum $\tilde{u}$. At this time, mainly the generated strong shaft vortex, and to some extent the bilge vortex, at the time of minimum $\tilde{u}$ lag behind, and they remain outside of the propeller disk. This, together with the possible effects from the wave orbital velocities and the surge velocity as well as the complex interactions between them may be the main reason for observing such higher harmonics effects.

7.2.3. Time-averaged wake

The nominal wake velocity components are monitored on the propeller disk during the last encountered wave period in the regular head wave simulations with the grid $n = 1.00$ and then time-averaged over T_E in each wave length. The results are shown as contour plots in Fig. 32. Thereafter, the calm water nominal wake on the propeller disk in the last time step of simulations for the grid $n = 1.00$, shown in Fig. 15(b), is subtracted from such time-averaged contour plots in waves and the results are shown in Figs. 32(b), 32(d) and 32(f).

The nominal wake in waves is affected by the hull motions and the wave orbital velocities leading to different flow dynamics in comparison to calm water conditions. As presented earlier, the wake becomes fuller in waves in comparison to calm water which can also be seen in Fig. 32, especially in $\lambda/L = 1.1$ and 1.6 where the hull motions are larger. The time-averaged nominal wake distribution in $\lambda/L = 0.6$ is the closest to the calm water nominal wake, simply because the wave-induced motions are the smallest in this wave relative to the other studied waves. The nominal wake in this wave length is mainly affected by the wave orbital velocities. However, in $\lambda/L = 1.1$ and 1.6, the motions become significantly large which in turn alter the formation of the boundary layer and bilge vortex dynamics.

Generally, the bilge vortex tends to move low-speed flow from the inner part of the boundary layer outward, and inward further up, (Larsson and Raven, 2010). This creates a hook shape in the velocity contour at the propeller disk in calm water. The bilge vortex is less dynamic in calm water relative to waves. As a result, it stays within a certain range close to the hull. Therefore, in a certain time interval, its effect is concentrated in a limited region. However, the bilge vortex continuously moves up and down in waves, and sometimes even moves out of the propeller disk. Consequently, the interaction effect of the bilge vortex and the boundary layer will be less concentrated and thus its capability of moving the low-speed flow close to the propeller center will be weakened. This results in a fuller nominal wake in waves relative to calm water.

Here, the motions in $\lambda/L = 1.1$ and 1.6 are severe and thus the averaged nominal wakes are fuller than that of the shortest wave. Although the variation of Δz_{shaft} during one encounter period is very similar in $\lambda/L = 1.1$ and 1.6, the wake in $\lambda/L = 1.1$ is slightly fuller, which is also seen in Fig. 21. The magnitudes of the maximum and minimum values of the shaft vertical velocity $-\dot{\Delta} z_{shaft}$ are similar in $\lambda/L = 1.1$ and 1.6, see Fig. 30. However, since the wave encounter period is smaller in $\lambda/L = 1.1$, the magnitudes of the maximum and minimum values of the

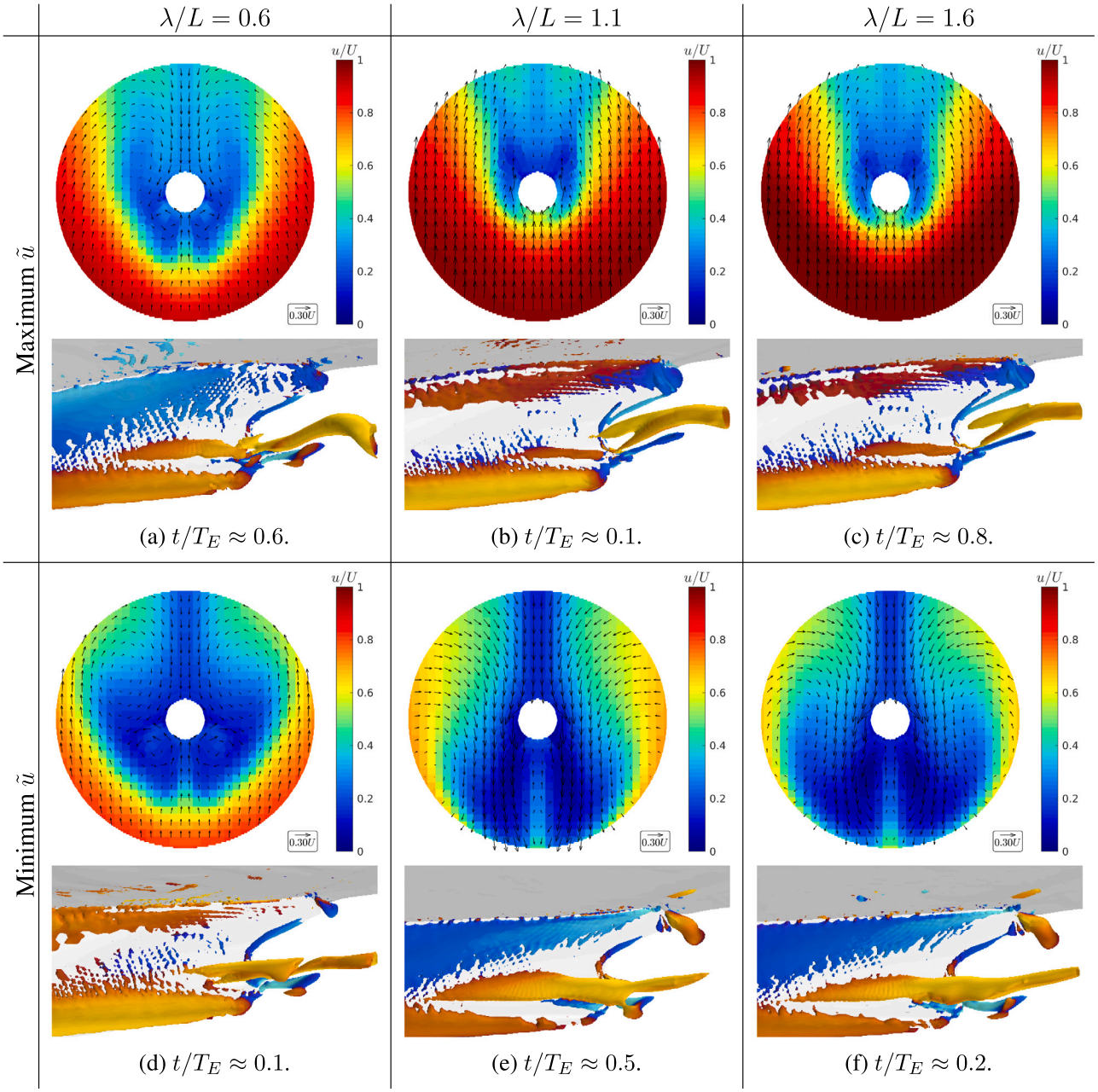

Fig. 31. CFD wake on the hull-fixed propeller disk and the vortical structures (colored by normalized helicity provided in Fig. 11) found by Q-criterion = 10 $/s^2$ at the approximately maximum and minimum time instances of $\tilde{u}$ in regular head wave simulations.

shaft vertical acceleration $-\ddot{\Delta}z_{shaft}$ in this wave length are larger than the values in $\lambda/L = 1.6$. Larger shaft/stern vertical accelerations result in larger bilge vortex dynamics. Consequently, the time in which the bilge vortex remains outside of the propeller disk is longer in $\lambda/L = 1.1$, resulting in a fuller wake in comparison to $\lambda/L = 1.6$. The contour plots of the time-averaged wake difference between the waves and the calm water conditions show the regions with velocity deficit and excess in waves relative to calm water. Such deficit and excess for the axial, transversal and vertical velocity components in $\lambda/L = 1.1$ and 1.6 pinpoints missing bilge vortex and the shaft vortex in comparison to the calm water wake. Since a propeller is often designed based on the calm water nominal wake, any deviation from the calm water wake alters the loading distribution on the blade resulting in an adverse effect on the propeller performance.

7.2.4. Harmonic amplitudes of wake

In order to further analyze the variation of wake in waves, the axial velocity of the wake for each extracted data point (computational cell) on the hull-fixed propeller plane (HF_{PP}) is monitored during the last encountered wave in the simulations and then the Fourier analysis is performed on $1T_E$ time window for each point separately. Thereafter, the 1st, 2nd and 3rd harmonic amplitudes are plotted for each point resulting in contour plots shown in Fig. 33. Since a hull-fixed plane is considered, the propeller disk is represented by a dashed circle in this figure. Having different harmonic amplitudes and harmonic phases of the wake in every extracted data point on the propeller plane also provides an opportunity to reconstruct the wake with different time resolutions as well as using different harmonic components.

In $\lambda/L = 0.6$, the harmonic amplitudes are very small which may be related to the insignificant shaft vertical position variation and vortices dynamics seen in this wave length. The highest values for all

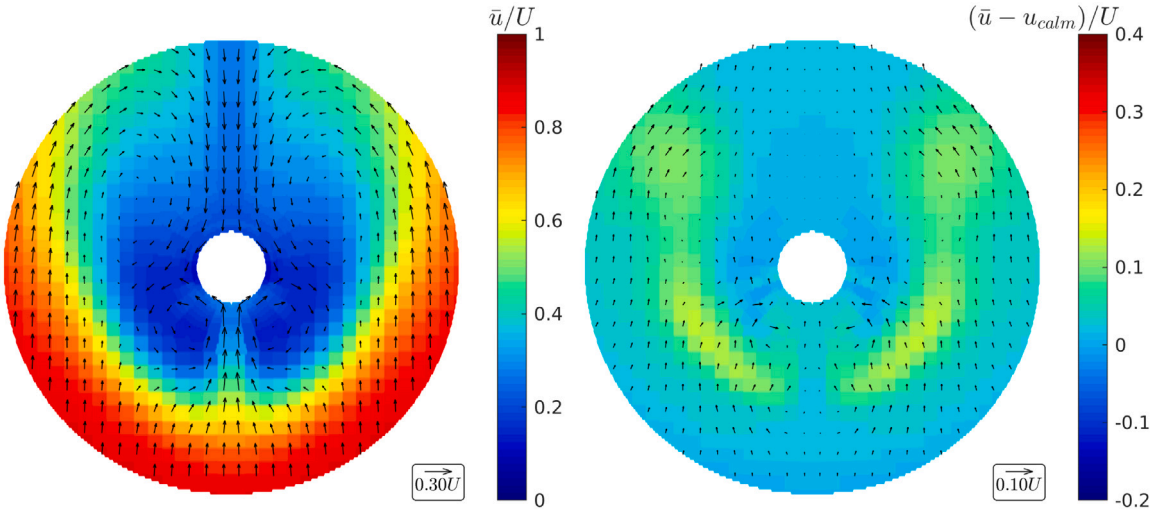

(a) $\lambda/L = 0.6$, time-averaged over T_E.

(b) $\lambda/L = 0.6$, time-averaged over T_E minus calm.

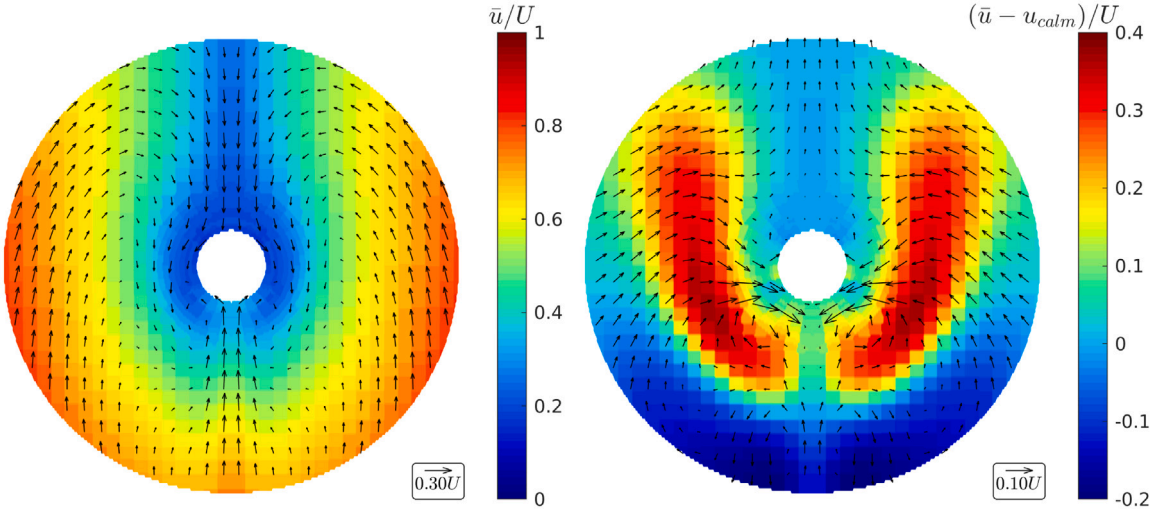

(c) $\lambda/L = 1.1$, time-averaged over T_E.

(d) $\lambda/L = 1.1$, time-averaged over T_E minus calm.

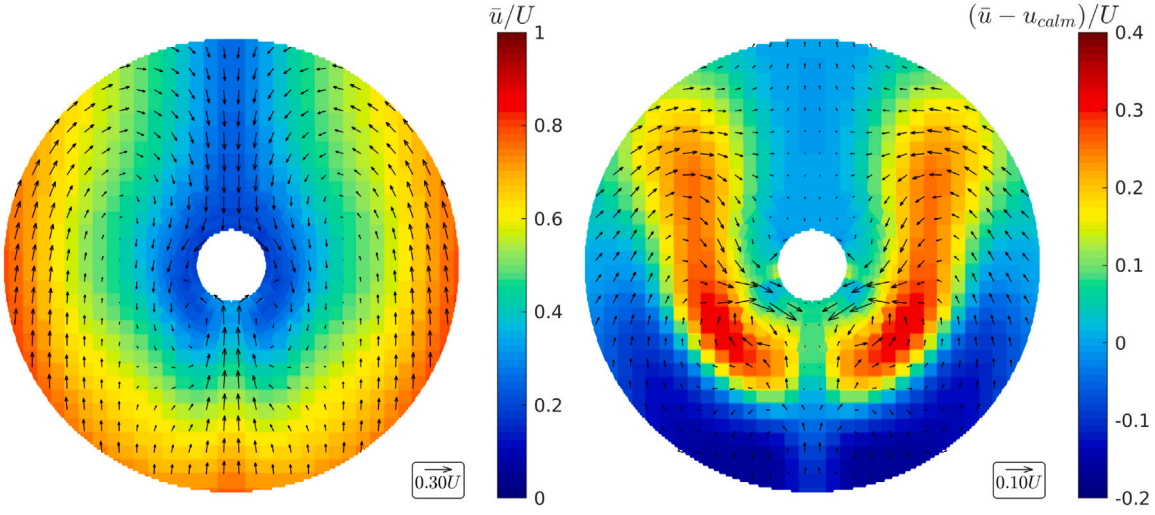

(e) $\lambda/L = 1.6$, time-averaged over T_E.

(f) $\lambda/L = 1.6$, time-averaged over T_E minus calm.

Fig. 32. Time-averaged CFD wake over the last encountered wave period T_E in the regular head wave simulations on the hull-fixed propeller disk as well as the same averaged wake mines calm water wake at the last time step in free surge calm water simulations, all for grid $n = 1.00$.

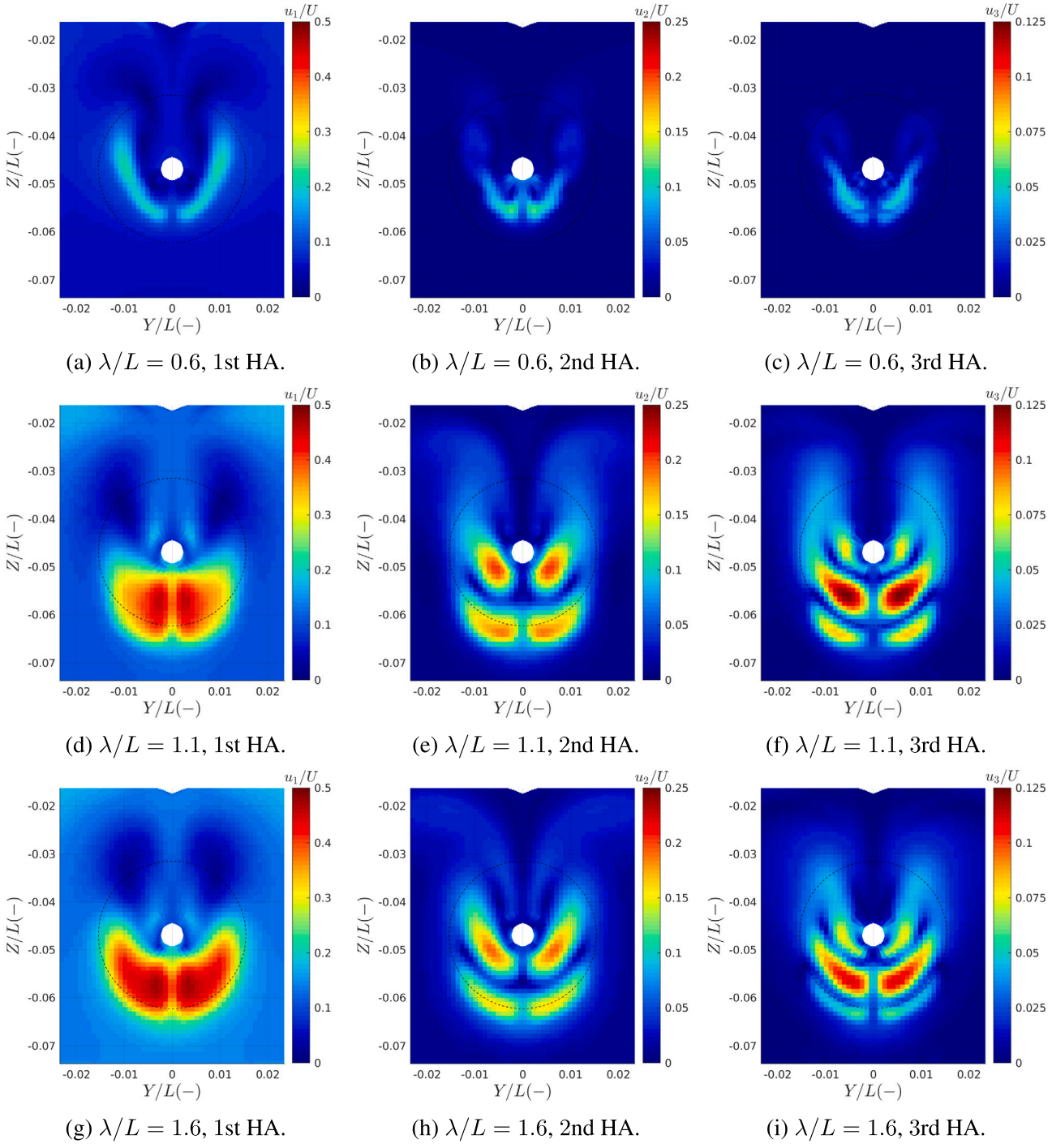

Fig. 33. FFT results of the axial velocity component of the CFD wake in regular head waves on the hull-fixed propeller plane in HF_{PP}.

three harmonic amplitudes are almost occurring in the same regions with respect to the propeller center. On the other hand, the harmonic amplitudes are rather large in $\lambda/L = 1.1$ and 1.6 and the large values of the 1st, 2nd and 3rd harmonic amplitudes of the axial velocity of the wake (u_1, u_2 and u_3) are seen mainly in the lower part of the propeller disk. As the harmonic amplitude of the axial wake increases, the number of islands associated with wake oscillations increases but at the same time, the oscillations become weaker and more confined.

A point with a high value of the harmonic amplitude experience a larger variation of the axial wake from its mean value during T_E. For instance, at the point where u_1/U is 0.5 and all other harmonic amplitudes are zero, u/U varies once between $\bar{u}-0.5$ and $\bar{u}+0.5$ during $1T_E$. This variation is occurring twice and three times during $1T_E$ for the 2nd and 3rd harmonic amplitudes, respectively. However, the phases of variations are not identical all over the propeller plane. Therefore, the wake at a certain location and time can reach its maximum value which is not necessarily the case elsewhere.

In order to understand the time differences of wake variations between different cells, the harmonic phases contour plots should also be shown. Nevertheless, such details are out of the scope of the current investigations and it is just enough to point out that such phases for the cells in each high-value region are almost similar meaning that the axial velocity of the wake varies smoothly in those regions. Since the high-value regions occur mainly in the lower part of the propeller disk,

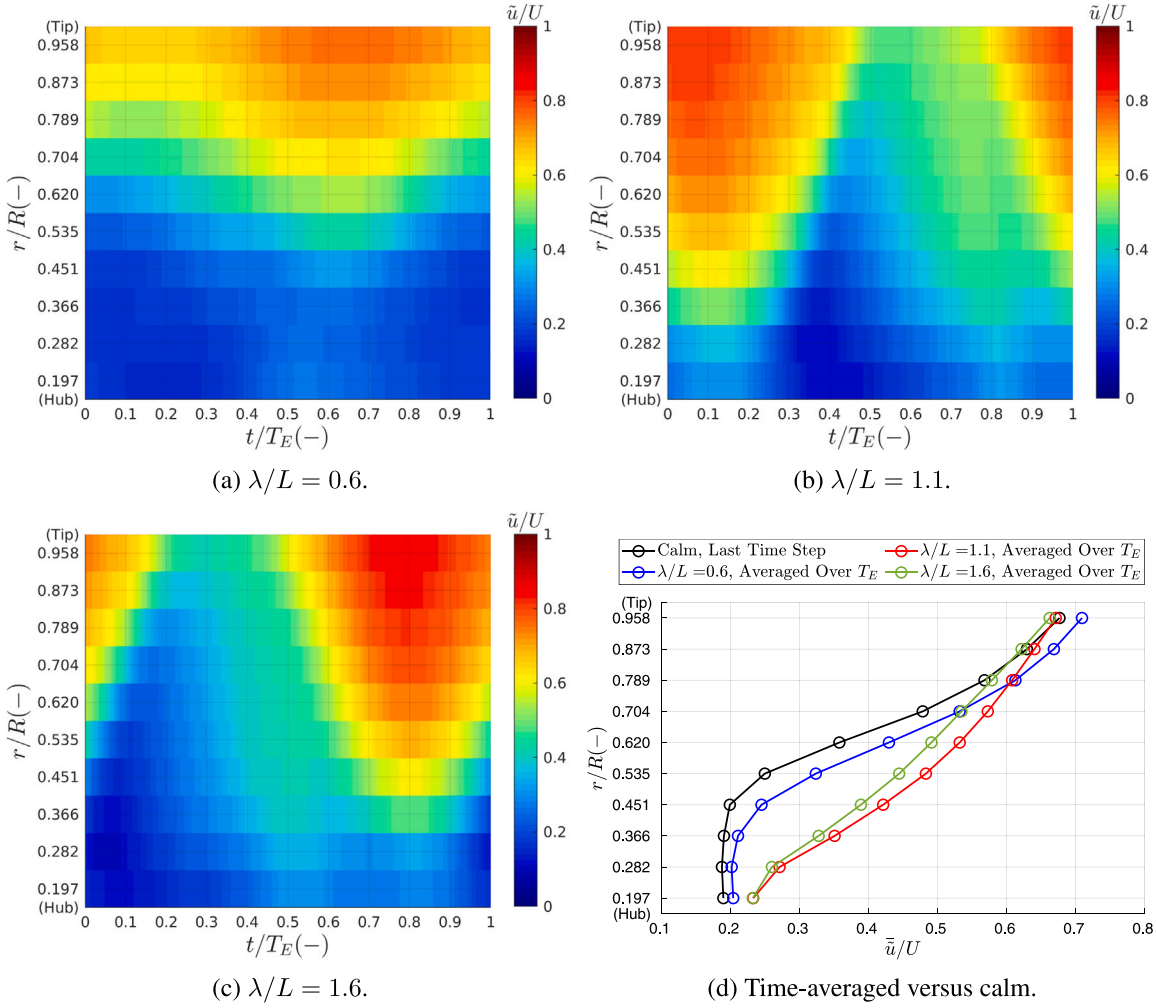

Fig. 34. Circumferential-averaged axial velocity component of wake on the hull-fixed propeller disk in the last time step of simulation in calm water and in the last encountered wave in the regular head waves simulations, all for grid $n = 1.00$.

the propeller blades that pass those regions experience large variations during one encounter period.

7.2.5. Circumferential-averaged wake

In Fig. 34, the circumferential-averaged axial velocity component of the nominal wake in the last encountered wave of the regular wave simulations is compared to that of calm water in the last time step of the simulation. Similar plots for the transversal and vertical velocity components are also provided in Figs. 35 and 36.

The variation of the circumferential-averaged axial velocity in the last encountered wave period in the regular head waves simulations is shown in Figs. 34(a)–34(c) for $\lambda/L = 0.6$, 1.1 and 1.6, respectively. These contour plots indicate that the wake significantly varies in time, especially in $\lambda/L = 1.1$ and 1.6 where the motions are large. This means that the blade loading while operating in this wake will change significantly in each time incident during one encounter period. However, it should be kept in mind that a time-averaged of the circumferential-averaged wake, shown in Fig. 34(d), is a more relevant way of extracting the nominal wake for designing a wake adapted propeller blade for each wave length. Nevertheless, it should not be forgotten that the transient wake and thus propeller load variation in one encounter period should also be studied to avoid any design failure in any of the circumferential transient nominal wake distributions.

The curves shown in Fig. 34(d) represent the average flow that each propeller blade section encounters in one full revolution. The radial distribution of the axial component in $\lambda/L = 0.6$ is rather similar to that of calm water, however, in $\lambda/L = 1.1$ and 1.6 the radial distribution of the axial velocity is considerably different than the calm water curve, especially between $0.282 < r/R < 0.704$, in which a large part of the propeller thrust is often generated. Although the time-averaged values near the propeller tip remain similar to calm water, the severe variation of the axial velocity component near the propeller tip in the wave can have significant effects on the formation of tip vortex and propeller cavitation pattern close to this region.

For the transversal velocity component, the variations of the circumferential-averaged wake during one encounter wave period at each radius are rather insignificant. Although the distribution of the time-averaged values in waves is different from the calm water, especially in $\lambda/L = 1.1$ and 1.6, the differences in terms of magnitude are insignificant.

The vertical velocity components exhibit significant variation in the circumferential-averaged wake during one encounter wave period at each radius. However, the radial distribution of the time-averaged values in waves is very close to that of calm water. One interesting aspect regarding the vertical velocity component in $\lambda/L = 1.1$ and 1.6 is the consistent impact across all radii throughout t/T_E. This uniform impact can potentially be attributed to the vertical velocity of the shaft, meaning that the whole propeller disk roughly experiences a similar effect.

Large variations of the circumferential-averaged axial and vertical velocity components during one encounter period, especially near the propeller tip, may significantly affect the angle of attack and hence the

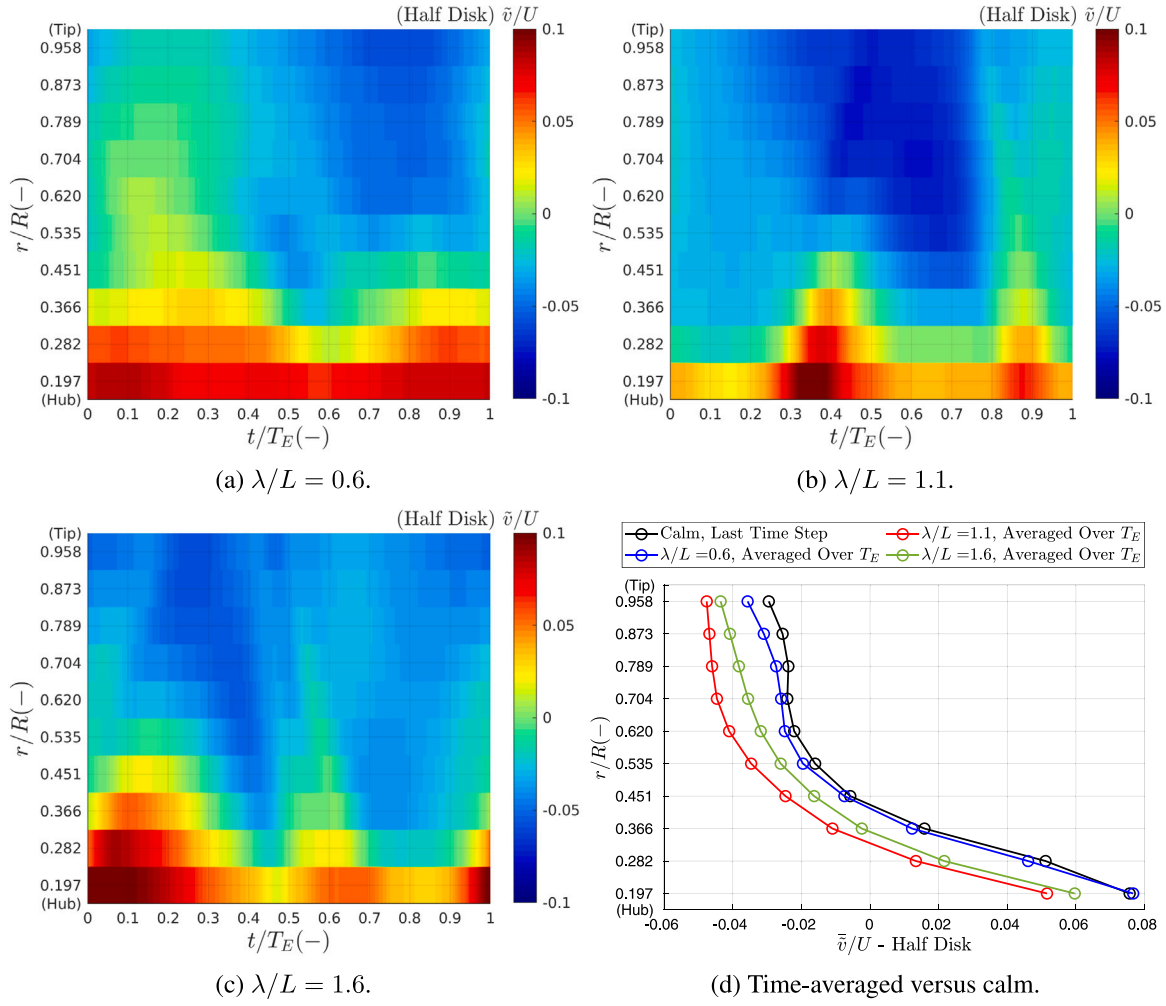

Fig. 35. Circumferential-averaged transversal velocity component of wake on the hull-fixed propeller disk (half of the disk) in the last time step of simulation in calm water and in the last encountered wave in the regular head waves simulations, all for grid $n = 1.00$.

cavitation patterns on the blades. Such information can also be used by propeller designers to reduce propeller noise and nuisance. Moreover, detailed information about the non-axial velocity components may be crucial for designing Energy Saving Devices (ESDs).

7.3. Computational costs

As the final step of the evaluations, the computational costs in terms of *Core-Hours* for the simulations in calm water and regular head waves are shown in Fig. 37. The computational costs are presented as *Core-Hours* per 1 s of physical time simulation. Therefore, the simulation of one encounter wave period demands more computational resources in the longer waves than the shorter ones, because T_E is larger for the longer waves.

One important point to note is that the computational costs in calm water and regular head waves in terms of the simulation of 1 s physical time for the same grid are almost similar because the same models and grid discretization are used for the simulation of these two conditions. Nonetheless, for different simulations, different computing resources (clusters) with different configurations were employed, hence there is an inconsistency (bias) in the direct comparison of the computational costs in different operational conditions. Furthermore, for parallel computations, approximately between 50 000 to 90 000 cells are allocated to each core in different simulations, except for the grid $n = 1.00$ in $\lambda/L = 0.6$ where much less number of cells ($\approx$ 30 000) are allocated to each core. It can be seen that the efficiency of such computations is dropped which is resulted in higher computational costs. The efficiency of the computations is also the reason behind the differences between the simulations in the grid $n = 2.00$ in calm water and waves. Even though a direct comparison may not be reliable, the computational costs presented in Fig. 37 can still offer valuable insights for an overall comparison in different conditions.

It should be noted that each simulation runs for a different total physical time in order to achieve convergence and define the proper time window for post-processing the results. Therefore, the computational costs presented in Fig. 37 do not reflect the entire computational power used for running simulations. A very rough estimation of the total computational costs used for the simulations in calm water and in regular head waves of $\lambda/L = 1.1$ both with grid $n = 1.00$ implies running on 128 cores (CPUs) for 7 days and 8 days, respectively.

8. Conclusions

In this paper, the hydrodynamic performance of the KVLCC2 bare hull was investigated by using a Reynolds-Averaged Navier–Stokes (RANS) solver to analyze the ship resistance, motions and nominal wake. The simulations were carried out in four operational conditions all at the design speed and in the design loading condition while being free to surge, heave and pitch (3DOF): one in calm water and three in regular head waves with the same wave height and three different wave lengths $\lambda/L = 0.6$, 1.1 and 1.6. The convergence of simulations was examined based on different criteria defined on the ship resistance

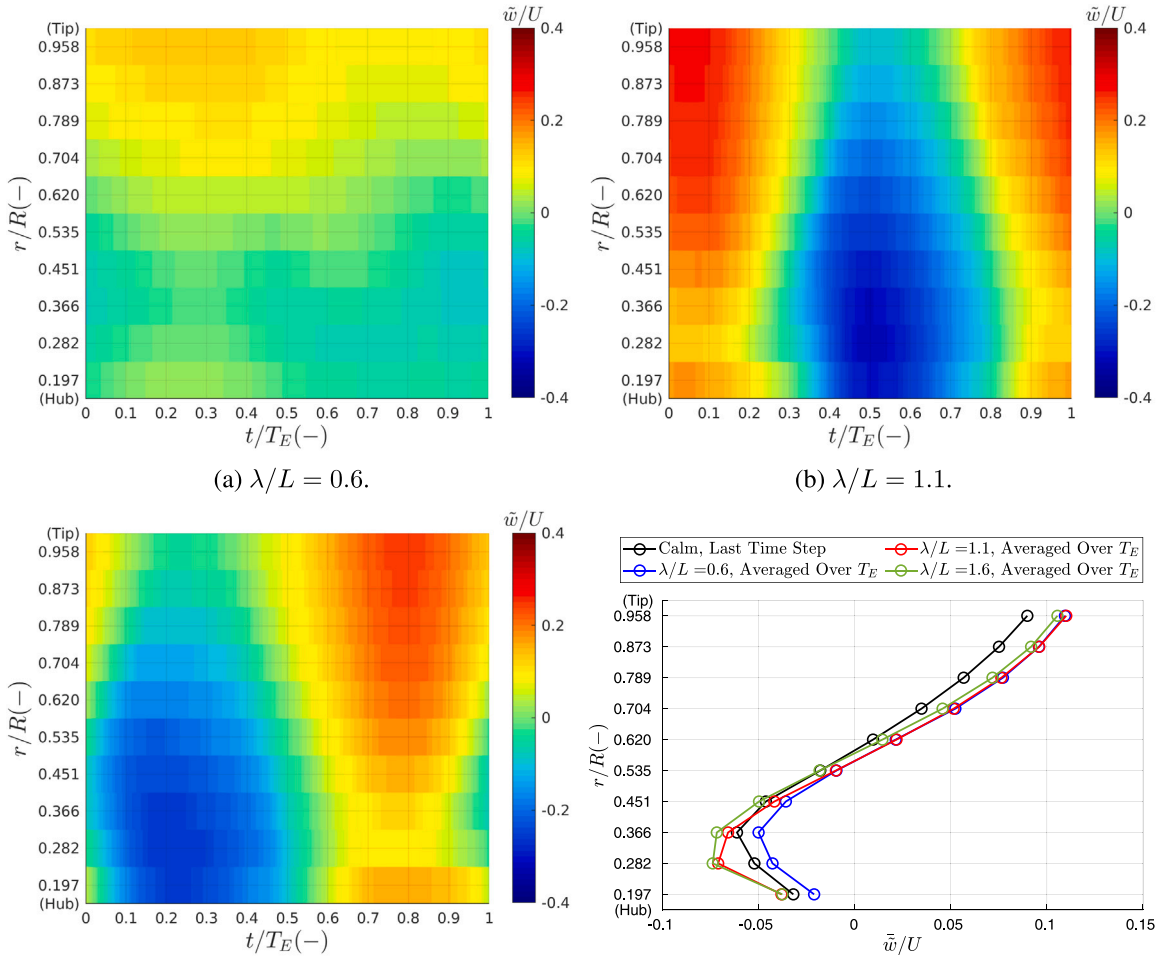

(a) $\lambda/L = 0.6$. (b) $\lambda/L = 1.1$.

(c) $\lambda/L = 1.6$. (d) Time-averaged versus calm.

Fig. 36. Circumferential-averaged vertical velocity component of wake on the hull-fixed propeller disk in the last time step of simulation in calm water and in the last encountered wave in the regular head waves simulations, all for grid $n = 1.00$.

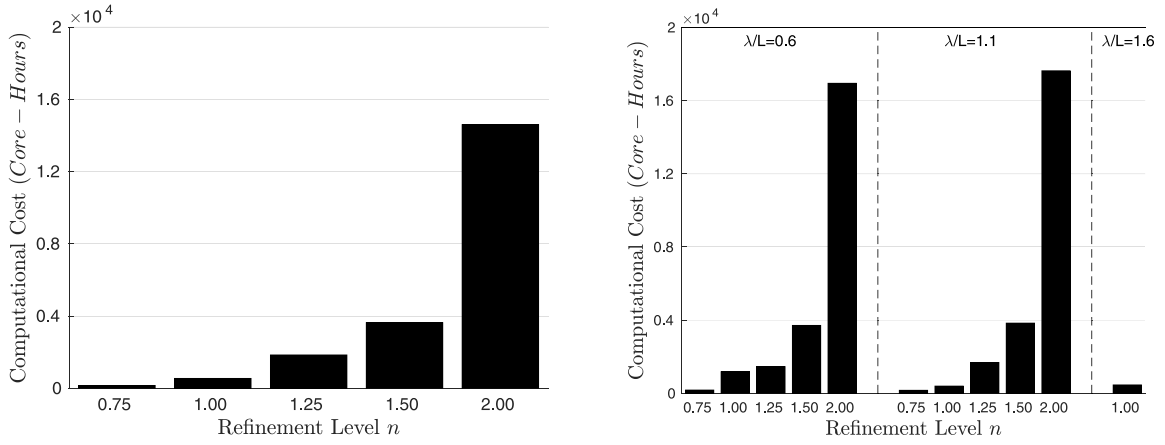

(a) Computational costs in calm water simulation. (b) Computational costs in regular wave simulation.

Fig. 37. Computational costs for 1 s of physical time simulations in calm water and in regular head waves.

in each operational condition using a carefully defined time window for the post-processing of the results.

A formal verification and validation (V&V) procedure was applied to understand and control the numerical and modeling errors in the conducted RANS computations. The verification analysis concerned the grid convergence study using the tool developed by Eça and Hoekstra (2014) based on the Least Squares fits to power series expansions. The simulations were carried out for up to five "as geometrically similar as possible" unstructured grids defined by refinement levels $n = 0.75$, 1.00, 1.25, 1.50 and 2.00.

The experimental data (EFD) were obtained from the model tests carried out in Osaka University Towing Tank mainly in free surge conditions (3DOF) using a very weak spring system. An external force F_0 was applied in each operational condition to restrict large compression/expansion of the spring. The CFD wake at different planes was compared to that of experimental SPIV measurements. However, due to several potential sources of discrepancy between CFD and EFD data, only qualitative comparisons were carried out.

EFD wake measurements were carried out on two planes that were fixed on the carriage. Since F_0 was not known from the experiments, a presumed value was used in the CFD simulations. The difference between such external forces could change the spring behavior resulting in an inconsistency of surge motion between CFD and EFD. As the plane of wake measurements was carriage-fixed, the difference in surge would affect the longitudinal position of the plane with respect to the hull, hence introducing a separate source of discrepancy in the wake comparison. Another potential source of discrepancy was the exact time instances of SPIV measurements in regular head waves as different setups were used to trigger the EFD wake measurements. Based on the analysis performed in this paper, such setups could significantly affect the time instances for the wake measurements. Moreover, the measured wave height in EFD data in some operational conditions was notably different from the target value, therefore, the response of the ship could have been affected, hence adding another source of discrepancy to the wake comparisons. Despite the aforementioned potential sources of discrepancy, the CFD wake reasonably matched the EFD SPIV measurements.

Calm Water — V&V

The calm water simulations were carried out in all five grid refinement levels. Although the grid convergence study for the calm water resistance showed rather large numerical uncertainties (8.8% to 14.9%), the computed resistance from different grids were similar in terms of magnitude. It was suggested that a linear curve fitting could have been a more practical alternative than the second-order method in the employed verification tool. The computed resistance and motions in calm water were in rather good agreement with the measured data, especially when the discrepancies were compared in terms of magnitude with respect to the accuracy of the computations and measurements.

For the axial velocity component of the nominal wake on the hull-fixed propeller disk $\bar{\bar{u}}$ in calm water, the numerical uncertainties were higher (18.1% to 31.0%) than those of resistance. Contrary to the motions and resistance, significant differences of $\bar{\bar{u}}$ were seen between different grids, which in conjunction with the high uncertainties, indicated the importance of grid refinement for the wake predictions. Moreover, significant differences in the magnitude and profile of the circumferential-averaged axial wake were observed between different grids, especially in the radius of $0.6 < r/R < 0.8$ where often a substantial part of the propeller thrust is generated. Therefore, significantly different wake-adapted propeller designs can be proposed depending on the choice of the grid in calm water.

Regular Head Waves — V&V

In regular head waves, all five grid refinement levels were used for the simulations in $\lambda/L = 0.6$ and 1.1 and the grid convergence studies were carried out in these wave lengths. However, only one grid $n = 1.00$ was used for the simulations in $\lambda/L = 1.6$. An insignificant spectral leakage was obtained in the performed Fourier analyses over the defined post-processing time windows, as different time series were, to a very high extent, a harmonic function of the wave encounter frequency in each wave condition. The numerical uncertainties for the 1st harmonic amplitudes of the heave and pitch motions were relatively lower (0.7% to 8.2%) than the numerical uncertainties of the mean total resistance (6.6% to 11.1%). However, since the results of different grids were very similar in terms of magnitude, a linear line might be a better candidate for curve fitting for these quantities, similar to the calm water resistance.

The overall results of the simulations in regular head waves were in good agreement with the experimental data for ship resistance and motions. The largest validation errors were justified by addressing the differences in terms of magnitude and taking into account the possible uncertainties involved in the EFD data as well as considering the actual measured wave height in the model tests by studying the non-dimensional quantities in conjunction with the dimensional ones.

The averaged absolute error $\overline{|E\%D|}$, computed from averaging the absolute errors of the mean total resistance and the 1st harmonic amplitudes of surge, heave and pitch motions, for the simulations in $\lambda/L = 1.1$ and 1.6 with the grid $n = 1.00$ were reduced for the non-dimensional quantities in comparison to the dimensional ones. Averaging $\overline{|E\%D|}$ in $\lambda/L = 1.1$ and 1.6 in EFD_1 and EFD_2 gave approximately 10.4% validation error in dimensional quantities but 7.4% error in the non-dimensional ones. However, for the shortest wave $\lambda/L = 0.6$ these errors were mainly increased from 8.3% to 12.4%. Firstly, in this wave length, the magnitudes of the 1st harmonic amplitudes of motions were extremely small and close to zero, hence small discrepancies resulted in large errors and the uncertainty of measurements became essential. Secondly, the validation errors for the dimensional mean total resistance and the 1st harmonic amplitudes of motions were already negligible in terms of magnitude. Last but not least, the non-dimensionalization using the wave amplitude in such a short wave might be questionable.

In regular head waves, the numerical uncertainties of the mean axial velocity of wake were relatively higher (4.9% to 32.1%) than that of mean total resistance and the 1st harmonic amplitudes of motions, similar to the calm water condition. One important conclusion from the verification analyses in calm water and regular head waves was that the numerical uncertainties as well as the discrepancies between different grids in terms of magnitude for resistance and motions were relatively lower than those of the axial velocity of the nominal wake. This means although rather reliable resistance and motion predictions could be derived from the coarser grids, the nominal wake predictions were significantly dependent on the choice of the grid. This dependency was stronger in calm water and the shortest wave $\lambda/L = 0.6$, in which the hull motions and hence bilge vortex dynamics were insignificant and the numerical uncertainties were mainly imposed by the accuracy of the predicted flow-driven phenomena such as the budging bilge vortex. On the other hand, the grid refinement dependencies and numerical uncertainties were lower for the longer waves in which significant vortex dynamics were observed due to the large hull motions and the accuracy of the predicted wake was mainly governed by the ship dynamics.

Hydrodynamic Performance — Resistance and Motions

After the verification and validation studies, the hydrodynamic performance of the ship was compared in different operational conditions using the calm water results and the reconstructed time series as well as the time series of the last encountered wave period in the regular head wave simulations. It was found that the higher harmonic amplitudes, e.g., up to the 5th harmonic amplitude in the longer waves, were playing a significant role in the resistance and nominal wake velocities, while only the 1st harmonic amplitudes were significant for the motions.

Although the behavior of heave and pitch motions during one encounter period was completely different in different wave lengths, the behavior of total resistance was roughly similar for all three waves, with minimum/maximum values occurring approximately when the wave trough/crest is close to the ship fore perpendicular. Larger variations were seen for the total resistance during one encounter period in $\lambda/L = 0.6$ and 1.6 in comparison to $\lambda/L = 1.1$, while the mean total resistance was higher in $\lambda/L = 1.1$ mainly due to the effects of higher harmonic amplitudes in this wave length. Therefore, a self-propelled hull in $\lambda/L = 1.1$ has to deliver a larger averaged thrust in comparison to the other wave lengths, but the load variation and consequently the maximum and minimum loading conditions on the propeller will be more severe in the shorter and longer wave lengths. Such load variations can impose several design constraints both for the propeller and also the machinery system.

The contribution of the added shear resistance on the total added resistance of the hull was 6.8%, 2.9% and 4.6% for the shortest wave to the longest one in grid $n = 1.00$, which was relatively small but not negligible. Moreover, it was found that the time-averaged wetted surface area in waves was almost equal to that of calm water. Therefore, it is concluded that the viscous phenomena such as increased turbulence by the wave orbital velocities contribute to the increased frictional resistance in waves relative to calm water. Consequently, the conventional frictional resistance prediction methods, such as the ITTC-57 model-ship correlation line, cannot be directly used for the frictional resistance prediction in waves.

Hydrodynamic Performance — Nominal Wake

During one encountered wave period in regular head waves, quite significant variations were seen for the axial velocity component of the wake and the time-averaged values in all three waves were larger (approximately 9.8%, 21.3% and 14.6% for $\lambda/L = 0.6$, 1.1 and 1.6, respectively) than the calm water value. The variations in the transversal velocity components remained insignificant in terms of magnitude in comparison to the axial component. However, large variations were seen for the vertical velocity component, similar to the axial component. The trend of the wake velocities during one encounter wave period was different in different wave lengths, while the resistance trends were rather similar. Therefore, the expected propeller thrust in self-propulsion undergoes different alterations over time than the required thrust to overcome the resistance in different wave lengths, which may give rise to significant propeller design constraints.

Overall, the variation of nominal wake in waves could be associated with the instantaneous propeller disk velocities, boundary layer contraction/expansion due to hull motions, bilge vortex dynamics, shaft vortex dynamics and the orbital wave velocities at the propeller disk as well as the complex interactions between these factors in different operational conditions. The importance of the instantaneous propeller disk velocities was studied using the instantaneous surge velocity as well as the instantaneous vertical shaft velocity. Ship motions effects could create an adverse/favorable pressure gradient which resulted in the expansion/contraction of the boundary layer. The effects of other contributing factors were also examined using the instantaneous values for the wave elevation at the propeller disk and the instantaneous vertical shaft departure from its original position as well as the dynamics of bilge and shaft vortices in the vicinity of the propeller disk.

In $\lambda/L = 0.6$, due to small ship motions, the variation of wake during one encounter wave period from its time-averaged value was found to be mainly affected by the wave orbital velocities. However, in $\lambda/L = 1.1$ and 1.6 the ship motions introduced significant effects on the flow physics, and different factors were found to contribute to the transient wake. The maximum value of axial wake in both $\lambda/L = 1.1$ and 1.6 coincided with the time in which the shaft was almost horizontal and moving downwards and the analytical free surface elevation at propeller plane was approaching the still water level from the wave crest. In these wave lengths, the minimum value of the axial wake occurred when the shaft was located lower than its original position and moving upwards and the wave trough just passed and the free surface elevation was reaching the still water level. Moreover, in both of these wave lengths, the time t/T_E between the occurrence of the maximum of $\tilde{u}$ to the minimum of $\tilde{u}$ was similar but shorter ($\approx 0.4T_E$) than the time between minimum to maximum ($\approx 0.6T_E$). The effects of higher harmonic amplitudes were more pronounced during the time from minimum $\tilde{u}$ to approximately mean values of $\tilde{u}$, in which the bilge vortex recurs to the propeller disk. In $\lambda/L = 0.6$ the time between maximum and minimum is almost equal ($\approx 0.5T_E$) and no significant effects were seen from the higher harmonic amplitudes. Overall, the large hull motions in the longer waves dictated the variation of wake through the contraction/expansion of the boundary layer as well as imposing vortical structure dynamics. However, the wave orbital velocities were the dominant factor in the shortest wave where the hull motions are insignificant.

The contour plots of the time-averaged wake difference between the waves and the calm water conditions showed the regions with velocity deficit and excess in waves relative to calm water. These results in $\lambda/L = 1.1$ and 1.6 pinpointed the missing bilge vortex and the secondary shaft vortex in comparison to the calm water wake. It was found that since the variation of vertical shaft acceleration was more severe in $\lambda/L = 1.1$, the time in which the bilge vortex resided outside of the propeller disk was longer, hence fuller wake was observed in this wave length in comparison to $\lambda/L = 1.6$. However, the contours of the time-averaged wake in $\lambda/L = 0.6$ were rather similar to that of calm water, due to small ship motions and hence insignificant dynamics of the vortical structures. Since a propeller is often designed based on the calm water nominal wake, any deviation from the calm water wake alters the loading distribution on the blade resulting in an adverse effect on the propeller performance.

Furthermore, the analysis of the harmonic amplitudes of the axial wake on each computational cell in the propeller plane revealed large variations of the axial wake during one encounter wave period mainly in the lower part of the propeller disk area, especially in $\lambda/L = 1.1$ and 1.6. Therefore, the propeller blades passing this area will experience larger axial wake variations during one encounter period than the upper part of the disk.

Significant variations were seen for the circumferential-averaged axial velocity of wake during one encountered wave period in the regular head waves simulations, especially in $\lambda/L = 1.1$ and 1.6 where the motions are large. Such variations were significant near the propeller tip which might impact the local blade loading, the dynamics of the tip vortex, and the cavitation pattern on the blades. The time-average of the circumferential-averaged axial velocity of wake showed a rather similar radial distribution in $\lambda/L = 0.6$ in comparison to calm water, while being noticeably different in $\lambda/L = 1.1$ and 1.6, especially between $0.282 < r/R < 0.704$, where a significant proportion of the propeller thrust is often generated. Although the time-average of the circumferential-averaged vertical velocity of the wake was rather similar in waves and calm water, the variations during one encounter wave period were significant, which might be important for the angle of attack and hence propeller design.

Final Remarks

The general results are promising compared with the experimental measurements. The uncertainty of the EFD data should not be overlooked either. The flow field analyses provided valuable insight into the hull-wave interaction effects and contributed to the comprehension of the underlying physical mechanisms. Although the finer grids mainly exhibited superior results, particularly for the nominal wake predictions, the computational costs associated with such grids were relatively high. Hence, the choice of the refinement level heavily depends on the available computing resources.

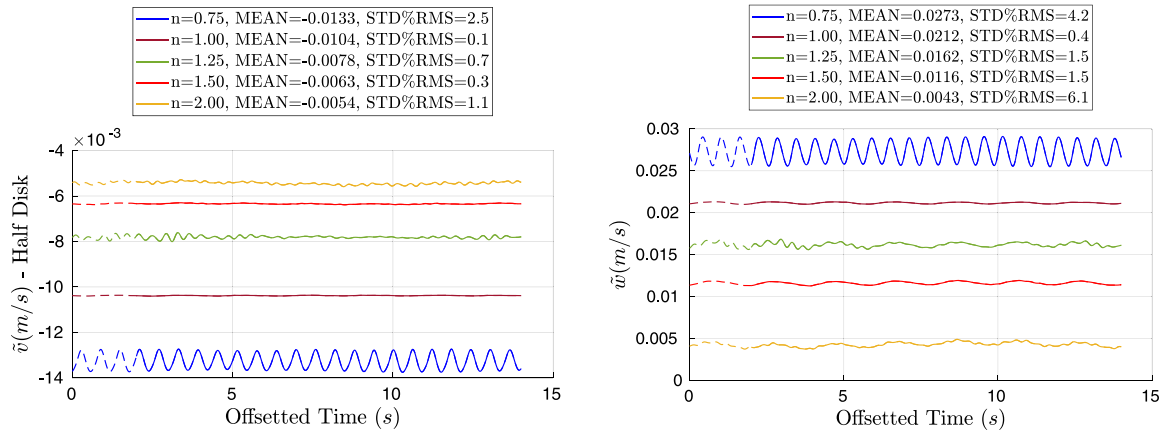

(a) Transversal component time series. (b) Vertical component time series.

Fig. A.1. Time series of the surface-averaged non-axial velocity components on hull-fixed propeller disk in calm water simulations.

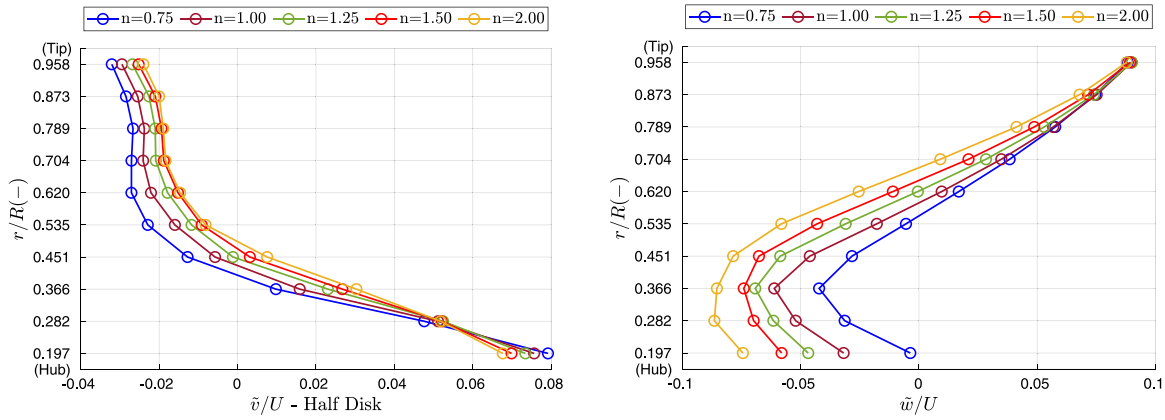

(a) Transversal component. (b) Vertical component.

Fig. A.2. Circumferential-averaged non-axial velocity components of CFD wake on hull-fixed propeller disk at the last time step in free surge calm water simulations.

CRediT authorship contribution statement

Mohsen Irannezhad: Conceptualization, Formal analysis, Investigation, Data curation, Writing – original draft, Writing – review & editing, Visualization. **Rickard E. Bensow:** Conceptualization, Writing – review & editing, Supervision. **Martin Kjellberg:** Conceptualization, Writing – review & editing, Supervision. **Arash Eslamdoost:** Conceptualization, Resources, Writing – original draft, Writing – review & editing, Supervision, Project administration, Funding acquisition.

Declaration of competing interest

The authors declare that they have no known competing financial interests or personal relationships that could have appeared to influence the work reported in this paper.

Data availability

Data will be made available on request.

Acknowledgments

This research is funded by The Swedish Transport Administration through Lighthouse (Swedish Maritime Competence Center). The simulations were performed on the resources provided by the National Academic Infrastructure for Supercomputing in Sweden (NAISS) and the Swedish National Infrastructure for Computing (SNIC) at Chalmers Centre for Computational Science and Engineering (C3SE) and National Supercomputer Center at Linköping University (NSC) partially funded by the Swedish Research Council through grant agreements no. 2022-06725 and no. 2018-05973. The authors would like to sincerely thank Professor Yasuyuki Toda from Osaka University for sharing the experimental data. Assistant Professor Ping-Chen Wu and Dr. Benson Oyunge Mwangi are also acknowledged for providing detailed information about the experimental data.

Appendix

See Figs. A.1, A.2, A.3, A.4, A.5, A.6, A.7, A.8, A.9 and A.10.

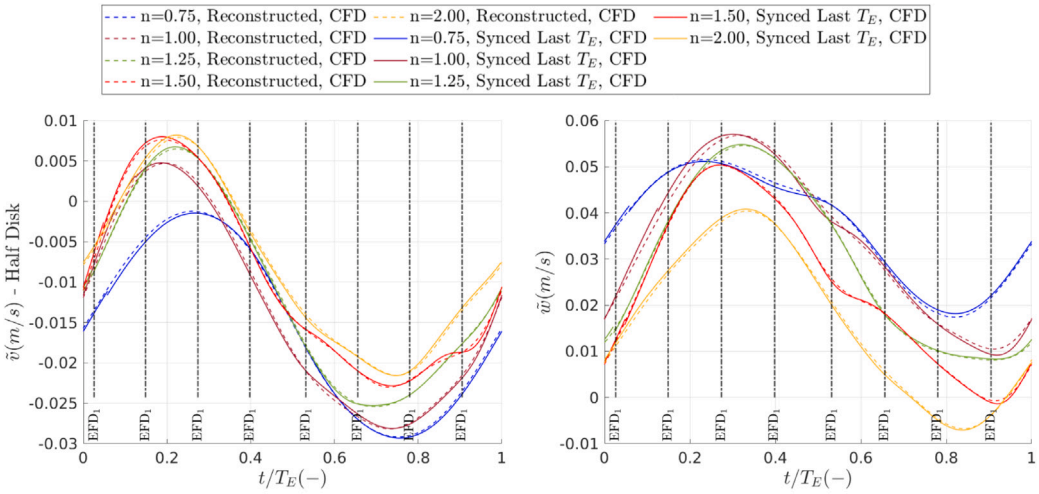

(a) Transversal velocity component. (b) Vertical velocity component.

Fig. A.3. Reconstructed and synced last T_E time series of the non-axial velocity components of the wake in $\lambda/L = 0.6$.

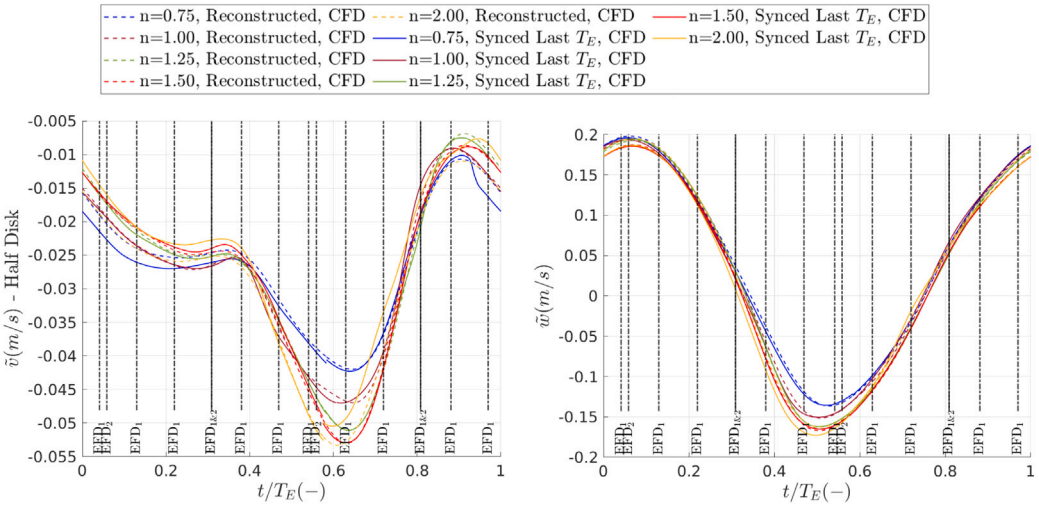

(a) Transversal velocity component. (b) Vertical velocity component.

Fig. A.4. Reconstructed and synced last T_E time series of the non-axial velocity components of the wake in $\lambda/L = 1.1$.

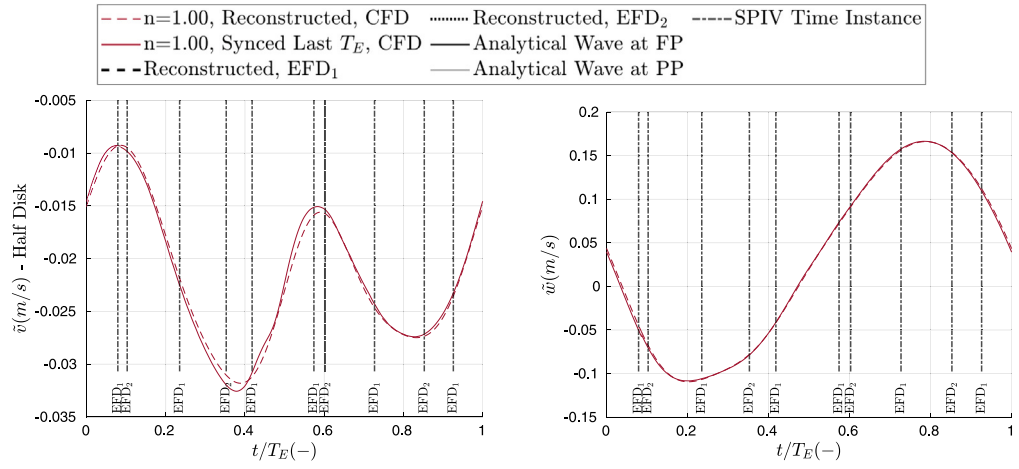

(a) Transversal velocity component. (b) Vertical velocity component.

Fig. A.5. Reconstructed and synced last T_E time series of the non-axial velocity components of the wake in $\lambda/L = 1.6$.

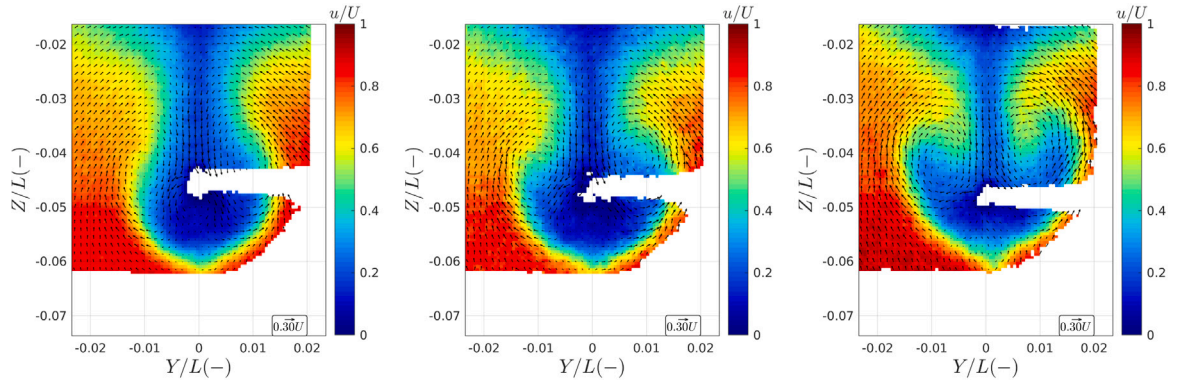

(a) EFD$_1$, $t/T_E = 0.026$. (b) EFD$_1$, $t/T_E = 0.149$. (c) EFD$_1$, $t/T_E = 0.398$.

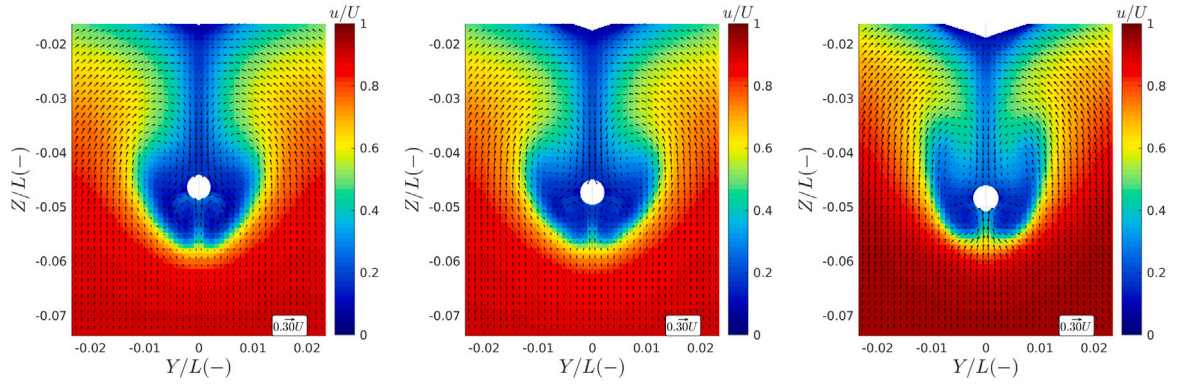

(d) $n = 1.00$, $t/T_E = 0.024$. (e) $n = 1.00$, $t/T_E = 0.150$. (f) $n = 1.00$, $t/T_E = 0.399$.

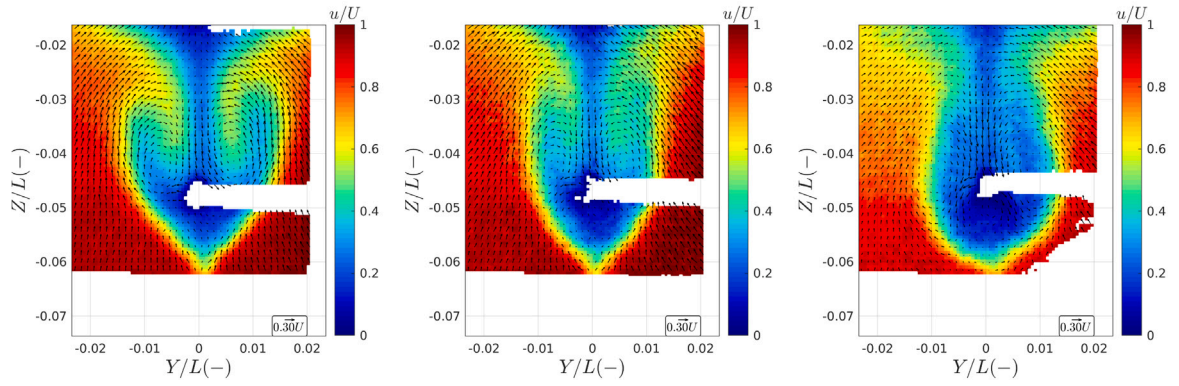

(g) EFD$_1$, $t/T_E = 0.532$. (h) EFD$_1$, $t/T_E = 0.656$. (i) EFD$_1$, $t/T_E = 0.905$.

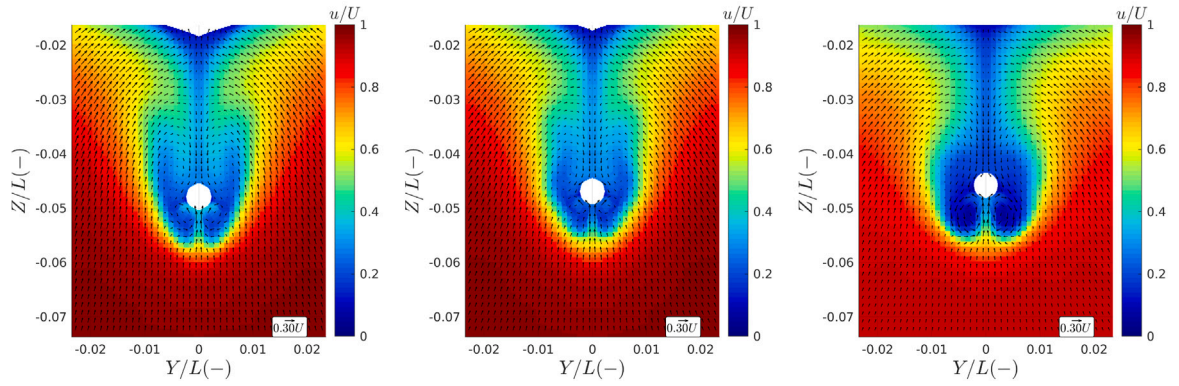

(j) $n = 1.00$, $t/T_E = 0.533$. (k) $n = 1.00$, $t/T_E = 0.656$. (l) $n = 1.00$, $t/T_E = 0.905$.

Fig. A.6. EFD$_1$ and CFD ($n = 1.00$) wake comparison in CF_{PP} in $\lambda/L = 0.6$.

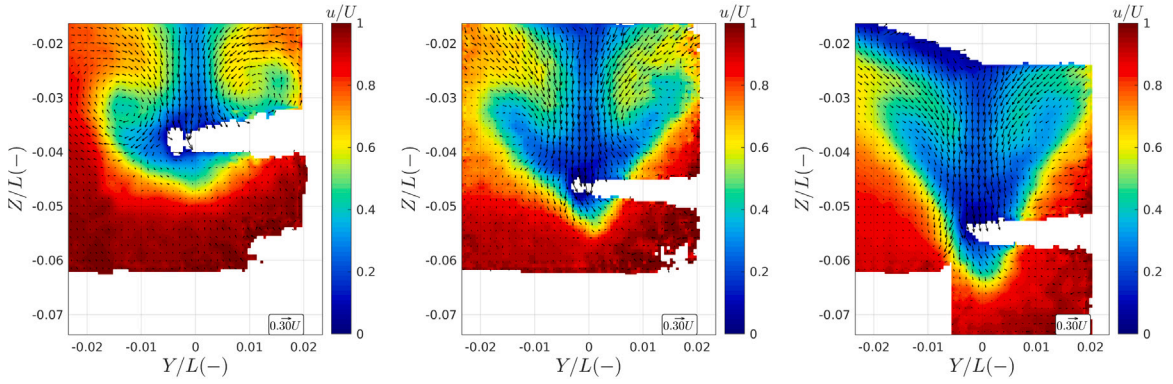

(a) EFD$_1$, $t/T_E = 0.041$. (b) EFD$_1$, $t/T_E = 0.130$. (c) EFD$_1$, $t/T_E = 0.220$.

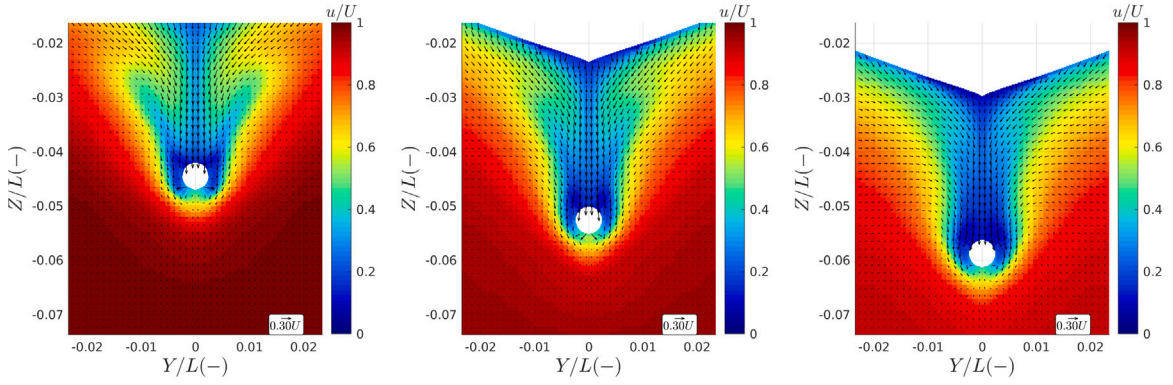

(d) $n = 1.00$, $t/T_E = 0.040$. (e) $n = 1.00$, $t/T_E = 0.131$. (f) $n = 1.00$, $t/T_E = 0.220$.

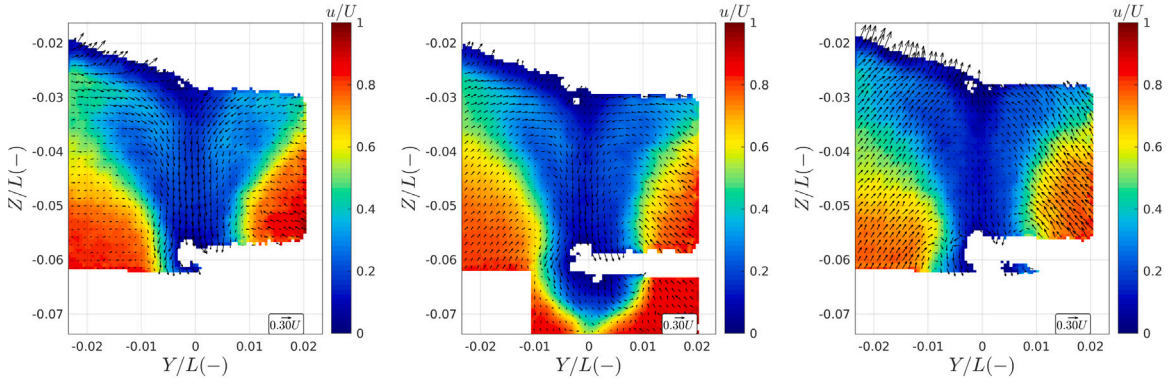

(g) EFD$_1$, $t/T_E = 0.309$. (h) EFD$_1$, $t/T_E = 0.380$. (i) EFD$_1$, $t/T_E = 0.469$.

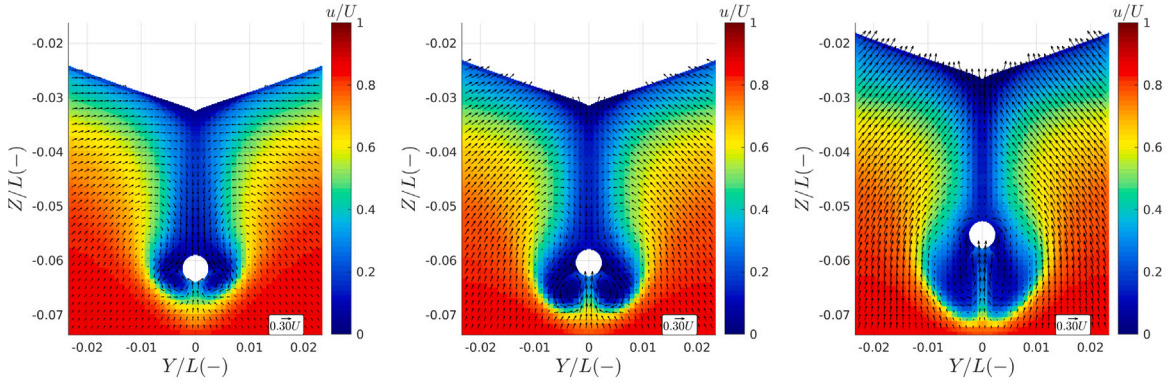

(j) $n = 1.00$, $t/T_E = 0.311$. (k) $n = 1.00$, $t/T_E = 0.380$. (l) $n = 1.00$, $t/T_E = 0.469$.

Fig. A.7. EFD$_1$ and CFD ($n = 1.00$) wake comparison in CF_{PP} in $\lambda/L = 1.1$.

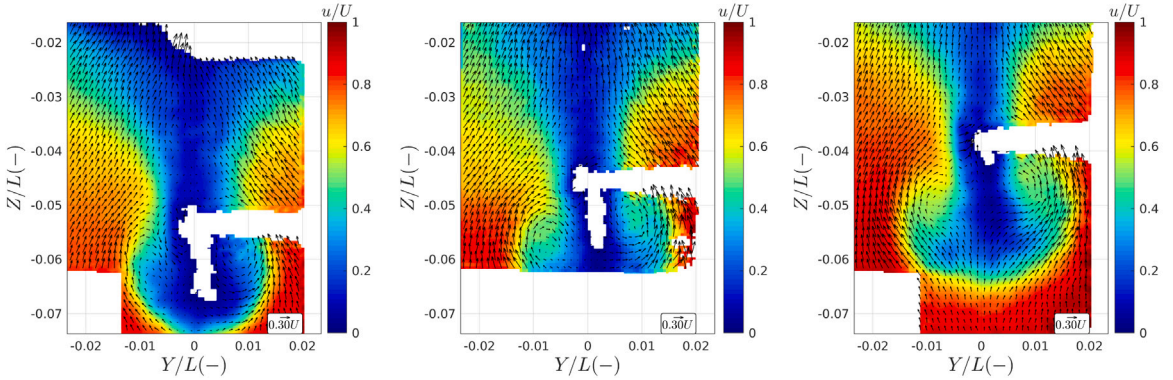

(m) EFD$_1$, $t/T_E = 0.541$. (n) EFD$_1$, $t/T_E = 0.630$. (o) EFD$_1$, $t/T_E = 0.720$.

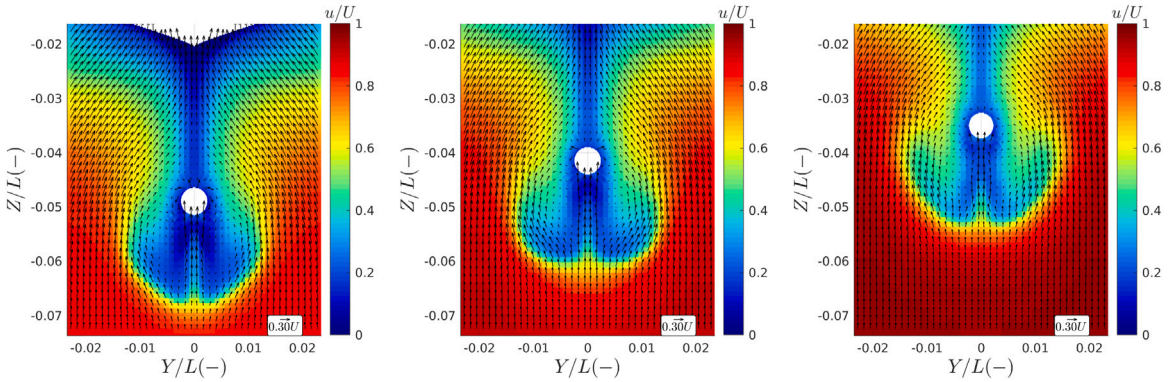

(p) $n = 1.00$, $t/T_E = 0.541$. (q) $n = 1.00$, $t/T_E = 0.629$. (r) $n = 1.00$, $t/T_E = 0.720$.

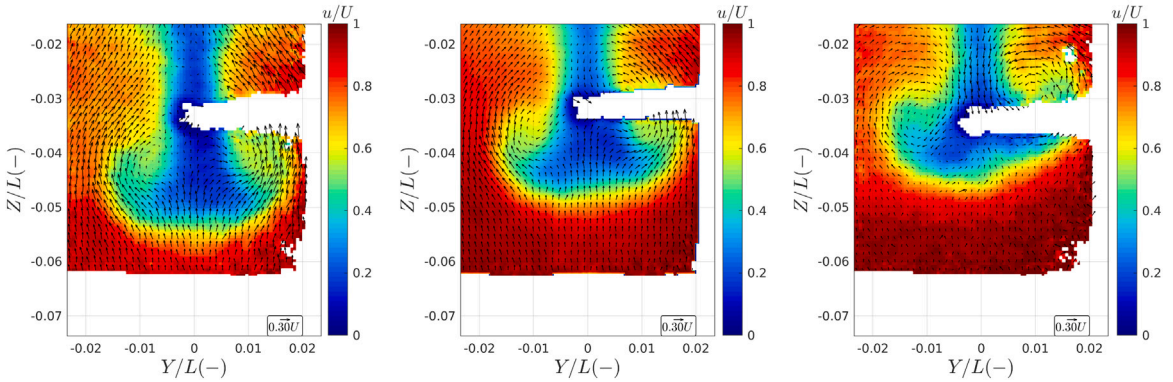

(s) EFD$_1$, $t/T_E = 0.809$. (t) EFD$_1$, $t/T_E = 0.880$. (u) EFD$_1$, $t/T_E = 0.970$.

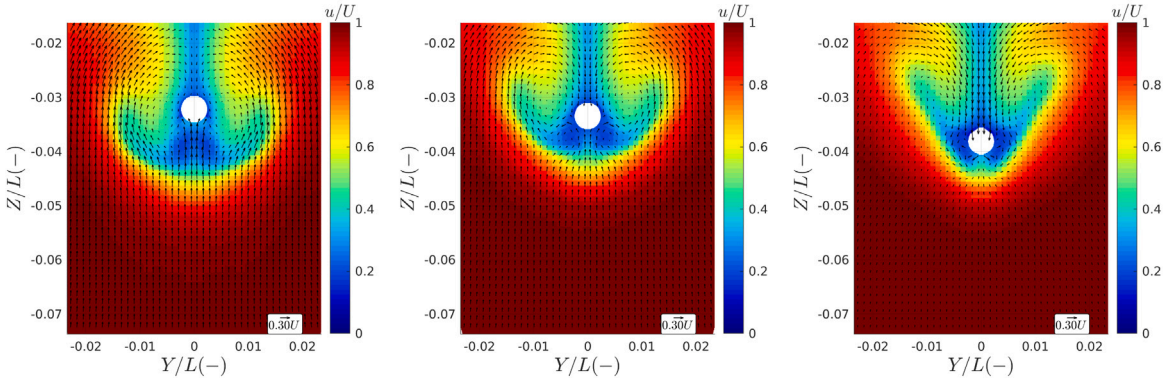

(v) $n = 1.00$, $t/T_E = 0.809$. (w) $n = 1.00$, $t/T_E = 0.881$. (x) $n = 1.00$, $t/T_E = 0.969$.

Fig. A.7. (*continued*).

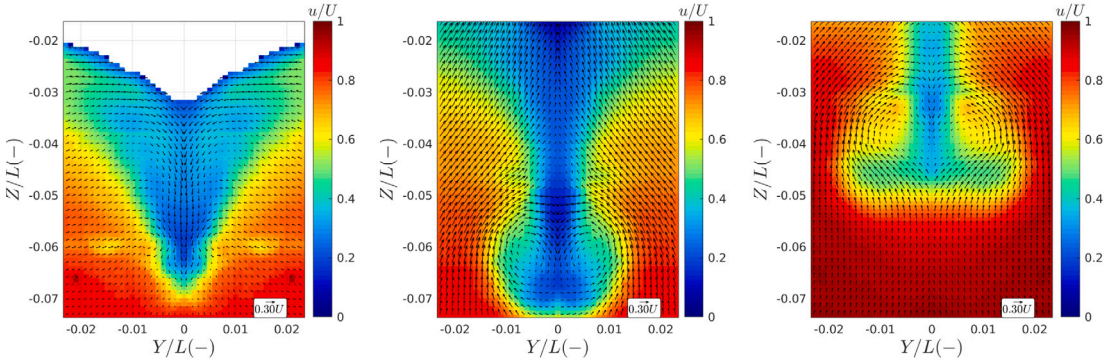

(a) EFD$_2$, $t/T_E = 0.309$. (b) EFD$_2$, $t/T_E = 0.559$. (c) EFD$_2$, $t/T_E = 0.809$.

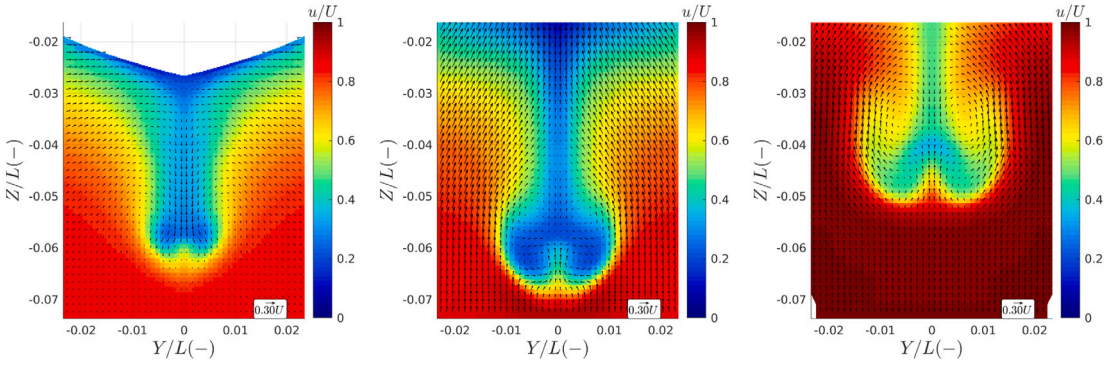

(d) $n = 1.00$, $t/T_E = 0.308$. (e) $n = 1.00$, $t/T_E = 0.560$. (f) $n = 1.00$, $t/T_E = 0.809$.

Fig. A.8. EFD$_2$ and CFD ($n = 1.00$) wake comparison in CF_{AP} in $\lambda/L = 1.1$.

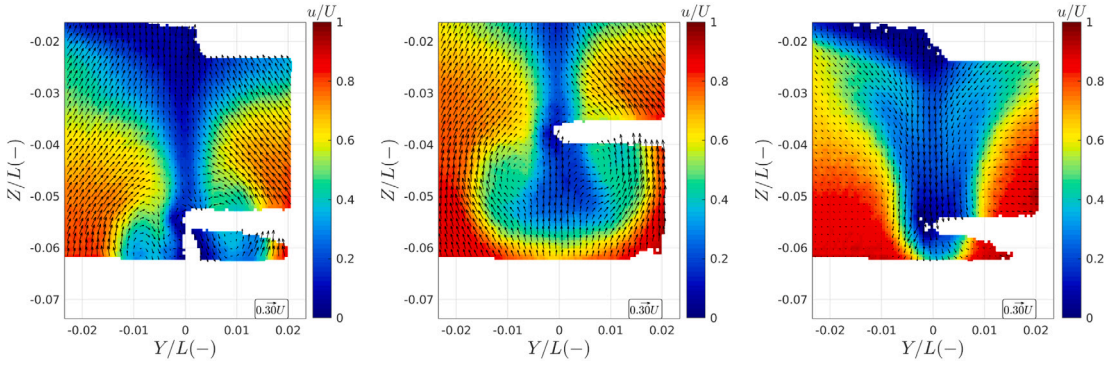

(a) EFD$_1$, $t/T_E = 0.235$. (b) EFD$_1$, $t/T_E = 0.418$. (c) EFD$_1$, $t/T_E = 0.926$.

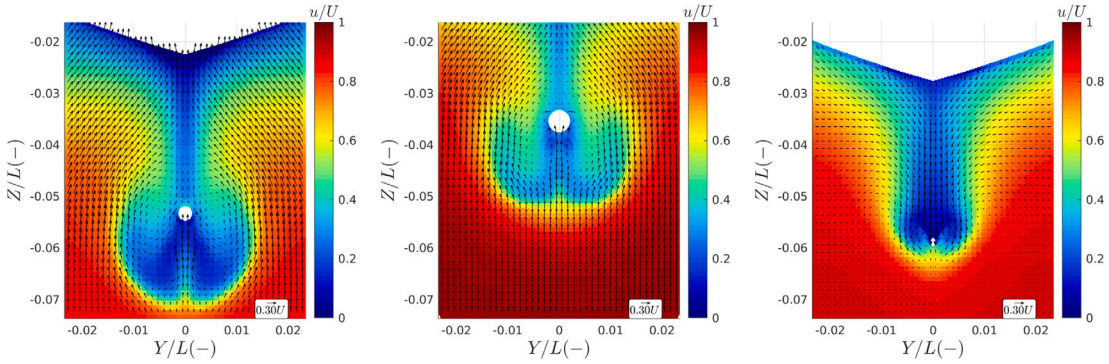

(d) $n = 1.00$, $t/T_E = 0.236$. (e) $n = 1.00$, $t/T_E = 0.418$. (f) $n = 1.00$, $t/T_E = 0.926$.

Fig. A.9. EFD$_1$ and CFD ($n = 1.00$) wake comparison in CF_{PP} in $\lambda/L = 1.6$.

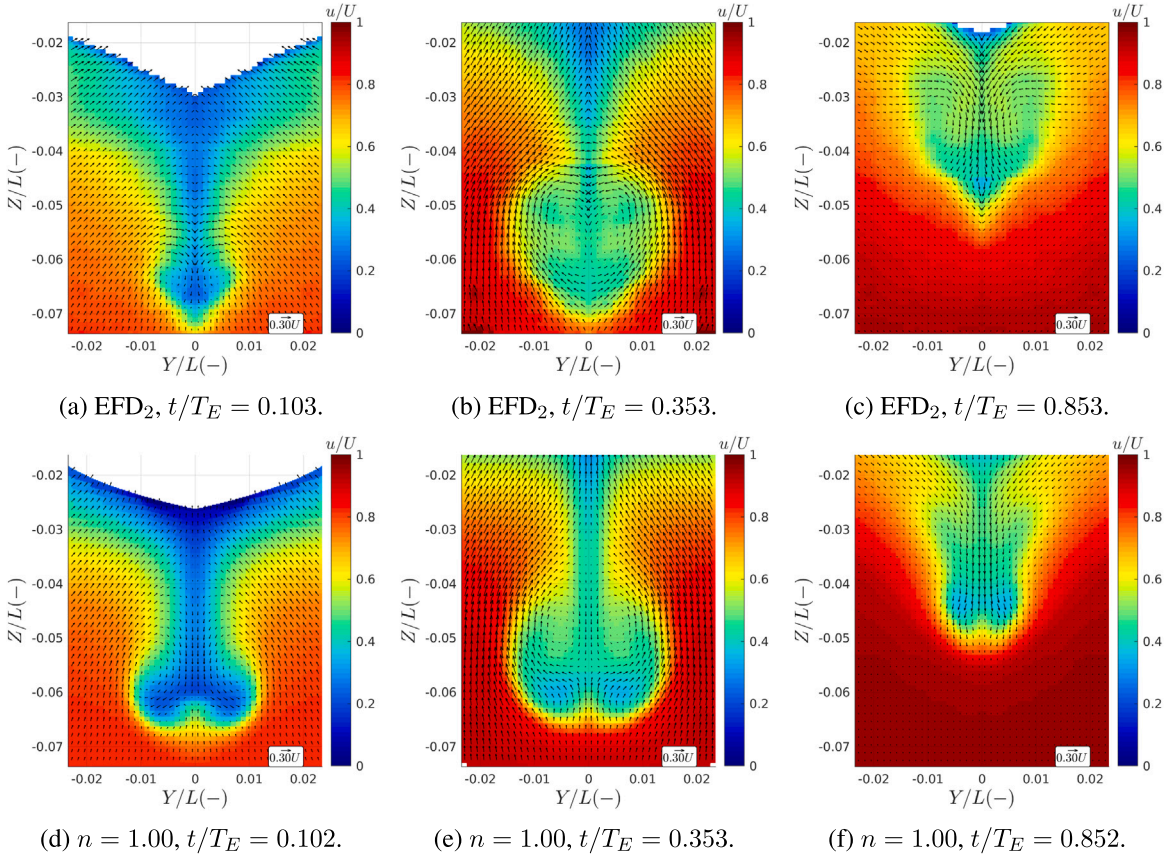

(a) EFD$_2$, $t/T_E = 0.103$. (b) EFD$_2$, $t/T_E = 0.353$. (c) EFD$_2$, $t/T_E = 0.853$.

(d) $n = 1.00$, $t/T_E = 0.102$. (e) $n = 1.00$, $t/T_E = 0.353$. (f) $n = 1.00$, $t/T_E = 0.852$.

Fig. A.10. EFD$_2$ and CFD ($n = 1.00$) wake comparison in CF_{AP} in $\lambda/L = 1.6$.

References

Berndt, J.C., Perić, R., Abdel-Maksoud, M., 2021. Improved simulation of flows with free-surface waves by optimizing the angle factor in the HRIC interface-sharpening scheme. J. Appl. Fluid Mech. (ISSN: 1735-3572) 14 (3), 909–920. http://dx.doi.org/10.47176/jafm.14.03.32062, URL https://www.jafmonline.net/article_1132.html.

Bertram, Volker, 2012. Practical Ship Hydrodynamics, second ed. Butterworth-Heinemann, Oxford.

Bhattacharyya, Rameswar, 1978. Dynamics of Marine Vehicles. In: A Wiley-Interscience publication, Wiley.

Block, Jan Jacobus, 1993. The resistance increase of a ship in waves (Ph.D. thesis). Delft University of Technology.

Carrica, Pablo M., Wilson, Robert V., Noack, Ralph W., Stern, Fred, 2007. Ship motions using single-phase level set with dynamic overset grids. Comput. & Fluids (ISSN: 0045-7930) 36 (9), 1415–1433. http://dx.doi.org/10.1016/j.compfluid.2007.01.007.

Castiglione, Teresa, Stern, Frederick, Bova, Sergio, Kandasamy, Manivannan, 2011. Numerical investigation of the seakeeping behavior of a catamaran advancing in regular head waves. Ocean Eng. (ISSN: 0029-8018) 38 (16), 1806–1822. http://dx.doi.org/10.1016/j.oceaneng.2011.09.003.

Chen, Si, Hino, Takanori, Ma, Ning, Gu, Xiechong, 2018. RANS investigation of influence of wave steepness on ship motions and added resistance in regular waves. J. Mar. Sci. Technol. (Japan) 23 (4), 991–1003. http://dx.doi.org/10.1007/s00773-018-0527-5.

Crepier, P., 2017. Ship resistance prediction: verification and validation exercise on unstructured grids. In: MARINE VII : Proceedings of the VII International Conference on Computational Methods in Marine Engineering. CIMNE, ISBN: 978-84-946909-8-3, pp. 365–376, URL http://hdl.handle.net/2117/331841.

Eça, L., Hoekstra, M., 2014. A procedure for the estimation of the numerical uncertainty of CFD calculations based on grid refinement studies. J. Comput. Phys. (ISSN: 0021-9991) 262, 104–130. http://dx.doi.org/10.1016/j.jcp.2014.01.006.

Eça, L., Klaij, C.M., Vaz, G., Hoekstra, M., Pereira, F.S., 2016. On code verification of RANS solvers. J. Comput. Phys. (ISSN: 0021-9991) 310, 418–439. http://dx.doi.org/10.1016/j.jcp.2016.01.002.

Eça, L., Vaz, G., Toxopeus, S.L., Hoekstra, M., 2019. Numerical errors in unsteady flow simulations. J. Verif. Valid. Uncert. Quant. (ISSN: 2377-2158) 4 (2), http://dx.doi.org/10.1115/1.4043975, 021001.

Fenton, J.D., 1985. A fifth-order stokes theory for steady waves. J. Waterway Port Coastal Ocean Eng. 111 (2), 216–234. http://dx.doi.org/10.1061/(ASCE)0733-950X(1985)111:2(216).

Gao, Qingze, Song, Lifei, Yao, Jianxi, 2021. Rans prediction of wave-induced ship motions, and steady wave forces and moments in regular waves. J. Mar. Sci. Eng. 9 (12), http://dx.doi.org/10.3390/jmse9121459.

Gerritsma, J., Beukelman, W., 1972. Analysis of the resistance increase in waves of a fast cargo ship. Int. Shipbuild. Progress (ISSN: 0020868X) 19 (217), 285–293. http://dx.doi.org/10.3233/isp-1972-1921701.

Guo, Bing-jie, Steen, Sverre, 2011. Evaluation of added resistance of KVLCC2 in short waves. J. Hydrodyn. 23, 709–722. http://dx.doi.org/10.1016/S1001-6058(10)60168-0.

Guo, B.J., Steen, S., Deng, G.B., 2012. Seakeeping prediction of KVLCC2 in head waves with RANS. Appl. Ocean Res. (ISSN: 0141-1187) 35, 56–67. http://dx.doi.org/10.1016/j.apor.2011.12.003, URL https://www.sciencedirect.com/science/article/pii/S0141118711001040.

Hayashi, Y., 2012. Phase-averaged 3DPIV flow field measurement for KVLCC2 model in waves. Osaka University, Japan (in Japanese).

Hino, Takanori, Stern, Frederick, Larsson, Lars, Visonneau, Michel, Hirata, Nobuyuki, Kim, Jin (Eds.), 2021. Numerical Ship Hydrodynamics - An Assessment of the Tokyo 2015 Workshop. Springer, http://dx.doi.org/10.1007/978-3-030-47572-7.

Hossain, Md. Alfaz, Wu, Ping-Chen, Shibano, Yusuke, Toda, Yasuyuki, 2018. Forces, ship motions and velocity wake field for KRISO container ship model in regular head waves. In: International Ocean and Polar Engineering Conference. ISOPE-I-18-339.

Irannezhad, Mohsen, 2022. Numerical Investigation of Ship Responses in Calm Water and Regular Head Waves. In: Thesis for the degree of Licentiate of Engineering: 2022:4, Department of Mechanics and Maritime Sciences, Chalmers University of Technology, URL https://search.ebscohost.com/login.aspx?direct=true&db=cat09075a&AN=clpc.oai.edge.chalmers.folio.ebsco.com.fs00001000.fc3c91e4.fb13.4370.acdb.4142d02bd062&site=eds-live&scope=site&authtype=guest&custid=s3911979&groupid=main&profile=eds.

Irannezhad, Mohsen, Eslamdoost, Arash, Kjellberg, Martin, Bensow, Rickard E., 2022. Investigation of ship responses in regular head waves through a fully nonlinear potential flow approach. Ocean Eng. (ISSN: 0029-8018) 246, 110410. http://dx.doi.org/10.1016/j.oceaneng.2021.110410, URL https://www.sciencedirect.com/science/article/pii/S0029801821016991.

Irvine, Jr., Martin, Longo, Joseph, Stern, Fredrick, 2008. Pitch and heave tests and uncertainty assessment for a surface combatant in regular head waves. J. Ship Res. (ISSN: 0022-4502) 52 (02), 146–163. http://dx.doi.org/10.5957/jsr.2008.52.2.146.

Islam, H., Guedes Soares, C., 2022. Head wave simulation of a KRISO container ship model using OpenFOAM for the assessment of sea margin. J. Offshore Mech. Arct. Eng. 144 (3), http://dx.doi.org/10.1115/1.4053538.

ITTC, 2014. International Towing Tank Conference. Recommended Procedures and Guidelines 7.5-03-02-03, "Practical Guidelines for Ship CFD Applications", 27th ITTC, 2014.

ITTC, 2017a. International Towing Tank Conference. Recommended Procedures and Guidelines 7.5-02-03-01.5, "Predicting Powering Margins", 28th ITTC, 2017.

ITTC, 2017b. International Towing Tank Conference. Recommended Procedures and Guidelines 7.5-02-07-02.8, "Calculation of the weather factor f_w for decrease of ship speed in wind and waves", 28th ITTC, 2017.

ITTC, 2021a. International Towing Tank Conference. Final Report and Recommendations from the Seakeeping Committee, 29th ITTC, 2021.

ITTC, 2021b. International Towing Tank Conference. Final Report and Recommendations from the Specialist Committee on Modelling of Environmental Conditions, 29th ITTC, 2021.

Kim, Ho, 2014. Phase-Averaged SPIV Wake Field Measurement for KVLCC2 Propeller Plane in Waves (Ph.D. thesis). Osaka University, Japan, http://dx.doi.org/10.18910/50513.

Kim, Yoo-Chul, Kim, Kwang-Soo, Kim, Jin, Kim, Yoonsik, Park, Il-Ryong, Jang, Young-Hun, 2017. Analysis of added resistance and seakeeping responses in head sea conditions for low-speed full ships using URANS approach. Int. J. Nav. Archit. Ocean Eng. (ISSN: 2092-6782) 9 (6), 641–654. http://dx.doi.org/10.1016/j.ijnaoe.2017.03.001.

Larsson, L., Raven, H.C., 2010. Ship Resistance and Flow. In: PNA Series, Society of Naval Architects and Marine Engineers, Jersey City.

Larsson, Lars, Stern, Frederik, Visonneau, Michel (Eds.), 2014. Numerical Ship Hydrodynamics - An Assessment of the Gothenburg 2010 Workshop. Springer, http://dx.doi.org/10.1007/978-94-007-7189-5.

Lee, Jae-Hoon, Kim, Yonghwan, Kim, Beom-Soo, Gerhardt, Frederik, 2021a. Comparative study on analysis methods for added resistance of four ships in head and oblique waves. Ocean Eng. 236, http://dx.doi.org/10.1016/j.oceaneng.2021.109552.

Lee, Soon-Hyun, Paik, Kwang-Jun, Hwang, Hong-Sik, Eom, Myeong-Jin, Kim, Sang-Hyun, 2021b. A study on ship performance in waves using a RANS solver, part 1: Comparison of power prediction methods in regular waves. Ocean Eng. 227, http://dx.doi.org/10.1016/j.oceaneng.2021.108900.

Lee, Soon-Hyun, Paik, Kwang-Jun, Lee, Jun-Hee, 2022. A study on ship performance in waves using a RANS solver, part 2: Comparison of added resistance performance in various regular and irregular waves. Ocean Eng. (ISSN: 0029-8018) 263, 112174. http://dx.doi.org/10.1016/j.oceaneng.2022.112174.

Lee, Jaehoon, Park, Dong-Min, Kim, Yonghwan, 2017. Experimental investigation on the added resistance of modified KVLCC2 hull forms with different bow shapes. Proc. Inst. Mech. Eng. M 231 (2), 395–410. http://dx.doi.org/10.1177/1475090216643981.

Lee, Cheol-Min, Park, Sung-Chul, Yu, Jin-Won, Choi, Jung-Eun, Lee, Inwon, 2019. Effects of diffraction in regular head waves on added resistance and wake using CFD. Int. J. Nav. Archit. Ocean Eng. (ISSN: 2092-6782) 11 (2), 736–749. http://dx.doi.org/10.1016/j.ijnaoe.2019.02.013, URL https://www.sciencedirect.com/science/article/pii/S2092678217303758.

Lemaire, Sébastien, Vaz, Guilherme, Rijswijk, Menno, Turnock, Stephen, 2021. On the accuracy, robustness and performance of high order interpolation schemes for the overset method on unstructured grids. Internat. J. Numer. Methods Fluids 93, 1–36. http://dx.doi.org/10.1002/fld.5050.

Lungu, Adrian, 2022. Numerical investigation of the 6-DOF seakeeping performances of the KCS containership. J. Mar. Sci. Eng. (ISSN: 2077-1312) 10 (10), http://dx.doi.org/10.3390/jmse10101397.

Menter, F.R., 1994. Two-equation eddy-viscosity turbulence models for engineering applications. AIAA J. 32 (8), 1598–1605. http://dx.doi.org/10.2514/3.12149.

Mikkelsen, Henrik, Shao, Yanlin, Walther, Jens Honoré, 2022. Numerical study of nominal wake fields of a container ship in oblique regular waves. Appl. Ocean Res. (ISSN: 0141-1187) 119, 102968. http://dx.doi.org/10.1016/j.apor.2021.102968.

Moctar, Ould el, Sigmund, Sebastian, Ley, Jens, Schellin, Thomas E., 2016. Numerical and experimental analysis of added resistance of ships in waves. J. Offshore Mech. Arct. Eng. (ISSN: 0892-7219) 139 (1), http://dx.doi.org/10.1115/1.4034205.

Muzaferija, S., Peric', M., 1998. Computation of free surface flows using interface-tracking and interface-capturing methods. In: Mahrenholtz, O., Markiewicz, M. (Eds.), Nonlinear Water Wave Interaction. Computational Mechanics Publications, Southampton.

Mwangi, Benson Oyunge, 2021. SPIV Flow Field Measurement around the Stern of a Self-propelled KVLCC2 Model Ship in Regular Head Waves (Ph.D. thesis). Osaka University, Japan, http://dx.doi.org/10.18910/85407.

Ozdemir, Yavuz Hakan, Barlas, Baris, 2017. Numerical study of ship motions and added resistance in regular incident waves of KVLCC2 model. Int. J. Nav. Archit. Ocean Eng. 9 (2), 149–159. http://dx.doi.org/10.1016/j.ijnaoe.2016.09.001.

Papanikolaou, A., Zaraphonitis, G., Bitner-Gregersen, E., Shigunov, V., Moctar, O. El, Soares, C. Guedes, Reddy, D.N., Sprenger, F., 2016. Energy efficient safe ship operation (SHOPERA). Transp. Res. Procedia (ISSN: 2352-1465) 14, 820–829. http://dx.doi.org/10.1016/j.trpro.2016.05.030, Transport Research Arena TRA2016.

Park, Dong-Min, Lee, Jaehoon, Kim, Yonghwan, 2015. Uncertainty analysis for added resistance experiment of KVLCC2 ship. Ocean Eng. (ISSN: 0029-8018) 95, 143–156. http://dx.doi.org/10.1016/j.oceaneng.2014.12.007.

Pereira, F.S., Eça, L., Vaz, G., 2017. Verification and validation exercises for the flow around the KVLCC2 tanker at model and full-scale Reynolds numbers. Ocean Eng. (ISSN: 0029-8018) 129, 133–148. http://dx.doi.org/10.1016/j.oceaneng.2016.11.005.

Perić, Robinson, Abdel-Maksoud, Moustafa, 2018. Analytical prediction of reflection coefficients for wave absorbing layers in flow simulations of regular free-surface waves. Ocean Eng. (ISSN: 0029-8018) 147, 132–147. http://dx.doi.org/10.1016/j.oceaneng.2017.10.009, URL https://www.sciencedirect.com/science/article/pii/S0029801817306066.

Perić, Robinson, Abdel-Maksoud, Moustafa, 2020. Reducing Undesired Wave Reflection at Domain Boundaries in 3D Finite Volume-Based Flow Simulations via Forcing Zones. J. Ship Res. (ISSN: 0022-4502) 64 (01), 23–47. http://dx.doi.org/10.5957/jsr.2020.64.1.23.

Perić, Robinson, Vukčević, Vuko, Abdel-Maksoud, Moustafa, Jasak, Hrvoje, 2022. Optimizing wave generation and wave damping in 3D-flow simulations with implicit relaxation zones. Coast. Eng. (ISSN: 0378-3839) 171, 104035. http://dx.doi.org/10.1016/j.coastaleng.2021.104035, URL https://www.sciencedirect.com/science/article/pii/S0378383921001794.

Roache, Patrick J., 1998. Verification of codes and calculations. AIAA J. 36 (5), 696–702. http://dx.doi.org/10.2514/2.457.

Sadat-Hosseini, Hamid, Wu, Ping-Chen, Carrica, Pablo, Kim, Ho, Toda, Yasuyuki, Stern, Frederick, 2013. CFD verification and validation of added resistance and motions of KVLCC2 with fixed and free surge in short and long head waves. Ocean Eng. 59, 240–273. http://dx.doi.org/10.1016/j.oceaneng.2012.12.016.

Saettone, Simone, 2020. Ship Propulsion Hydrodynamics in Waves (Ph.D. thesis). Technical University of Denmark.

Seo, Jin-Hyeok, Lee, Cheol-Min, Yu, Jin-Won, Choi, Jung-Eun, Lee, Inwon, 2020. Power increase and propulsive characteristics in regular head waves of KVLCC2 using model tests. Ocean Eng. (ISSN: 0029-8018) 216, 108058. http://dx.doi.org/10.1016/j.oceaneng.2020.108058.

Seo, Seonguk, Park, Sunho, Koo, BonYong, 2017. Effect of wave periods on added resistance and motions of a ship in head sea simulations. Ocean Eng. 137, 309–327. http://dx.doi.org/10.1016/j.oceaneng.2017.04.009.

Shen, Zhirong, Wan, Decheng, 2013. RANS computations of added resistance and motions of a ship in head waves. Int. J. Offshore Polar Eng. 23 (4), 263–271.

Shin, Hyun-Woo, Paik, Kwang-Jun, Jang, Yoon-Ho, Eom, Myeoung-Jin, Lee, Sung-wook, 2020. A numerical investigation on the nominal wake of KVLCC2 model ship in regular head waves. Int. J. Nav. Archit. Ocean Eng. (ISSN: 2092-6782) 12, 270–282. http://dx.doi.org/10.1016/j.ijnaoe.2020.01.001, URL https://www.sciencedirect.com/science/article/pii/S2092678219300147.

Shivachev, Emil, Khorasanchi, Mahdi, Day, Sandy, Turan, Osman, 2020. Impact of trim on added resistance of KRISO container ship (KCS) in head waves: An experimental and numerical study. Ocean Eng. (ISSN: 0029-8018) 211, 107594. http://dx.doi.org/10.1016/j.oceaneng.2020.107594.

Siemens Industries Digital Software, 2020. Simcenter STAR-CCM+ user guide. Version 2020.3.

Sigmund, Sebastian, 2019. Performance of ships in waves (Ph.D. thesis). http://dx.doi.org/10.17185/duepublico/70021.

Simonsen, Claus D., Otzen, Janne F., Joncquez, Soizic, Stern, Frederick, 2013. EFD and CFD for KCS heaving and pitching in regular head waves. J. Mar. Sci. Technol. (Japan) (ISSN: 09484280) http://dx.doi.org/10.1007/s00773-013-0219-0.

Sprenger, Florian, Maron, Adolfo, Delefortrie, Guillaume, van Zwijnsvoorde, Thibaut, Cura-Hochbaum, Andres, Lengwinat, Antonio, Papanikolaou, Apostolos, 2017. Experimental studies on seakeeping and maneuverability of ships in adverse weather conditions. J. Ship Res. (ISSN: 0022-4502) 61 (03), 131–152. http://dx.doi.org/10.5957/JOSR.170002.

Tavakoli, Sasan, Khojasteh, Danial, Haghani, Milad, Hirdaris, Spyros, 2023. A review on the progress and research directions of ocean engineering. Ocean Eng. (ISSN: 0029-8018) 272, 113617. http://dx.doi.org/10.1016/j.oceaneng.2023.113617, URL https://www.sciencedirect.com/science/article/pii/S002980182300001X.

Win, Yan, Wu, Ping-Chen, Akamatsu, Keisuke, Okawa, Hiroshi, Stern, Frederick, Toda, Yasuyuki, 2016. RANS simulation of KVLCC2 using simple body-force propeller model with rudder and without rudder. J. Jpn. Soc. Nav. Archit. Ocean Eng. 23, 1–11. http://dx.doi.org/10.2534/jjasnaoe.23.1.

Wu, Ping-Chen, 2013. A CFD Study on Added Resistance, Motions and Phase Averaged Wake Fields of Full Form Ship Model in Head Waves (Ph.D. thesis). Osaka University, Japan, http://dx.doi.org/10.18910/26191.

Wu, Ping-Chen, Hossain, Md. Alfaz, Kawakami, Naoki, Tamaki, Kento, Kyaw, Htike Aung, Matsumoto, Ayaka, Toda, Yasuyuki, 2020. EFD and CFD study of forces, ship motions, and flow field for KRISO container ship model in waves. J. Ship Res. (ISSN: 0022-4502) 64 (01), 61–80. http://dx.doi.org/10.5957/jsr.2020.64.1.61.

Wu, Ping-Chen, Okawa, H., Kim, H, Akamatsu, K., Sadat-Hosseini, Hamid, Stern, Fred, Toda, Yasuyuki, 2014. Added resistance and nominal wake in waves of KVLCC2 model ship in ballast condition. In: Proceedings of the 30th Symposium on Naval Hydrodynamics. Tasmania, Australia, pp. 2–7.

Wu, Ping-Chen, Sadat-Hosseini, Hamid, Stern, Fred, Toda, Yasuyuki, 2016. Nominal wake fluctuation due to waves: Volume mean and distribution based on CFD. J. Jpn. Soc. Nav. Archit. Ocean Eng. 24, 13–19. http://dx.doi.org/10.2534/jjasnaoe.24.13.

Ye, Haixuan, Shen, Zhirongn, Wan, Decheng, 2012. Numerical prediction of added resistance and vertical ship motions in regular head waves. J. Mar. Sci. Appl. 11, 410–416. http://dx.doi.org/10.1007/s11804-012-1150-1.

Yu, Jin-Won, Lee, Cheol-Min, Choi, Jung-Eun, Lee, Inwon, 2017. Effect of ship motions on added resistance in regular head waves of KVLCC2. Ocean Eng. (ISSN: 0029-8018) 146, 375–387. http://dx.doi.org/10.1016/j.oceaneng.2017.09.019.